FOUR-WAVE MIXING EXPERIMENTS ON SOLUTION-PROCESSED METHYLAMMONIUM LEAD IODIDE (CH3NH3PBI3) PEROVSKITE THIN FILMS

by

Samuel March

Submitted in partial fulfillment of the requirements
for the degree of Doctor of Philosophy

at

Dalhousie University
Halifax, Nova Scotia
December 2018

Table of Contents

List of Figures . . . . **v**

Abstract . . . . **viii**

List of Abbreviations and Symbols Used . . . . **ix**

Acknowledgements . . . . **xi**

Chapter 1 Introduction **1**

1.1 Optical Properties of Semiconductors 6
  1.1.1 Bulk Semiconductor Properties 6
  1.1.2 Carrier Dynamics Following Photoexcitation 8

1.2 Materials 10
  1.2.1 $CH_3NH_3PbI_3$ (MAPI) Perovskite Semiconductor 10
  1.2.2 The Prototypical III-V semiconductor: GaAs 12

1.3 Optical Spectroscopy 12
  1.3.1 Four-Wave Mixing Spectroscopy (FWM) 14

1.4 Literature Review 17
  1.4.1 Exciton Binding Energies in MAPI Perovskite 17
  1.4.2 Carrier-Carrier Scattering in GaAs and MAPI Perovskite 19
  1.4.3 Carrier-phonon Scattering in MAPI Perovskite 20

1.5 Overview of Thesis 21
  1.5.1 Structure of the Thesis 22

Chapter 2 Background and Theory **23**

2.1 Electronic Structure and Optical Properties of III-V Semiconductors 23
  2.1.1 Optical Absorption 27
  2.1.2 Carrier Scattering 32

2.2 Theory and Analysis of Four-Wave Mixing Spectroscopy 35
  2.2.1 Independent (Non-Interacting) Two-Level System 36
  2.2.2 Inhomogeneously Broadened Transitions 38
  2.2.3 Many-Body Effects 39

Chapter 3 Experimental Methods 43

3.1 Sample Preparation and Characterization 43
 3.1.1 MAPI Perovskite Thin-Film 43
 3.1.2 GaAs Single Crystal 45

3.2 Four-Wave Mixing Spectroscopy 46
 3.2.1 Carrier Dephasing Times 48

3.3 Pulse Characterization 49
 3.3.1 Ultrafast Pulse Width Compression and Measurement 50
 3.3.2 Pulse Spectrum Measurement 52
 3.3.3 Laser Spot Size Measurement 52
 3.3.4 Carrier Density Calculation 52

Chapter 4 Simultaneous observation of free and defect-bound excitons in $CH_3NH_3PbI_3$ using four-wave mixing spectroscopy 54

4.1 Abstract 55

4.2 Introduction 55

4.3 Results and Discussion 58

4.4 Conclusions 65

4.5 Acknowledgements 65

Chapter 5 Four-Wave Mixing in Perovskite Photovoltaic Materials Reveals Long Dephasing Times and Weaker Many-Body Interactions than GaAs 66

5.1 Abstract 67

5.2 Introduction 68

5.3 Weak Exciton-Carrier Scattering in $CH_3NH_3PbI_3$ 69

5.4 Long Interband Dephasing Time in $CH_3NH_3PbI_3$: Weak Carrier-Carrier Scattering 73

5.5 Role of Defects: Comparison to Low-temperature-grown GaAs 77

5.6 Conclusions and Outlook 79

5.7 Acknowledgements 80

5.8 Supporting Information 80

5.8.1 $CH_3NH_3PbI_3$ thin-film preparation 80
5.8.2 Molecular beam epitaxy growth of GaAs and LT-GaAs 81

5.9 Optical experiments 82

5.10 Many-body exciton signal caused by exciton-free carrier interactions 82

5.11 Extraction of electron-hole pair dephasing times 83

Chapter 6 Ultrafast acoustic phonon scattering in $CH_3NH_3PbI_3$ 87

6.1 Abstract 88

6.2 Introduction 88

6.3 Results and Discussion 92

6.4 Conclusions 97

6.5 Acknowledgements 98

Chapter 7 Conclusion 99

Bibliography 103

Appendix A Copyright Permission 121

List of Figures

1.1 Worldwide cumulative photovoltaic installations 2

1.2 Solar module production by technology as a function of time . 2

1.3 National Renewable Energy Labs (NREL) best research solar cell chart 4

1.4 MAPI Perovskite band structure. 7

1.5 Photon absorption in a simple 2-level atom 7

1.6 Recombination and transport timescales 9

1.7 Exciton binding energy 10

1.8 MAPI perovskite crystal structure 11

1.9 GaAs crystal structure 12

1.10 Schematic of pump-probe spectroscopy 14

1.11 Schematic of four wave mixing (FWM) coherent spectroscopy 15

1.12 FWM signals from homogeneously and inhomogeneously broadened transitions 17

1.13 Homogeneous and inhomogeneous broadening 18

1.14 Transient absorption measurement of hot carrier cooling . . . 21

2.1 Electronic band structure near k=0 24

2.2 Electronic band structure for GaAs and MAPI perovskite . . . 25

2.3 Rashba and Dresselhaus band splitting 28

2.4 Qualitative representation of the absorption spectrum in the vicinity of the band gap of a direct-gap semiconductor 30

2.5 Absorption spectrum of MAPI illustrating the role of inhomogeneous broadening 31

2.6 GaAs phonon dispersion showing the two acoustic and two optical branches 33

2.8 Dephasing of third order nonlinear optical response from a homogeneously broadened transition 38

2.9 Dephasing of third order nonlinear optical response from a inhomogeneously broadened transition 39

2.10 Continuum contribution (CC) signal from the exciton in Germanium 41

3.1 Perovskite thin-film characterization 45

3.2 Low-temperature grown GaAs and high-temperature grown GaAs optical absorption 46

3.3 Schematic of FWM apparatus 48

3.4 FWM signal analysis 49

3.5 Schematic of apparatus used for group velocity dispersion compensation setup 51

4.1 Schematic of FWM, and the FWM signal at 10 K as a function of energy and delay 57

4.2 Characterization of the $CH_3NH_3PbI_3$ films 59

4.3 FWM response of $CH_3NH_3PbI_3$ for varying laser tuning relative to band gap, and exciton resonance signals 60

4.4 FWM response of defect-bound exciton, and temperature dependence of E_g, and E_b 61

4.5 Schematic diagram of the two-pulse degenerate four-wave mixing apparatus 64

5.1 Transient four-wave mixing spectroscopy 70

5.2 Comparison of four-wave mixing response at 200 K from the $\mathrm{CH_3NH_3PbI_3}$ thin film and single crystal GaAs 72

5.3 Four-wave mixing results for $\mathrm{CH_3NH_3PbI_3}$, low-temperature-grown GaAs, and GaAs at 10 K 75

5.4 Electron-hole pair dephasing times versus the excited carrier density for $\mathrm{CH_3NH_3PbI_3}$, low-temperature-grown GaAs, and GaAs 76

5.5 SEM image of the $\mathrm{CH_3NH_3PbI_3}$ thin-film studied in this work. 84

5.6 Linear absorption spectra at 10 K for high-temperature-grown GaAs (HT-GaAs) and low-temperature-grown GaAs (LT-GaAs). 85

5.7 Schematic diagram of the four-wave mixing apparatus. 85

5.8 Four-wave mixing spectrum at zero delay (red curves) and excitation laser pulse spectrum (black curves) 86

5.9 Results of four-wave mixing experiments on $CH_3NH_3PbI_3$ at 10 K and Delay dependence of FWM signal at 1.653 eV (solid black curve) with fit 86

6.1 Schematic electron dispersion relation in the presence of Rashba coupling, four-wave mixing signal for two different temperatures, four-wave mixing signal versus interpulse delay and detection photon energy for various temperatures 91

6.2 Interband dephasing rate obtained from fits to the four-wave mixing signal 93

6.3 Results of theoretical simulations of the interband dephasing times 96

Abstract

Hybrid organic-inorganic perovskite materials have gained widespread interest in recent years due to the high solar cell efficiencies demonstrated using perovskite as the absorbing layer. These materials may be deposited with a low-cost solution processing technique, yet solar cell efficiencies as high as the commercial standard(made from Silicon, grown using an expensive, high temperature process) have been achieved. The surprising performance of perovskite solar cells leads to many open questions regarding the optoelectronic properties of these interesting materials. This thesis work aims to shed light on these optoelectronic properties of the archetypical perovskite material $CH_3NH_3PbI_3$ (MAPI) by applying the coherent optical technique of femtosecond four-wave mixing (FWM). In contrast to incoherent optical techniques such as transient absorption and photoluminescence, FWM probes coherence excited on the electron-hole pairs in the semiconductor, opening new opportunities to study the fundamental photo species and scattering processes.

We used FWM to directly determine the free exciton binding energy as well as the binding energy of excitons bound to shallow trap states in the MAPI system. Using FWM we were able to clearly decipher the exciton signal from the free-carrier continuum response, not apparent in incoherent spectroscopy signals due to the broadening associated with the soft nature of the organic-inorganic perovskite lattice. FWM was also used to measure the carrier-carrier scattering rate in MAPI thin-films, and was compared to GaAs. It was found that carrier-carrier scattering is much weaker in the MAPI system compared to GaAs over the carrier densities probed reflecting the operating densities in solar cells, resulting in a stark contrast between hybrid MAPI and the archetypical semiconductor GaAs. Finally, we used FWM to measure the dephasing time as a function of temperature, and as a function of excess energy near the bandgap. The results fit a model of electron-phonon scattering that included contributions from impurity scattering, and scattering by both acoustic phonons and optical phonons. These results show that for MAPI the recently-discovered Rashba effect enhances the rate of acoustic phonon scattering.

List of Abbreviations and Symbols Used

PV photovoltaic

MAPI methyl ammonium lead iodide

GaAs gallium arsenide

FWM four-wave mixing

VB valence band

BBO β barium borate

CB conduction band

TI-FWM time-integrated four-wave mixing

MBE molecular beam epitaxy

Ga gallium

As arsenide

InP indium phosphide

CdSe cadmium selenide

Ge germanium

InGaAs indium gallium arsenide

ZnSe zinc selenide

FPD free polarization decay

SR-FWM Spectrally-resolved four-wave mixing

Lt-GaAs low-temperature gallium arsenide

SOC Spin-orbit coupling

CC continuum contribution

EID Excitation induced dephasing

EIS excitation induced shift

XRD x-ray diffraction

SEM scanning electron microscopy

GVD group velocity dispersion

PbI2 lead iodide

DMF dimethylformamide

PTFE polytetrafluoroethylene

UV ultraviolet

FWHM full-width at half maximum

OBE Optical Bloch Equation

SHG second-harmonic generation

Acknowledgements

First, I would like to acknowledge my supervisor Professor Kimberley Hall. Without her constant and deliberate patience, I would have never puzzled this long. Thank you for the many years of support and guidance. As well, I would like to thank the many generations of Hall group members including Jen, Ye, Murat, Angela, Kerry, Lindsay, Nathan, Reuble, Colin, Tristan, Amy, Aaron, Jeremy, Daphne and especially Dan, Ajan, Seth, and Drew during these past few years for keeping me together or breaking me apart when necessary. Also I would like to thank Professor Ian Hill and his group including Jon-Paul, Charlotte, Irina, Alan and Eric for helping me traverse the wacky world of perovskite solar cell device fabrication.

Thank you to the office staff Tanya, Jen, Val, and Heather Anne, for everything from meandering the administrative hoops at Dalhousie, to the overall care and support given to grad students in the Physics department. Thanks to everybody in the machine shop including John, Kevin and Simon for helping with experiment design and fabrication. Thanks to Jim for understanding why my computer wouldn't turn on, and finally thanks to Andy for everything else experimental.

I would like to thank my folks Janette and Peter March, my brothers Andy and Forbes, and my extended family of uncles, aunts, and cousins. I am most grateful to Ma for teaching me to be reasonable, and to Pa for teaching me to be reasonably unreasonable. This thesis, and all of my work will always be dedicated to you both. Thank you to Andy for the late-night physics scheming, and to Forbes for providing the perspective on decisions that only a big brother can, and thank you Vanessa for keeping Forbes alive and well. Thank you to Mini-Mina, and Petey-Pablo, my niece and nephew for being amazing all the time.

Lastly and most importantly this thesis is dedicated to my partner in life Laura. Without her constant and unwavering support none of this would have been imaginable. Finally, thank you to my other family Julie and Greg Hambleton for taking care of us, to Lesley and Rob, baby Sam, Max, and Felicity, and to the rest of my friends and family that over the years have helped show me the way.

Chapter 1

Introduction

The un-checked burning of fossil-fuels has led our planet into a new era, where the human induced change in CO_2 and other greenhouse gas concentrations in our atmosphere has resulted in serious, and potentially catastrophic changes to the earth's climate. This research, and all renewable energy research has the goal to help us to stop emitting unnecessary, and dangerous greenhouse gases into the atmosphere. Solar, and other renewable energy technologies have proliferated in recent years thanks to early adopters, leading to renewable energy prices falling below fossil-fuel based energy prices in many markets thanks to cost reductions due to the economy of scale. This dramatic change in the energy market is clear as more renewable energy was installed in 2016 than fossil fuel based technologies [1].

In 2013 less than 1% of the world's energy supply came from all forms of solar energy production combined [2], generally due to a lack of investment. This situation is quickly changing, where in 2016 solar energy production rose to 2% of global energy production. The uptake of solar energy production is shown in figure 1.1, illustrating the cumulative installed capacity for solar photovoltaics (PV), that is dramatically increasing due to enormous investments by China, the US, and Japan. In 2017 multicrystalline silicon, and mono-crystalline silicon technologies accounted for roughly 95% of the solar PV market [3], shown in figure 1.2. Although silicon solar cell prices have, and will continue to dramatically drop, perovskite solar technologies offer a cheaper, and cleaner option compared to silicon [4]. Perovskite solar technologies attain similar efficiencies compared to silicon solar cells but are deposited from solution at low temperatures, and silicon technologies require energy intensive, high temperature processes to refine the silicon to a high enough crystal purity. As well, perovskite technologies have a host of novel applications. They are solution deposited, and can be fabricated on a variety of rigid, or flexible substrates including on flexible plastics, or can be building integrated as a film on windows, and building facades.

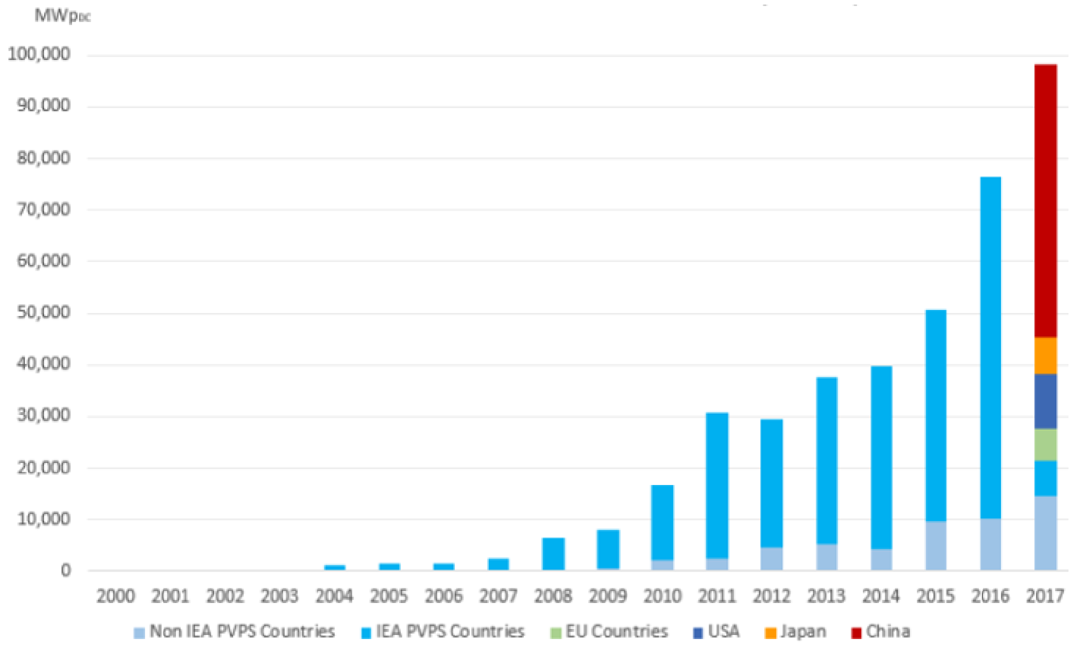

Figure 1.1: Worldwide cumulative solar installations by year, in megawatts peak (MW_p). Last year the dramatic rise in solar installations was due to large investments by Japan, United States, and China (reproduced with permission [2])

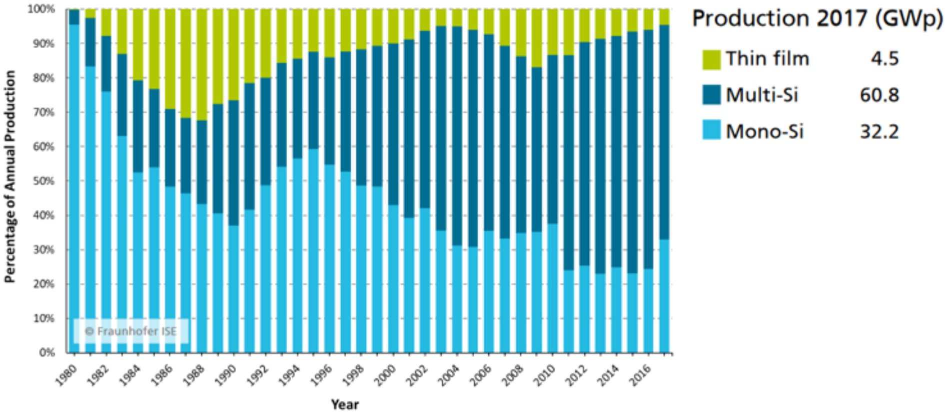

Figure 1.2: Solar module production by technology as a function of time. 95% of solar modules manufactured in 2017 were silicon based technologies, including 60.8% from Multicrystalline silicon, and 32.2% from Monocrystalline silicon. Only 4.5% of total solar mdules manufactured in 2017 were from thin-film technologies (reproduced with permission [3])

To get a larger perspective of the community of solar cell technologies, figure

1.3 shows the US NREL, or National Renewable Energy Labs "best Research-solar cell efficiencies chart" that charts the record efficiency rise over time of each solar photovoltaic technology. In blue, single junction silicon based technologies progress over 40 years to between 22.3% and 25.8% depending on the silicon crystal purity. In green, the thin-film technologies include CdTe and CIGS have reached efficiencies of 22-23%. In purple, the GaAs based solar cells have reached efficiencies of 28.8%, and tandem solar cells have reached 38.8% but usually find a home on satellites where the solar cell weight, and not its manufactured cost is the main applications constraint. In red, the emerging PV technologies include dye sensitized solar cells at 11.9%, organic solar cells at 11.5% and quantum dot solar cells at 13.4%. Perovskite solar cells are the red circles filled with yellow. The solar to electric efficiency has skyrocketed to 22.7% after 5 years of intense research, surpassing multicrystalline silicon efficiency of 22.3% that dominates the existing solar market. This marks the fastest rise in efficiency of any solar cell technology.

Hybrid organic-inorganic perovskite semiconductors offer a unique material platform combining ease of fabrication typical of organic semiconductors, with the efficient generation and transport of excited photo-carriers, typical of inorganic semiconductors. These intrinsic material properties make perovskite an ideal material candidate for developing an efficient and cheap solar photovoltaic energy production technology, low cost LEDs, photodetectors, and laser gain media [6–9].

Implemented as the absorber material in solar photovoltaic applications, perovskite has reached solar conversion efficiencies of 22.7% in 5 years of intense research [5] due in-part to the combined high absorption coefficient and long carrier diffusion length [10–12]. As a result, perovskite based materials have captivated the renewable energy industry world-wide as a potential low-cost alternative to expensive, and polluting fossil-fuels. This has stimulated an intense research effort into the fundamental photophysical properties of these materials to further optimize device performance [12–33].

A variety of perovskite materials have been further developed recently including multiple cation perovskites [34], all-inorganic perovskite [35], lead-free perovskite [36–38], 2D layered perovskite [39], as well as a variety of nanostructured material systems including quantum dots [40], nanowires [41], and nanoplatelets [42] that

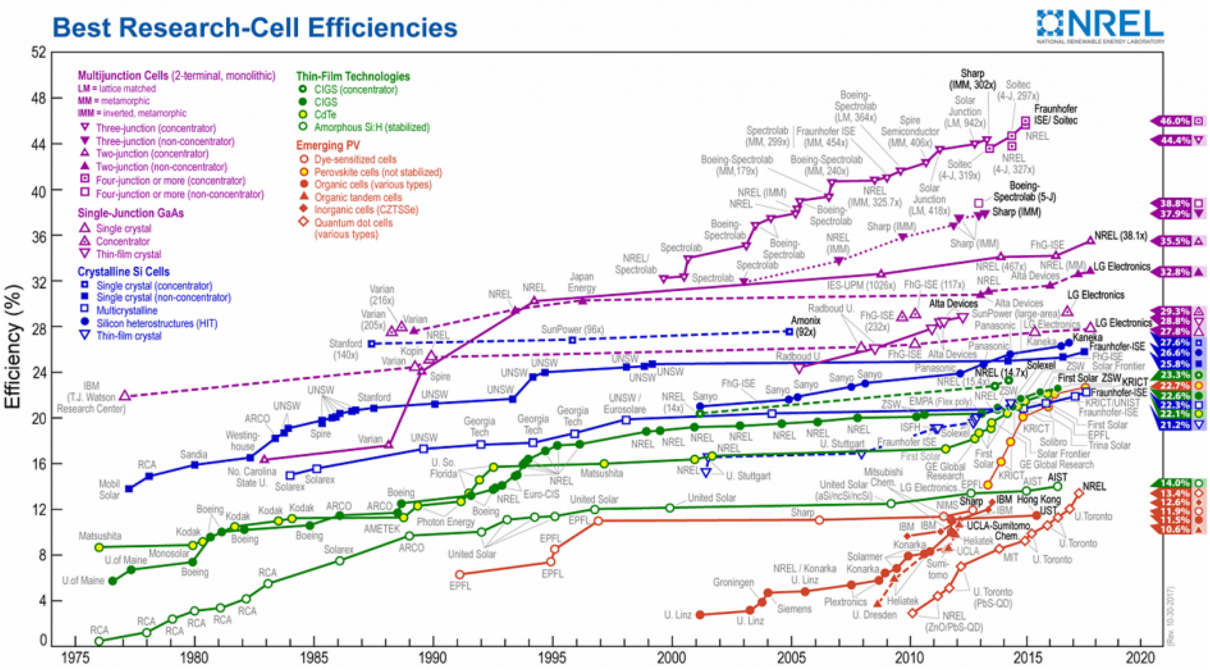

Figure 1.3: National Renewable Energy Labs (NREL) best research solar cell chart, that illustrates the record lab efficiency of solar technologies. In blue, single junction silicon based technologies have reached efficiencies of 21.2% and 25.8% depending on the silicon crystal purity. In green the thin-film technologies, CdTe and CIGS, have reached efficiencies of 22.6% and 22.1%. In purple, the GaAs based solar cells have the highest efficiencies for single-junction solar cells at 28.8%. In red, the emerging PV technologies including dye sensitized solar cells reaching 11.9%, organic solar cells at 11.5% and quantum dot solar cells at 13.4%. Perovskite solar cells are the red circles filled in with yellow. The solar to electric efficiency has reached 22.7% surpassing multicrystalline silicon efficiency of 22.3% (reproduced with permission [5])

offer a host of novel properties [43, 44]. Among these new materials, $CH_3NH_3PbI_3$ (methyl ammonium lead iodide (MAPI)) remains the archetypical perovskite material, and therefore understanding its photophysical properties is essential to lay the foundation for future materials engineering.

A broad body of work focused on the fundamental photophysical properties of MAPI perovskite utilizing a variety of spectroscopic techniques have been reported in recent years [45, 46]. These studies have contributed to a wealth of knowledge regarding photocarrier generation, relaxation, and diffusion, however a number of open questions remain. These include the value of the exciton binding energy that dictates the nature of carrier transport in solar cells at operating temperature, and the rate and type of dominant scattering processes for electrons and holes. These material properties have remained elusive in-part due to the soft nature of the hybrid organic-inorganic perovskite structure, tied to rotational and translational motions of the cations and anions in the lattice [22], giving rise to substantial inhomogeneous broadening of spectral transitions that can mask details in the absorption spectrum. In addition, prior to this thesis work ultrafast spectroscopy studies of perovskite were limited to incoherent techniques such as transient absorption. Incoherent spectroscopy methods probe the occupation of the band structure by electrons and holes. In contrast, the coherent four-wave mixing (four-wave mixing (FWM)) technique utilized in this work probes the coherent polarization response excited on the electron-hole pair transitions in the material. This opens up new opportunities to study carrier interactions and scattering processes. The objective of this thesis work is to explore what further insight can be gained into the photophysical properties of MAPI using FWM spectroscopy.

Due to it's high purity (using MBE), and high single junction solar cell efficiencies [5], the fundamental properties of gallium arsenide (GaAs) have been extensively investigated over several decades, resulting in a wealth of information regarding this archetypical inorganic solar cell material [47]. We utilized GaAs to compare and contrast the fundamental properties of MAPI to draw comparisons between the two systems, and to place MAPI in the context of other well known, high efficiency solar cell materials.

Utilizing FWM for the first time in this material system allowed us to clarify an ongoing debate regarding the value of the exciton binding energy, and to observe bound exciton states in the low temperature phase of MAPI [48]. This work is described in Chapter 4. In Chapter 5 we present a study that investigated the many-body interactions of excited carriers after photo-excitation in the MAPI system. The results were compared to GaAs in order to place MAPI in the context of existing photovoltaic materials [49]. Finally, in Chapter 6 we present a study that measured the dominant dephasing mechanisms at low temperature indicating the important role played by electron-phonon scattering. These studies constitute the first probe of the coherent carrier dynamics in hybrid organic-inorganic thin-film perovskite semiconductors and have stimulated a number of other groups to apply variants of four-wave mixing to MAPI in recent years [50, 51].

1.1 Optical Properties of Semiconductors

1.1.1 Bulk Semiconductor Properties

Semiconductors are used in optoelectronic devices, including the active layer in photovoltaics, photodiodes, and light-emitting diodes. The optoelectronic properties of semiconductors can be understood by considering the chemical constituents of the material, and the periodic structure that they form. The electronic structure of a semiconductor may be obtained by solving the Schrödinger equation.

$$\Big[-\frac{\hbar^2}{2m}\nabla^2 + V(\mathbf{r})\Big]\psi(\mathbf{r}) = E\psi(\mathbf{r}) \tag{1.1}$$

where V(r) is a periodic potential created by the ion cores in the crystal, that takes into account screening of the bare ions by all of the other electrons. The solution to equation (1.1) is a Bloch function,

$$\psi_{v,\mathbf{k}}(\mathbf{r}) = u_{v,\mathbf{k}}(\mathbf{r})\mathrm{e}^{-i\mathbf{k}\cdot\mathbf{r}} \tag{1.2}$$

that is a product of a plane wave with wavevector **k**, and a function $u_{v,\mathbf{k}}(\mathbf{r})$ that has the periodicity of the lattice. The subscripy v in equation 1.2 refers to a particular band v in the semiconductor. Due to coupling of the electrons with the periodic lattice potential, there are energies where no propagating electron states exist, called a band gap. This is the case when the electron wavelength is a multiple of 2 times the crystal lattice spacing and is known as the Bragg Scattering condition. The band diagram in the first Brillouin zone can be seen in figure 1.4 for MAPI perovskite. The highest occupied band is known as the valence band (VB), and the lowest unoccupied band is known as the conduction band (CB). In the case when the top of the valence band and the bottom of the conduction band occur at the same wave vector **k**, it is known as a direct-gap semiconductor.

When light with a frequency corresponding to an energy exceeding the band gap interacts with the semiconductor, an electron from the valence band can be promoted to the conduction band, leaving an electron vacancy in the valence band (known as a hole) as seen in figure 1.5. These electrons and holes constitute charge

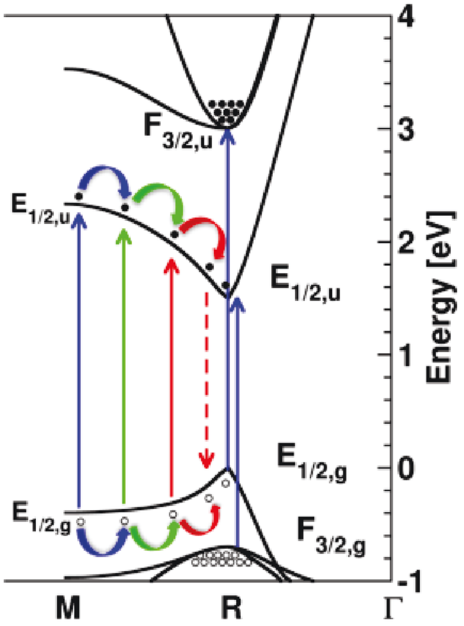

Figure 1.4: Band structure for perovskite that plots the energy versus wavevector in the first Brillouin zone (reproduced with permission [22]).

carriers in the semiconductor. In the presence of a bias, or a charge-carrier concentration gradient they produce a charge current flow. A photovoltaic device exploits the charge current flow created by optically-excited electrons and holes.

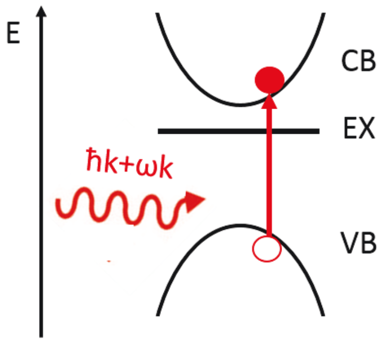

Figure 1.5: Absorption of a photon (with E = $\hbar\omega$) in a simplified band diagram for a direct band gap semiconductor that illustrates the generation of an electron in the CB, leaving a hole in the VB. The exciton state is also illustrated (EX)

1.1.2 Carrier Dynamics Following Photoexcitation

After photoexcitation, electrons and holes can undergo a complex cascade of scattering and relaxation processes before they recombine. For example, carriers can scatter with thermal excitations in the lattice (called phonons) or defects in the crystal (*e.g.* a missing atom, or vacancy). These carriers can also scatter with each other (many-body interactions). These scattering processes lead to an exchange of energy and momentum among the carriers and between the carriers and the lattice. These carrier dynamics can be divided into 4 regimes, representing overlapping timescales [47] and are shown in figure 1.6. The earliest is called the coherent regime ($\leq$200 fs). It describes the regime prior to the onset of scattering processes, in which the electron-hole pairs excited by the laser pulse have a well-defined (coherent) phase relationship with the pulse of light that excited them. The time that the carriers remain in this coherent state is known as the coherence time ($\mathbf{T}_2$). Any scattering process involving an electron or hole will interrupt the phase of the oscillating electron-hole pair leading to *dephasing* of the coherent signal. The second temporal regime is called the non-thermal regime ($\leq$2 ps). In this regime scattering processes have started to occur but the carrier distribution (i.e. the occupation versus energy) can not yet be described by a thermal distribution obeying Fermi statistics but is instead governed by the laser excitation energy. The third regime is known as the hot carrier regime (1-100 ps). In this regime the fastest scattering process is typically carrier-carrier scattering, which leads to a redistribution of the carrier energies, ultimately forming a thermal distribution, but at an elevated temperature compared to the lattice. The temperature of the distribution is determined by the excess energy of the absorbed photon relative to the bandgap. Finally, the isothermal regime ($\geq$100 ps) corresponds to carriers and phonons in equilibrium, so that the carriers and the lattice are at the same temperature. After the carriers have scattered and cooled, they either recombine radiatively by emitting a photon, or non-radiatively (*e.g.* by getting trapped in ‘dark states’ prior to recombining). The lifetime of the excited carrier is known as the $\mathbf{T}_1$ time.

During carrier cooling, and after an equilibrium with the lattice has been achieved the carriers undergo a variety of processes in a photovoltaic (PV) device. These mechanisms and their timescales are also illustrated in figure 1.6.

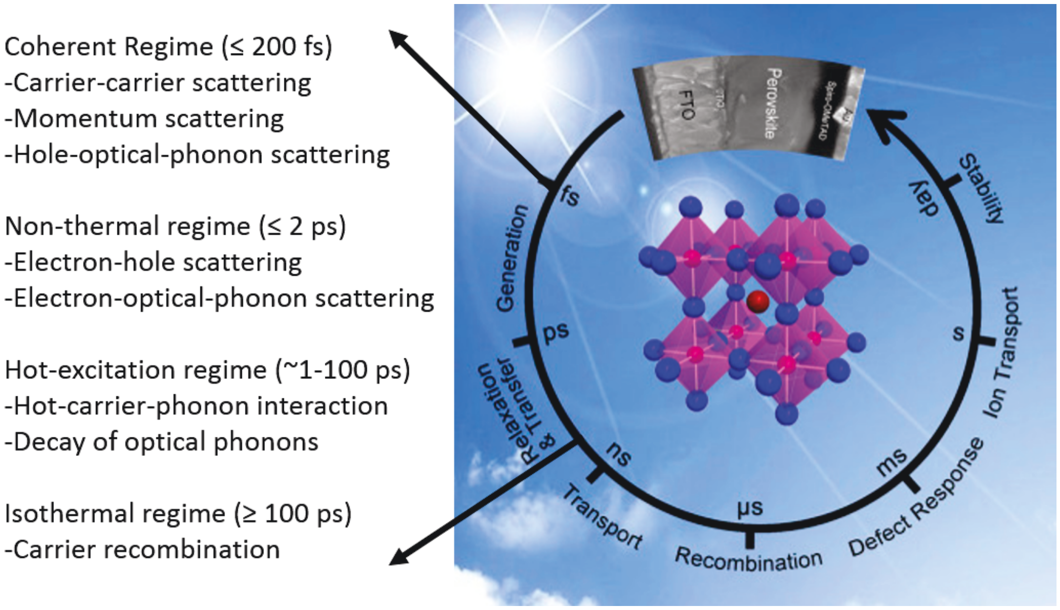

Figure 1.6: Left: Ultrafast photophysical timescales in phtoexcited semiconductors including scattering and relaxation processes for each regime including the coherent regime, the non-thermal regime, the hot-excitation regime, and the isothermal regime. Right: Timescales for the various photophysical mechanisms in perovskite PV devices including charge generation, Relaxation and charge transfer, charge transport, recombination, defect response, ion transport, and finally long term device stability (reproduced with permission [52].)

Due to the opposite charge of the electrons and holes, there exists an attractive Coulomb interaction between them. This leads to bound states of electron-hole pairs, called *excitons* (see figure 1.7a). An exciton is similar to a hydrogen atom, but has a much larger Bohr radius. The energy that binds a single electron-hole pair is referred to as the exciton-binding energy (E_B) seen in figure 1.7(b). The relationship between the binding energy and the Bohr radius is,

$$E_B = \frac{\hbar^2}{2m^* a_B^2} \tag{1.3}$$

where $a_B = \frac{\hbar^2 \epsilon}{m^* e^2}$ is the Bohr radius, m^* is the effective mass, and ϵ is the dielectric constant. How tightly an exciton is bound (and correspondingly, how large is it's exciton Bohr radius) depends on the dielectric constant within the crystal. If the exciton binding energy is large (*e.g.* 100 meV) the exciton is known as a Frenkel exciton, a situation common in organic semiconductors. If the binding energy is below 10 meV, it is known as a Wannier exciton. Wannier excitons are more common in inorganic semiconductors. For example, GaAs has an exciton binding energy of 4 meV. The exciton binding energy plays a large role in the transport properties of any semiconductor system. If the exciton binding energy is large compared to the thermal energy k_BT (25.7 meV at room temperature), where k_B is the boltzman constant and T is the operating temperature of the device, transport is limited by the diffusion of *excitons*. In contrast if $E_b < k_B T$, transport is governed by the drift and diffusion of separated electrons and holes know as *free carriers* that are highly mobile compared to excitons.

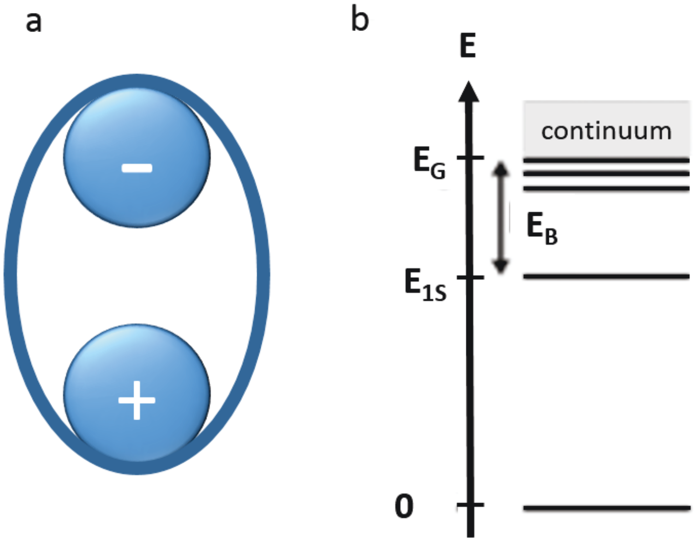

Figure 1.7: (a) Schematic illustration of an exciton shown as an electron-hole pair bound by the Coulomb interactions. (b) Spectrum of discrete exciton energy levels below the bandgap, and the continuum of unbound electron hole pair transitions above the band gap.

1.2 Materials

1.2.1 $CH_3NH_3PbI_3$ (MAPI) Perovskite Semiconductor

Perovskite refers to any system that forms a crystal structure of the form ABX_3 with corner-sharing octahedra. This structure was named after a famous Russian mineralogist Count Lev Aleksevich von Perovski after the first crystal with the ABX_3 structure was discovered by Gustav Rose in the Ural Mountains in 1839. Perovskite was first implemented as the solar absorber material in a dye-sensitized solar cell device structure in 2009 by Tsutomu Miyasaka *et al.* [53]. This promising first result generated what has become a landslide of research regarding this particular material system in the past 5 years. For the archetypical perovskite system (MAPI), methyl ammonium serves as the organic A-site ion, lead as the inorganic B-site ion, and iodide as the inorganic X-site ion. The perovskite structure has been found to have a stable crystal structure with a variety of interchangeable chemical constituents playing the role of A, B and X, [54] leading to highly tunable optoelectronic properties. For example, the bandgap of various material combinations spans the wavelength range from 400 nm (perovskite quantum dots) to 700 nm (bulk perovskite) [44].

MAPI Perovskite forms a pseudo cubic crystal structure that is tetragonal near room temperature, cubic at high temperature (above 325°K), and orthorhombic at reduced temperature (below 160 °K). The unit cell for MAPI is shown in figure 1.8. Methylammonium cations reside on the eight corners of the unit cell. A lead cation occupies the central position in the unit cell, and is surrounded by six iodine anions. MAPI has a relatively high optical absorption coefficient [12], and has a carrier diffusion length on the order of 1 micron at room temperature [11]. Recently, direct and indirect optical absorption have been experimentally verified [55], and potentially contribute to a host of interesting optoelectronic phenomena in this complex material system [56].

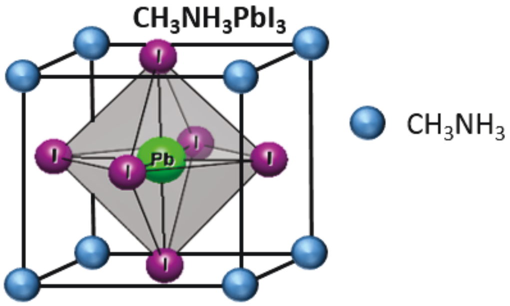

Figure 1.8: Perovskite's chemical constituents form an ABX_3 composition with corner-sharing octahedra, where for the archetypical perovskite MAPI, Methylammonium is the A-site cation, Lead is the B-site cation, and Iodide is the X-site anion.

1.2.2 The Prototypical III-V semiconductor: GaAs

Gallium Arsenide (GaAs) is an important example of an inorganic semiconductor to contrast with MAPI because it is used in some of the highest efficiency inorganic solar cells [5]. GaAs also provides an ideal material system for studying ultrafast carrier relaxation in inorganic semiconductors due in part to the high crystal purity that is achieved using molecular beam epitaxy (MBE) to grow single crystal GaAs. MBE deposits a molecular layer of material at a time in high vacuum, resulting in defect densities $\leq 10^{13}$ cm^{-3} for GaAs when grown at high temperatures (600 °C) [57,58]. The crystal structure of GaAs is zincblende. The primitive basis consists of a GaAs molecule. The overall structure may be viewed as two offset face centered cubic structures of gallium (Ga) and arsenide (As) seen in figure 1.9(a). To study the effects of defects in this archetypical inorganic system, defect concentrations can be increased by reducing the substrate temperature during MBE growth. For instance, when the growth temperature is in the range 200-300 °C, the resulting material is known as low-temperature gallium arsenide (Lt-GaAs). The defects have been shown to result from As interstitial incorporation [59,60] seen in figure 1.9(b).

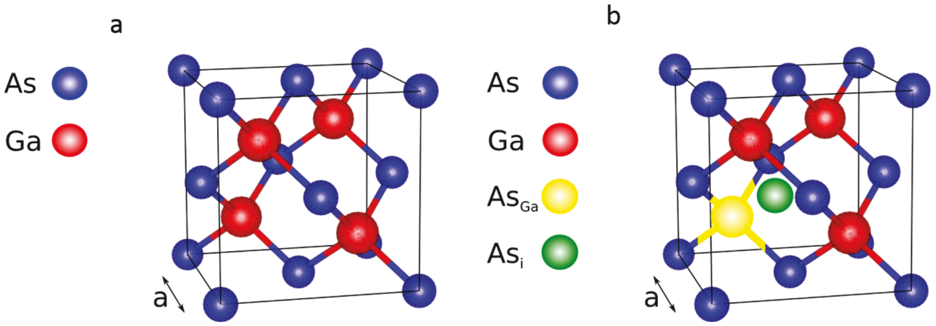

Figure 1.9: (a) Zinc-blende GaAs grown at high temperature (Ht-GaAs), and (b) zinc-blende GaAs grown at low temperature (Lt-GaAs) with As interstitial defects.

1.3 Optical Spectroscopy

A variety of spectroscopy techniques have been utilized to study the optical properties of perovskite semiconductors. Steady-state techniques include absorption and photoluminescence spectroscopy. In absorption spectroscopy, the transmission coefficient (typically of a thin film) is measured as a function of incident photon energy. In photoluminescence, light above band gap is used to excite the semiconductor and the radiation resulting from the radiative recombination of electron-hole pairs is detected. These techniques are often utilized to characterize optical bandgaps [23, 61].

To monitor temporal dynamics of charge-carriers, pulses of light are utilized. In the case of ultrafast spectroscopy techniques, the duration of the laser pulses used is $\sim$100 fs. Ultrafrast spectroscopy techniques can be broadly classified based on the type of information that they provide about the electron-hole pairs excited in the system by the optical pulse. Incoherent techniques probe the occupation of the band edge states by carriers. These include pump-probe and time-resolved photoluminescence.

In a pump-probe experiment (fig. 1.10), a strong ‘pump’ pulse excites carriers in a material, and a second weaker ‘probe’ pulse measures the change in absorption due to the injected carriers. This is often referred to as a transient absorption experiment. As a result of the Pauli exclusion principle, the probe absorption is reduced when electrons or holes occupy the band states coupled by the light at the probed photon energy. As carriers scatter and/or relax out of these states, the absorption recovers. The timescale for the relaxation is measured by varying the time-delay of the probe pulse relative to the pump pulse. One can use a broadband probe pulse to detect the occupation of states over a wide range of transition energies at each interpulse delay. In time-resolved photoluminescence, a laser pulse is used to excite the semiconductor, and the amount of photoluminescence is measured as a function of time after excitation. Both transient absorption and time-resolved photoluminescence are incoherent because they only probe the level of *occupation* states in the optically coupled region of the band.

Coherent spectroscopy describes a class of experiments that are sensitive to the presence of coherence in the system of electron-hole pairs. Each electron-hole pair can be considered as an oscillating dipole, with a frequency dictated by the transition energy. Before any scattering events occur, the phase of this oscillator is well defined and dictated by the electric field of the pulse that excited it. All of these oscillators together create a macroscopic polarization on the interband transitions. Coherent techniques probe this polarization in addition to the carrier occupation.

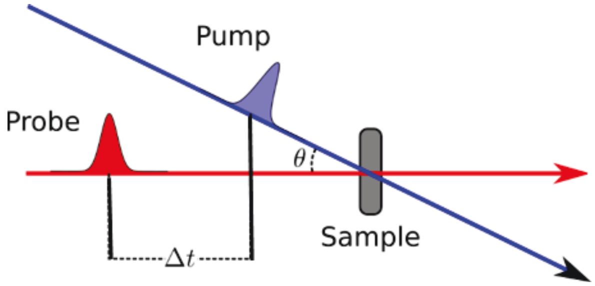

Figure 1.10: Illustration of pump-probe spectroscopy. The strong pump pulse excites a population of carriers above the bandedge, and the weak probe pulse monitors the generated excited carrier population at a time delay Δt after photoexcitation.

Coherent spectroscopy has been used for decades to study carrier dynamics in traditional semiconductors [47].

1.3.1 Four-Wave Mixing Spectroscopy (FWM)

FWM experiments, which are used in this thesis work, probe the coherent polarization response of excited electron-hole pairs. There are a variety of FWM techniques. In this work, two-beam degenerate four-wave mixing is used, where two spectrally and temporally identical pulses with electric fields $\mathbf{E}_1$ and $\mathbf{E}_2$ and wave vectors $\mathbf{k}_1$ and $\mathbf{k}_2$, are focused onto the sample. The two beams are focused in a non-collinear geometry as shown in figure 1.11. One can develop an understanding of how this technique probes the coherent polarization by considering first the case in which the two pulses are incident on the sample at the same time. In this case, the electric fields of the pulses interfere, resulting in fringes (regions of high and low light intensity) across the sample along the x direction. These light fringes result in a spatially modulated carrier density. The index of refraction is modified by the presence of carriers and the excited semiconductor sample acts as an optical diffraction grating. In the experiment, the diffraction of a portion of the second pulse $\mathbf{E}_2$ is measured. This diffracted light corresponds to the emission from a third order optical polarization with wave vector $2\mathbf{k}_2$-$\mathbf{k}_1$, and the total amount of this light corresponds to the FWM signal. Next we consider the case where pulse $\mathbf{E}_2$ arrives a time delay τ after $\mathbf{E}_1$. In this case, a diffraction grating may still be generated provided the polarization excited by the first pulse remains coherent by the time the second pulse arrives (*i.e.* as long as the individual electron-hole pair oscillators retain their phase). In the experiment, the time-averaged signal at $2\mathbf{k}_2$-$\mathbf{k}_1$ is detected at each value of interpulse delay τ, known as time-integrated four-wave mixing (TI-FWM). For a simple two-level system neglecting interactions between the charge carriers this signal decays exponentially, at a rate determined by the dephasing time ($\mathbf{T}_2$) of the electron-hole pairs.

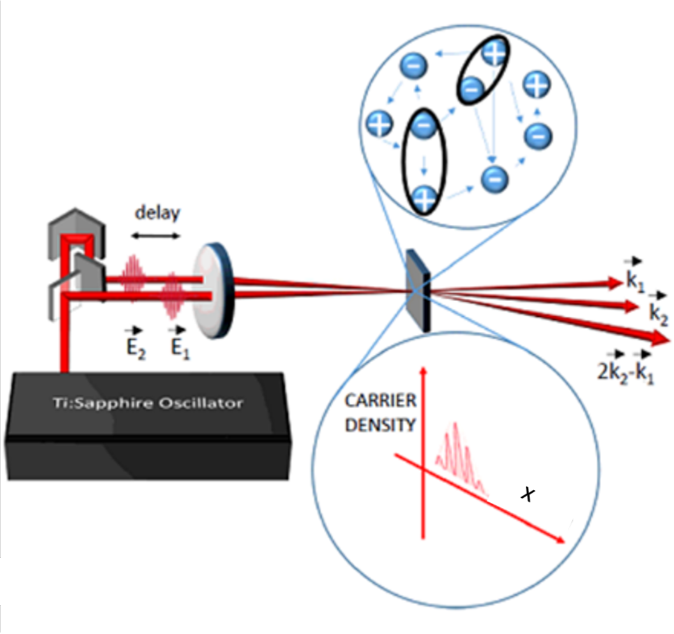

Figure 1.11: Illustration of the FWM apparatus. Ultrafast optical pulses from a Ti:Sapph oscillator laser source excite a carrier-induced grating. Self-deffraction of the pulse E_2 results in a signal that propagates along $2\mathbf{k}_2$-$\mathbf{k}_1$ and is proportional to the coherence after photo-excitation.

Yajima and Taira successfully interpreted the FWM signal contributions due to homogeneously, and inhomogeneously broadened transitions [62] leading to a flurry of experiments to understand the ultrafast relaxation mechanisms in a variety of semiconductor systems over several decades including GaAs [63–70], indium phosphide (InP) [71,72], cadmium selenide (CdSe) [73–75] , germanium (Ge) [76, 77], and nanostructured materials like GaAs quantum wells [74, 75, 78, 79, 79–84], indium gallium arsenide (InGaAs) multiple quantum wells [85], and zinc selenide (ZnSe) multiple quantum wells [86]. Homogeneously broadened transitions that arise from transitions between discrete energy levels (*eg.* the exciton transition below the band gap) have a linewidth dictated by the total rate of collisions of the carriers (*ie.* the dephasing rate). The FWM signal from a homogeneously broadened transition is known as free polarization decay (FPD) and is shown in figure 1.12 (a, b). Inhomogeneously broadened transitions above the band gap arise from a continuum of energy levels (*e.g.* unbound electron-hole pairs). The FWM signal from an inhomogeneously broadened transition is known as a photon echo. Such a FWM signal is shown in figure 1.12 (c, d). For a homogeneously-broadened transition, the FWM signal is generated at the time that the second pulse arrives, and decays exponentially versus time at a rate $\frac{1}{T_2}$. The decay of the time-integrated signal also decays at a rate $\frac{1}{T_2}$ versus interpulse delay. For an inhomogeneously-broadened transition, the signal versus time arises from a rephasing of the polarization contributions from the individual transitions within the continuum, which occurs at $t = t_2 + \tau$. The time-integrated signal decays versus τ at a rate $\frac{2}{T_2}$. The T_2 time for either type of transition may be extracted from the time-integrated FWM signal versus delay τ. The photon echo is analogous to the spin-echo in nuclear magnetic resonance measurements, although the FWM signal arises from the re-phasing of electron-hole dipoles. Spectrally-resolved four-wave mixing (SR-FWM) utilizes a monochromator to measure the photon energy spectrum of the FWM signal.

The above describes the FWM signals in the absence of interactions between electron-hole pairs. The FWM signal in this case may be thought of as a self-diffraction of the second laser pulse from the carrier density grating. When interactions between charge carriers are present, additional contributions to the FWM signal may be generated tied to diffraction of the polarization density excited by E_2. Such many-body related four-wave signals occur when the dephasing rate or transition energy depends on the density of electron-hole pairs. Such signals can be very strong at the excitonic transitions in semiconductors.

A large body of literature exists focused on the application of this technique to III-V semiconductors [47]. These studies have given insight into the interactions leading to dephasing of electron-hole pairs in traditional semiconductors. This body of literature provides the basis for interpreting the FWM response of perovskite in this thesis work.

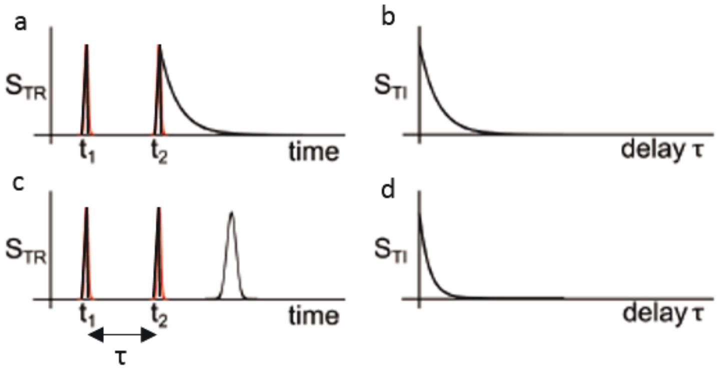

Figure 1.12: (a) Time-resolved (TR) FWM signal from a homogeneously broadened transition (b) and time-integrated (TI) FWM signal from a homogeneously broadened transition. (c) TR-FWM signal from the inhomogeneously broadened transition, and (d) TI-FWM signal from an inhomogeneously broadened transition (reproduced with permission [87]).

1.4 Literature Review

This section places the current thesis work within a broader context by exploring the existing literature relevant for each thesis project in section 1.4.1, section 1.4.2, and section 1.4.3. A summary of the thesis accomplishments is provided in section 1.5.1.

1.4.1 Exciton Binding Energies in MAPI Perovskite

The exciton binding energy is an important material parameter as it dictates the primary mode of carrier transport. At the time of this study, a conclusive value for this parameter was still under debate where values in the literature ranged from 2 meV to 55 meV [13–15, 18–28, 32, 33]. The exciton binding energy has remained controversial in part due to the presence of defects in the perovskite lattice [88], and dynamic disorder due to the correlated rotations of the methylammonium ions [89, 90]. Defects, together with the dynamic degrees of rotational and translational freedom of the chemical constituents in the crystal lattice, modify the local environment for electron-hole pairs, leading to a spatially-dependent variation in the transition energy at each **k**, resulting in several closely spaced transitions (figure 1.13). Both of these effects lead to a broadening of the optical transitions in the semiconductor, obscuring the exciton transition just below the band gap. The amount of broadening in the perovskite system has been found to vary from 30 meV at cryogenic temperatures to 60 meV at room temperature [24]. This level of broadening is comparable to the exciton binding energy, rendering simple measurement of the exciton binding energy difficult using the incoherent spectroscopy technique of linear absorption [25]. It is also difficult to extract the exciton binding energy from photoluminescence experiments. Photoluminescence provides an effective probe of recombination processes, however, recombination of carriers localized on defects can dominate the emission making it hard to determine the intrinsic exciton transition energy [16, 17] *i. e.* to separate defect-bound excitons, from free excitons. The defect-bound exciton emission occurs at lower energy than that of free excitons.

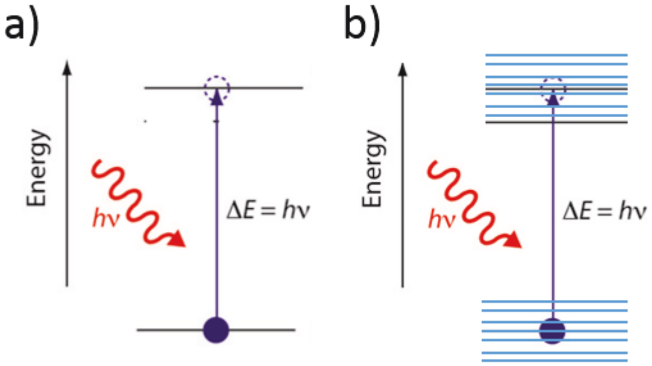

Figure 1.13: (a) Homogeneously-broadened transition. (b) Inhomogeneously broadened transition.

For TI-FWM from a homogeneously-broadened transition such as an exciton, the magnitude of the FWM response is proportional to the dephasing time T_2. As a result the FWM signal from spatially-localized charge-neutral excitons is enhanced compared to spatially-delocalized free carrier and band tail transitions [47, 91]. In addition, many-body interactions lead to additional contributions to the FWM at the exciton, whereas such signals are weak from the interband continuum. As a result, FWM is highly sensitive to exciton signals. This feature has for example been used to analyze excitons in Lt-GaAs. In Lt-GaAs the exciton signal is not visible in linear absorption due to strong broadening in the optical response. In contrast, using FWM spectroscopy, the exciton resonance was clearly visible due to the strong exciton many-body signal that emerged in addition to the photon echo from the interband continuum [70]. A similar situation occurs at the onset of transitions involving the spin-orbit split off valence band in III-V semiconductors. In this case, the exciton tied to the spin-orbit split off valence band to conduction band transition is resonant with the interband transitions associated with the lower energy heavy-hole and light-hole valence bands. As a result, this excitation resonance is not visible in linear absorption. It is clearly visible in FWM, however as shown in Ref [72], because of a strong many-body signal that contributes the the FWM signal. In this thesis work, one of the objectives was to utilize the sensitivity of FWM to gain further insight into the exciton resonance in perovskite.

1.4.2 Carrier-Carrier Scattering in GaAs and MAPI Perovskite

Many-body interactions are mediated by the Coulomb interaction, which provides a long range coupling between charge carriers. The strength of this interaction depends on the dielectric constant of the semiconductor. Prior to this thesis work, the strength of many-body interactions in MAPI was not known. This is due in part to the complexity involved in predicting the frequency dependence of the dielectric constant, for which a large number of phonon modes contribute due to the large size of the unit cell in perovskite.

GaAs provides an ideal material system for studying many-body interactions due to the high purity of the refined MBE growth process developed over several decades. Over the past three decades, FWM experiments have been applied to study many-body coupling in GaAs and related materials (*eg.* GaAs quantum wells). One of the original works was by Schultheis *et al.* [63], who measured the dependence of the dephasing rate on the density of electron-hole pairs by measuring the T_2 time in the presence of additional pulse that arrived prior to the two FWM pulses. In the years that followed many additional experiments have been carried out to gain insight into the interactions between excitons (exciton-exciton scattering, biexcitons) and the scattering of excitons with free carriers.

In this study we compared the coherent optical response of MAPI thin films and GaAs using FWM spectroscopy to provide insight into the strength of many-body effects in MAPI. We measured the interband dephasing time (T_2) and found that carrier-carrier scattering is much weaker in MAPI compared to GaAs illustrating a fundamental difference between hybrid MAPI and fully inorganic semiconductor systems.

1.4.3 Carrier-phonon Scattering in MAPI Perovskite

Coupling of charge carriers with thermal fluctuations of the crystal lattice is central to the operation of PV and other optoelectronic devices because scattering of electrons with phonons provides a source of resistance to current flow. Electron coupling to phonons also represents a pathway for hot electrons (*i.e.* electrons optically-excited far above band gap) to lose energy and relax down to the band edge. For this reason, a considerable effort has focused in recent years on understanding the nature of the phonon modes in perovskite [92–94], as well as to determine the rate of carrier cooling [95, 96].

An understanding of these effects is complicated in the perovskite by the large number of phonon modes [92–94], owing to the large number of atoms in the primitive basis. Pump-probe (transient absorption) spectroscopy has been applied to study carrier cooling [95, 96]. Such experiments allow the effective temperature of the charge carriers to be assessed from a measurement of the population of carriers as a function of energy above the band gap. An example of the results of such a study is shown in figure 1.14. This study revealed a slowing of the carrier cooling process due to the generation of large occupations of optical phonons.

In transient absorption, carrier-phonon coupling is monitored only indirectly by monitoring the average carrier temperature as a function of time following excitation, which evolves through a cascade of individual scattering events. In this thesis work, the rate of scattering of electrons with phonons was measured in MAPI by studying the interband dephasing time as a function of temperature. The advantage of four-wave mixing in this context is that it provides a direct time-based probe of phonon scattering.

The experiments reveal a dependence of T_2 on temperature, indicating that scattering with phonons contributes to interband dephasing. This temperature dependence was modeled by Zhi-Gang Yu (Washington State University) including scattering with both acoustic phonons and polar optical phonons. This model provides

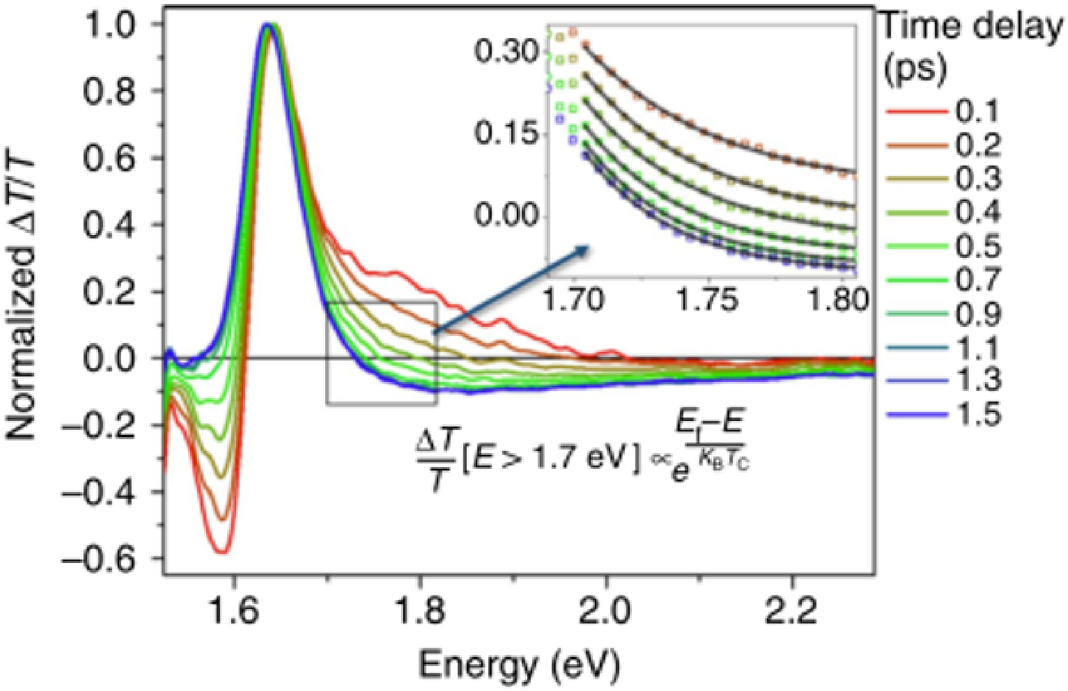

Figure 1.14: Transient absorption spectra of MAPI pumped at 2.25 eV (pump resolution ~200 fs), with an initial (t=0) average carrier density of N = 6.4 x 10^{17} cm^{-3} over the illuminated area. Spectral broadening at early times (before 2.5 ps) indicated hot-carrier distributions. Inset: cooling rates were obtained from a global fit of the high-energy tail of each timeslice between E=1.7 and 1.85 eV to a Boltzman distribution. (reproduced with permission [96])

quantitative agreement and indicates that the rapid acoustic phonon scattering we observe (110 fs) results from an enhancement of the density of states at the edges of the valence band and conduction band caused by the Rashba effect. The Rashba effect corresponds to a splitting of the spin states in each band due to the spin-orbit interaction [97].

1.5 Overview of Thesis

To summarize the contributions made in this thesis, we used FWM to directly determine the free exciton binding energy as well as the binding energy of excitons bound to shallow trap states in the MAPI system. As FWM measures the third order optical response of the system of electron-hole pairs, we were able to clearly decipher the exciton signal from the free-carrier continuum response, not apparent in incoherent spectroscopy signals due to the broadening associated with the soft nature of the organic-inorganic perovskite lattice. FWM was also used to measure the carrier-carrier scattering rate in MAPI thin-films, and was compared to GaAs. It was found that carrier-carrier scattering is much weaker in the MAPI system compared to GaAs over the carrier densities probed reflecting the operating densities in solar cells. This result was attributed to screening of the Coulomb interaction tied to the dynamic disorder in the soft MAPI crystal lattice, resulting in a stark contrast between hybrid MAPI and the archetypical semiconductor GaAs. We also found that the scattering rate between excitons and free-carriers is much weaker than in GaAs. Finally, we used FWM to measure the T_2 time as a function of temperature, and as a function of excess energy near the bandgap. The results fit a model of electron-phonon scattering that included contributions from impurity scattering, and scattering by both acoustic phonon and optical phonons. These results show that for MAPI the recently-discovered Rashba effect enhances the rate of acoustic phonon scattering.

1.5.1 Structure of the Thesis

This document will present the projects that constitute the author's thesis. Chapter 2 describes the relevant background information. Chapter 3 discusses the experimental methods utilized. Chapter 4 presents a study in which we simultaneously measured the free and defect bound exciton binding energies in MAPI perovskite. This study was published in Scientific Reports. Chapter 5 presents a study that reported the weak many-body interactions in MAPI compared to GaAs, and was published in ACS Photonics. Chapter 6 presents a study that reported a measurement of the rate of electron-phnon scattering in the MAPI system and is under preparation for submission to Applied Physics Letters. Conclusions and future outlook are presented in Chapter 7.

Chapter 2

Background and Theory

This chapter provides the theoretical background necessary to understand the projects carried out in this thesis work. Section 2.1 introduces semiconductor electronic structure, optical absorption, and carrier scattering. Section 2.2 presents the theoretical considerations utilized to analyze FWM spectroscopy, and the scattering mechanisms that lead to dephasing.

2.1 Electronic Structure and Optical Properties of III-V Semiconductors

We focus our attention first on the archetypical inorganic semiconductor GaAs. Due to the refined deposition techniques allowing for exceptionally low defect concentrations, GaAs has served as an ideal material system for studying fundamental properties including coherent relaxation dynamics for decades. GaAs has a zinc-blende crystal structure (Fig. 1.9) that is composed of offset face-centred cubic crystals for each of the constituents Ga and As.

Very near to the band extrema in a semiconductor, the dispersion relation is approximately parabolic. We can then write the dispersion relation in the same form as that for a free electron (or hole), but with the bare electron mass replaced by an effective mass. This is known as the effective mass approximation, and the conduction and valence energy eigenvalues are then:

$$\begin{aligned} E_{\mathrm{c},\mathbf{k}} &= E_g + \frac{\hbar^2 k^2}{2m_c^*}, \\ E_{\mathrm{v},\mathbf{k}} &= -\frac{\hbar^2 k^2}{2m_v^*}. \end{aligned} \tag{2.1}$$

The band structure in a semiconductor is strongly affected by Spin-orbit coupling (SOC). This coupling describes the interaction of the electron intrinsic angular momentum, or spin (S), and the effective magnetic field generated by the motion of the electron tied to its orbital angular momentum ($\mathbf{L}$). The spin-orbit coupling is described by the Hamiltonian:

$$H_{SO} = \frac{\hbar}{4m^2c^2}\nabla V \times \mathbf{p} \cdot \sigma \tag{2.2}$$

where V is the periodic potential from Eqn. 1.1, $\mathbf{p} = i\hbar\bigtriangledown$, and σ are the Pauli matrices. The cell functions $u_{\nu,\mathbf{k}}(\mathbf{r})$ (Eqn. 1.2) for each band in the semiconductor describe the orbitals corresponding to states of total angular momentum ($\vec{J}$=$\vec{L}$+$\vec{S}$) $|j, m_j\rangle$. The simplified band structure of a III-V semiconductor such as GaAs is shown in figure 2.1. For the conduction band, the angular momentum of the electron $l = 0$ and the spin $s = 1/2$, while for the valence band $l = 1$ and $s = 1/2$. The top most valence bands are the heavy-hole ($j = 3/2$, $m_j = \pm3/2$), light-hole ($j = 3/2$, $m_j = \pm1/2$), and spin-orbit split-off bands ($j = 1/2$, $m_j = \pm1/2$). The SOC lifts the degeneracy of the valence bands with $j = 3/2$ and $j = 1/2$. This splitting is labelled $\triangle$ in figure 2.1. The conduction band is characterized by $j = 1/2$ and $m_j = \pm1/2$.

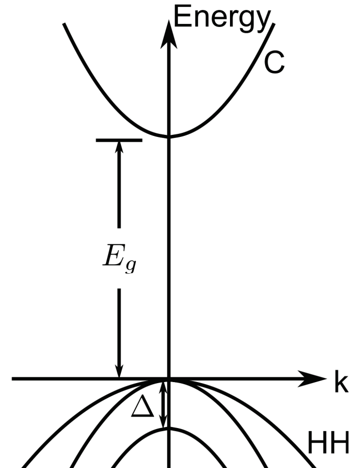

Figure 2.1: Schematic of the band structure of a III-V semiconductor such as GaAs in the vicinity of the band gap, showing the C band, HH band, LH band, and SO band. The band gap E_g and the split-off energy Δ are indicated.

The band structure of perovskite is similar to that of GaAs, except that the conduction band cell functions correspond to $l = 1$ and $s = 1/2$, and the valence band has $l = 0$ and $s = 1/2$. This leads to a band structure that has been referred to as "“reversed"” [98]. In this case, the relevant bands are the bottom three conduction bands, which correspond to the projections of total angular momentum with $l = 1$, and the top valence band with $l = 0$. Spin-orbit coupling in this case lifts the degeneracy of the $j = 3/2$ and $j = 1/2$ conduction bands so that the lowest conduction band (which is the conduction band involved in optical excitation and transport) is analogous to the spin-orbit split off valence band in GaAs, characterized by $j = 1/2$ and $m_j = \pm 1/2$. The full band structures of GaAs and perovskite are shown in figure 2.2. Spin-orbit coupling is much larger in perovskite than in GaAs, so the band splitting Δ in the conduction band is also much larger ($\approx$ 1 eV in perovskite [99]) compared to the splitting in the valence band of GaAs (340 meV [100]).

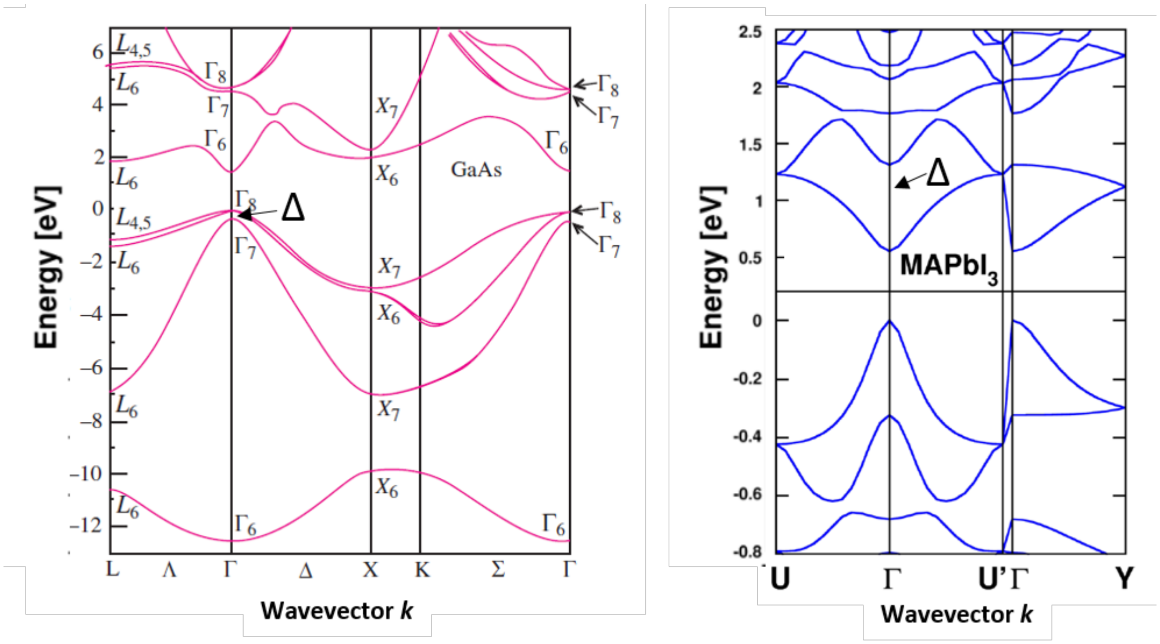

Figure 2.2: Electronic band structure of GaAs (reproduced with permission [101], and MAPI perovskite (reproduced with permission [102]). Δ illustrates the split-off energy

In addition to lifting the degeneracy of the total angular momentum eigenstates (Δ in figure 2.1), the spin-orbit interaction can also lead to more subtle effects on the band structure of the semiconductor [97,99]. When the crystal structure is non-centrosymmetric, the SOC lifts the degeneracy of the two spin projections in each band (for example, the $m_j = \pm 1/2$ states in the conduction band of perovskite) away from high symmetry points. Contributions to these band "‘spin splittings"’ are categorized according to the source of inversion asymmetry. For example, the crystal structure of GaAs is noncentrosymmetric because of the net charge on the Ga and As atoms. Silicon, in contrast, is centrosymmetric, with the centre of inversion symmetry at the midpoint of the bond between the two Silicon atoms in the primitive basis. Inversion symmetry breaking intrinsic to the crystal structure is referred to as bulk inversion asymmetry. It is also possible to "‘build-in"’ asymmetry by growing a layered structure with varying composition or to dynamically introduce inversion asymmetry by applying an external electric field.

In the case of III-V semiconductors, these effects of SOC have been extensively studied. Dresselhaus analysed the case of a III-V quantum well grown in the (100) crystal direction [103]. (A quantum well, is a thin layer of semiconductor with barriers on the top and bottom that confines the motion of electrons and holes to the plane of the well). Bychkov and Rashba analyzed the case of a two-dimensional electron gas (such as a doped semiconductor quantum well) under symmetry breaking along the direction perpendicular to the transport plane [104]. The size of the spin splittings in a particular material are determined by the size of the spin-orbit coupling and the degree of symmetry breaking. The presence of inversion asymmetry in any of the above cases can be understood as the existence of electric fields within the crystal (representing a non-zero ∇V in Eqn. 2.2). Unlike the established literature for III-V semiconductors, all sources of inversion symmetry breaking in perovskite semiconductors are typically referred to as Rashba effects. For MAPbI, much less is known about the spin splittings arising from inversion asymmetry. This is in part because the crystal structure itself is still under debate as the establishment of inversion asymmetry requires careful modeling (typically using density functional theory) of x-ray diffraction data. In addition, unlike GaAs, perovskite has three crystal phases (α, cubic for temperatures above 327 K; β, tetragonal for temperatures between 162 K and 327 K; and γ, orthorhomic for temperatures below 162 K). The symmetry is typically broken due to distortions in the lead-iodide octahedra in MAPI, and has been predicted to occur in several perovskite materials [102, 105–110]. This thesis work focuses on the tetragonal phase of MAPI.

It is instructive to describe the Rashba effect in the traditional geometry of a two-dimensional electron gas under the application of a bias. In this case, the motion of the electrons in the structure is confined to the x and y directions ($\mathbf{k}_{\|}$ = k$_x\hat{x}$ + k$_y\hat{y}$), and an electric field is applied along the z-direction. If we consider the form of the spin-orbit interaction in Eqn. 2.2, ($\frac{\hbar}{4m^2c^2}\nabla V \times \mathbf{p}$) acts as an effective magnetic field that defines the equilibrium direction of the electron spin. In the case considered here, ∇V is along z and $\mathbf{p}$ is in the x-y plane, so the effective magnetic field is in the x-y plane with a direction that is perpendicular to $\mathbf{k}_{\|}$. For a given magnitude of the in-plane wavevector defining a circle in k-space, the equilibrium spin direction has the structure of a pinwheel, as shown in figure 2.3. The Rashba Hamiltonian is:

$$H_{\mathbf{R}\pm}(\mathbf{k}_{\|}) = \lambda_{\mathrm{R}}(k_x\sigma_y - k_y\sigma_x) \tag{2.3}$$

The associated dispersion relation is

$$E_{\mathrm{R}}(\mathbf{k}_{\|}) = \frac{\hbar k_{\|}}{2m} \pm \sqrt{\lambda_{\mathrm{R}}^2(k_x^2 + k_y^2)} \tag{2.4}$$

and is depicted in figure 2.3.

2.1.1 Optical Absorption

Light with a photon energy above the band gap of the semiconductor may be absorbed, causing the promotion of an electron from the valence band to the conduction band. This leaves behind a hole in the valence band. In this absorption process, energy and momentum must be conserved for the electron and the photon. The photon has negligible momentum relative to the electrons because the wavelength of light is ∼1 micron, while the lattice constant of the semiconductor is on the order of a few Angstroms. In this case, the photon causes a vertical transition in k-space, and we can write:

$$\hbar\omega = E_{\mathrm{c},\mathbf{k}} - E_{\mathrm{v},\mathbf{k}} \tag{2.5}$$

where $\hbar\omega$ is the energy of the photon, and the right side of the above contains the dispersion relations in Eqn. 2.1. This leads to the following relationship between the wavevector of the excited electron and the photon energy as:

$$k^2 = \frac{2m_r}{\hbar^2}(\hbar\omega - E_g) \tag{2.6}$$

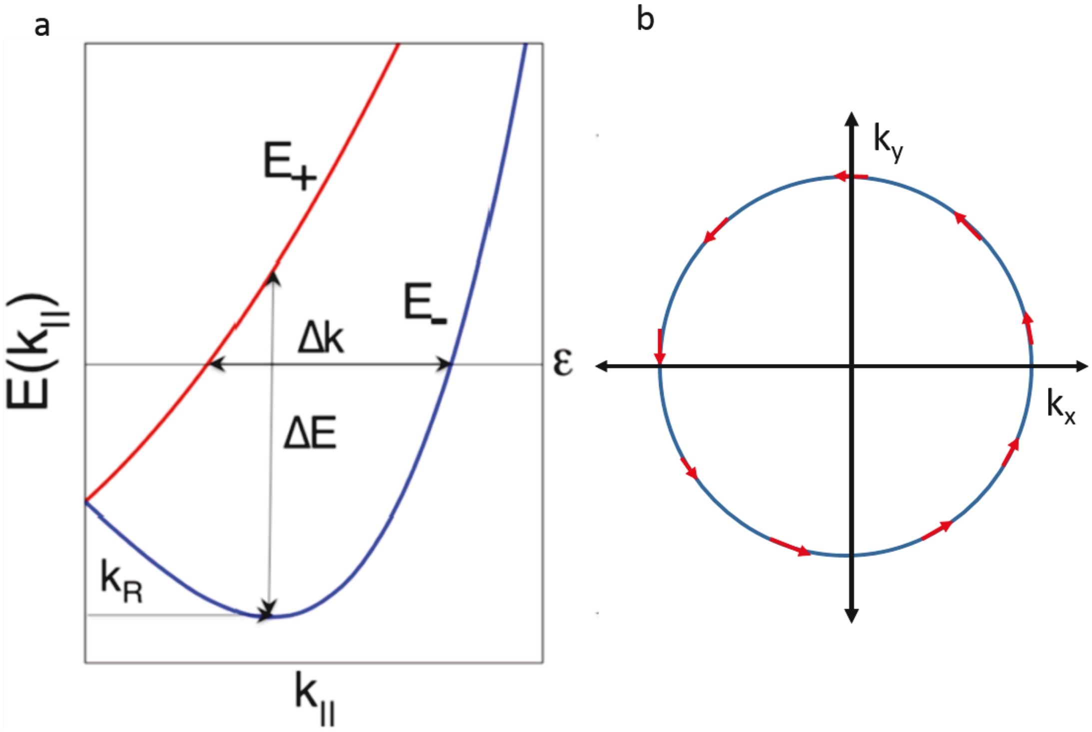

Figure 2.3: (a) Band structure near k=0 in a 2D system incorporating Rashba splitting (reproduced with permission [106]. (b) k$_x$ and k$_y$ at constant energy with red arrows illustrating the equilibrium carrier spin orientation.

In here, m_r is the reduced mass of the electron-hole pair ($\frac{1}{m_r} = \frac{1}{m_e^*} + \frac{1}{m_h^*}$). In this case, the optical joint density of states is given by:

$$\rho(\omega) = \Theta(\hbar\omega - E_g)\frac{(2m)^{3/2}}{\pi\hbar^2}(\hbar\omega - E_g)^{1/2} \tag{2.7}$$

where $\Theta(\hbar\omega - E_g)$ is the Heavyside step function. The optical joint density of states depends on the square-root of the photon energy, reflecting the square root density of states in each of the valence and conduction bands. The absorption coefficient (α) of a material describes the amount of absorbed light per unit length as the light propagates. We can use the optical joint density of states to obtain the linear absorption spectrum as:

$$\alpha(\omega) \propto \Theta(\hbar\omega - E_g)\frac{(\hbar\omega - E_g)^{1/2}}{(\hbar\omega)^2} \tag{2.8}$$

which also varies like the square root of the photon energy above the band gap. Each optical transition at a given wavevector represents an effective two-level system. When light excites this transition, it induces a dipole that oscillates with a natural resonance frequency equal to $\frac{1}{\hbar}(E_{\mathrm{c},\mathbf{k}} - E_{\mathrm{v},\mathbf{k}})$. The size of the absorption coefficient for a given semiconductor (the overall factor in Equ. 2.8) is determined in part by the dipole moment of the optical transition.

The above development describes direct optical absorption. It is also possible for a phonon to participate in the absorption process. In such a case, the energy and momentum of the phonon would need to be included. Phonon-assisted absorption is important near the band edge in an indirect gap semiconductor, for which the minimum in the conduction band is at a different wavevector than the maximum of the valence band, preventing direct transitions. Phonon assisted absorption is much weaker than direct absorption because it is a higher order process involving three particles (the phonon, electron and photon).

The simple square root prediction for the absorption coefficient for absorption above the band gap in Eqn. 2.8 is only an approximation to the absorption in a real semiconductor because it does not take into account the attractive Coulomb interaction between the electron and hole. As a result of this interaction, the electron and hole can form a bound state known as an exciton. An exciton is similar to a hydrogen atom, forming a series of bound states with energies below the band gap of the semiconductor. From the analysis of the hydrogen atom, the binding energy is given by,

$$E_B = \frac{m^* e^4}{2\hbar^2 \epsilon^2} \tag{2.9}$$

The strength of the exciton binding energy is determined by the size of the dielectric constant, ϵ.

The existence of these additional bound electron-hole pair states introduces additional absorption resonances below the band gap. The attractive Coulomb interaction also enhances the dipole moment of all of the optical transitions above the band gap (which are electron-hole pair states corresponding to unbound states of the exciton). The enhancement of the dipole moment, which is referred to as *Sommerfeld Enhancement* [111], is strongest for transitions at the band edge and decreases as the energy of the electron hole pair gets farther above the band gap. A schematic representation of the absorption spectrum with and without excitonic effects included is shown in figure 2.4.

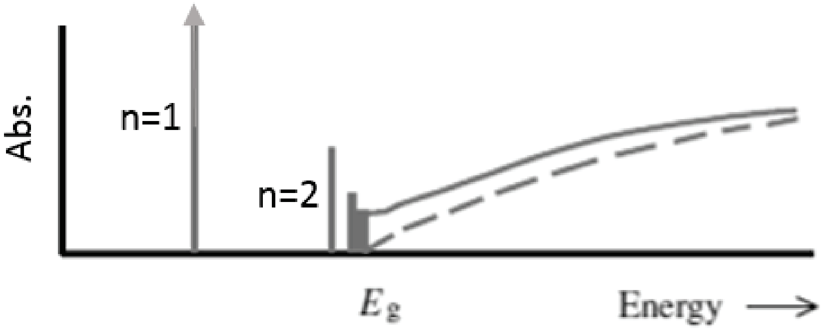

Figure 2.4: Qualitative representation of the absorption spectrum in the vicinity of the band gap of a direct-gap semiconductor with (solid line) and without (dashed lines) exciton effects. n represents the progression of bound states (reproduced with permission [101]).

The transitions shown in figure 2.4 neglect the influence of broadening, which leads to a finite width for all of the transitions, including the exciton and interband transitions. Since the area under each absorption line is constant (dictated by the dipole moment), for a sufficiently high level of broadening, the exciton peak will not be perceptible on the absorption spectrum. In addition, in a semiconductor with a relatively small dielectric constant, excitonic effects are strong. This has a strong impact on the shape of the absorption edge for the interband transitions above the gap. With a combination of strong excitonic effects and strong broadening, the lowest energy transitions above the band gap appears as a broad peak. This limit describes well the situation in MAPI at room temperature, and one must be careful to not mistake the Sommerfeld-enhanced band edge with the exciton peak. This issue is illustrated clearly in figure 2.5, which shows the calculated absorption spectrum in MAPI including broadening with two different sizes of the dielectric constant (*i.e.* two different strengths of excitonic effects).

The excitonic resonances above are "“free"” excitons in that they are free to move about the crystal. It is also possible for excitons to become bound to charged defects in the crystal. Charged defects can arise, for example, from the presence of vacancies (i.e. missing atoms), or interstitials (which are additional atoms that occupy a

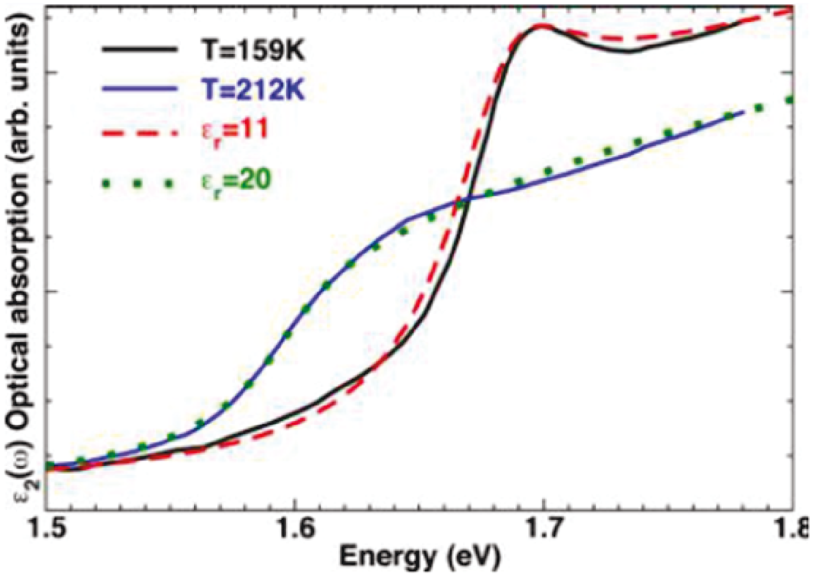

Figure 2.5: Absorption spectrum of MAPI (reproduced with permission [22]), illustrating the role of inhomogeneous broadening.

location that does not have an atom in it in the perfect crystal). These defects can involve atom types that are constituents of the perfect crystal (intrinsic) or other atoms (extrinsic). When an exciton is bound to a defect, its transition energy will be lower than that of a free exciton. This will introduce additional resonances below the hydrogenic series depicted in figure 2.4 for the free exciton. The dipole moment of the bound excitons will be determined by the density of defects in the crystal. Such bound exciton transitions are not typically observed in linear absorption spectra because they are much weaker than the free exciton transition. They are often observed in photoluminescence spectra, however, because electrons and holes relax to the lowest available states prior to recombining.

2.1.2 Carrier Scattering

After optical excitation, and before any scattering events occur, the electron-hole pairs have a well defined phase relationship with the laser excitation pulse. The excited carriers undergo a variety of scattering processes that lead to dephasing. These include scattering of electron-hole pairs with other electron-hole pairs (carrier-carrier scattering, mediated by the Coulomb interaction), scattering of carriers by phonons (thermal excitations of the crystal lattice), and scattering of carriers by defects in the crystal. The role of carrier-carrier scattering in the dephasing of electron-hole pairs may be studied using four-wave mixing experiments by measuring the dephasing time of the electron-hole pair transitions as a function of the power of the exciting laser beam. Since the power in the beam determines the density of electron-hole pairs excited by each laser pulse. The influence of many-body processes on the four-wave mixing signal are discussed in further detail in Section 1.2.3. The process of carrier scattering with phonons and defects are discussed in the subsections below.

Electron-Phonon Scattering

At finite temperature crystal lattice vibrations known as phonons are present. Electrons and holes can interact with phonons, causing scattering events that move the carrier from one point in k-space to another. Phonons are the fundamental quanta of energy associated with macroscopic oscillations of the crystal lattice that correspond to propagating waves. The oscillations can be perpendicular to the propagation direction, corresponding to shear waves known as transverse phonons, and can be parallel to the propagation direction, corresponding to compression waves known as longitudinal phonons. For a crystal structure with at least two atoms per primitive basis, there are two types of each of these classes of phonons: acoustic phonons and optical phonons. Acoustic phonons correspond to the motion of the unit cells relative to one another, and optical phonons correspond to the relative motion of the atoms inside each unit cell. Acoustic phonons have energies that increase linearly with wavevector for small wavevectors from zero, whereas optical phonons have an energy that is approximately independent of wavevector. The dispersion relation for GaAs is shown in figure 2.6, showing the two acoustic and two optical branches.

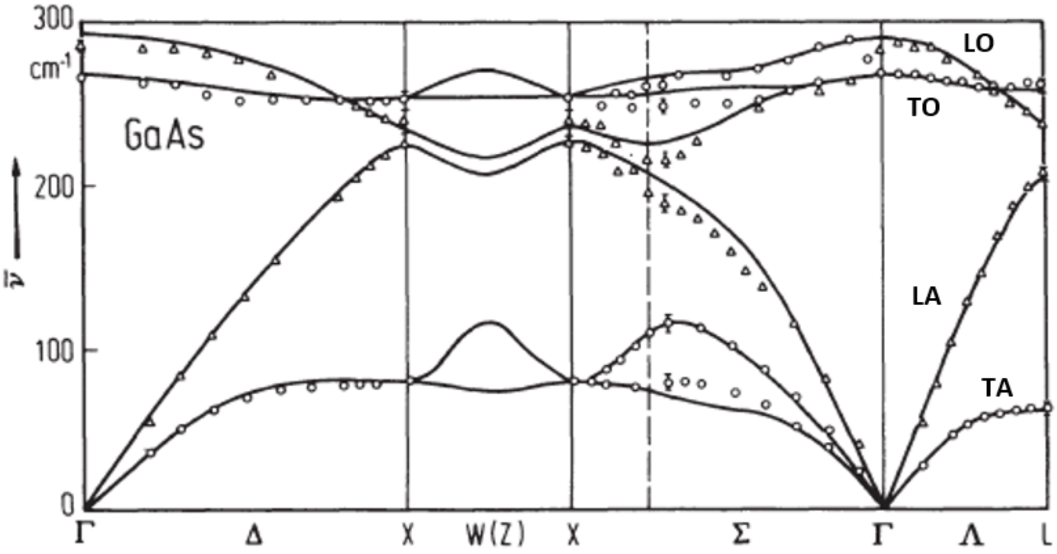

Figure 2.6: GaAs phonon dispersion showing the two acoustic and two optical branches (reproduced with permission [100]).

The dominant coupling between electrons and acoustic phonons is governed by the deformation potential coupling involving longitudinal acoustic phonons. This type of coupling takes into account the fact that the electron energy is modified by the volume deformation of the crystal. The interaction strength for electron-LA phonon coupling is:

$$V_q = iE_1\left(\frac{\hbar}{2\omega_q}\right)^{1/2} q \equiv iE_1\left(\frac{\hbar v_s}{2c_L}\right)^{1/2}\sqrt{q} \tag{2.10}$$

where E_1 is the deformation potential of the conduction band, ρ is the material density, $\omega_q = v_s q$ is the acoustic phonon dispersion with v_s the velocity of sound in the material, and $c_L = \rho v_s^2$ is the longitudinal elastic constant. We notice that the strength of the interaction varies like the square root of the wavevector: thus the longer the wave vector the stronger the interaction. In the limit of zero wave vector, there would be no coupling at all since this corresponds to a phonon with infinite wavelength. Since acoustic phonons describe the motion of unit cells relative to each other, an infinite wavelength phonon would simply correspond to the displacement of the crystal as a whole, which does not change the energy of the electron.

Perovskite and GaAs are both polar crystals because they involve ionic bonds. As explained above, optical phonons describe the motion of these charged ions relative to each other. An optical phonon in a polar crystal therefore has an electric field associated with it. This electric field couples strongly to the electron and dominates over the deformation potential coupling mechanism in polar crystals. The case of a crystal with just two atoms per primitive basis, which possesses one optical phonon mode, was analyzed by Fröhlich, and the associated interaction is called the Fröhlich interaction [101]. In this case, the coupling between electrons and polar optical phonons can be expressed as

$$V_k = -i\left(\frac{4\pi\alpha_e}{\Omega}\right)^{1/2}\frac{\hbar\omega_l}{q}\left(\frac{\hbar}{2m_e w_l}\right)^{1/4} \tag{2.11}$$

where α_e describes the strength of the polar coupling and $\hbar\omega_l$ is the longitudinal optical phonon energy which is approximately independent of q. The polar coupling strength is given by:

$$\alpha_e = (\frac{e^2}{\hbar})\sqrt{\frac{m}{2\hbar\omega_l}}\left(\frac{1}{\epsilon_\infty} - \frac{1}{\epsilon_0}\right) \tag{2.12}$$

where ϵ_∞ (ϵ_0) is the high (low) frequency dielectric constant. For polar coupling to LO phonons, the interaction strength varies inversely with the wave vector q of the phonon.

The probability of phonon absorption will be proportional to the occupation of the phonon mode at temperature T, which is given by the Bose-Einstein distribution:

$$n_{ph} = \frac{1}{\exp\frac{\hbar\omega}{k_B T} - 1} \tag{2.13}$$

where k_B is the Boltzmann constant. Phonon emission events do not depend on the occupation of the phonon mode, but conservation of energy dictates that the electron energy relative to the band edge must be at least as large as the phonon energy. For GaAs, the LO phonon energy is 35 meV [100]. In MAPI, there are several LO phonon modes to consider. The one with the strongest polar coupling constant is the Pb-I stretching mode, which has a phonon energy of 16 meV [112]. The lower optical phonon energy in MAPI compared to GaAs is due to the higher reduced mass of the anion and cation. Due to the phonon occupation factor, dephasing of electron-hole pairs due to scattering with phonons will be a function of temperature.

Ionized Impurity Scattering

Carriers in the crystal interact most strongly with charged impurities (as opposed to neutral impurities) due to the long range nature of the Coulomb interaction. A model of scattering with ionized impurities was developed by Conwell and Weisskopf that utilized the scattering cross section obtained from the Rutherford formula,

$$\sigma_\theta = \frac{1}{4}\left(\frac{Ze^2}{m_e v^2}\right)^2 csc^4\frac{\theta}{2} \tag{2.14}$$

where Z is the charge of the scattering centre, m_e is the electron effective mass, and v is the velocity. One can obtain the total cross section for scattering by integrating the above result over the scattering angle, and using the average density between two impurities to define a minimum scattering angle. We obtain

$$\sigma_c = 2\pi\int_{\theta_m}^{\pi}\sigma(\theta)sin\theta d\theta \quad = \pi\frac{1}{4}\left(\frac{Ze^2}{m_e v^2}\right)^2 csc^2\left(\frac{\theta_m}{2}-1\right) \tag{2.15}$$

where θ_m depends on the inter-impurity distance, $2r_m = N_I^{-1/3}$, and N_I is the impurity density. The rate of impurity scattering is given by:

$$\frac{1}{\tau} = N_I\sigma_c v \quad = \frac{\pi}{4}N_I^{\frac{1}{3}}v. \tag{2.16}$$

The rate of impurity scattering increases with the density of impurities. It also increases with the kinetic energy of the electron. In contrast to the rate of scattering with phonons, ionized impurity scattering is not dependent on the lattice temperature.

2.2 Theory and Analysis of Four-Wave Mixing Spectroscopy

This section will introduce the optical Bloch equations that have been used extensively to interpret the results of FWM experiments in semiconductors. The solutions to these equations for the geometry of a two-pulse degenerate four-wave mixing experiment will be presented in this section. We will first consider the case in which interactions between the charge carriers are neglected and present the solution for homogeneously and inhomogeneously broadened transitions, corresponding to excitons and interband transitions in the semiconductor [47]. This will be followed by an explanation of how interactions between charge carriers modifies this simple picture. These many-body interactions include a dependence of the transition energy and dephasing rate on the excited carrier density, referred to as excitation induced shift (EIS) and Excitation induced dephasing (EID), respectively. Finally, signals generated on the exciton transition due to exciton scattering with unbound electron-hole pairs, known as the continuum contribution to the exciton FWM signal (CC) will be described.

2.2.1 Independent (Non-Interacting) Two-Level System

We use a semi-classical model where a classical light field interacts with two-level atoms with ground state $|0\rangle$ and excited state $|1\rangle$

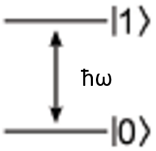

The Hamiltonian of the two-level system is given by,

$$H = H_0 + H_{int} + H_R \tag{2.17}$$

H_0 is the unperturbed Hamiltonian for the independent two-level system, H_{int} is the light-matter interaction Hamiltonian. In a semi-classical analysis, $H_{int} = \vec{\mu} \cdot \vec{E}$ where $\vec{\mu}$ is the electric dipole operator. The matrix elements of $\vec{\mu}$ determine the strength of interactions between the two-level system and the input electric field. Finally, H_R describes the processes that bring the system back to thermal equilibrium and is known as the relaxation Hamiltonian. The dynamic response of this two level system to the laser pulse may be obtained from the Liouville equation

$$\frac{\partial\rho}{\partial t} = \frac{1}{i\hbar}[H, \rho] \tag{2.18}$$

where H is the total Hamiltonian in Eqn. 2.17 and ρ is a density matrix,

$$\rho = \begin{bmatrix} \rho_{11} & \rho_{10} \\ \rho_{01} & \rho_{00} \end{bmatrix} \tag{2.19}$$

The diagonal elements represent the occupation probability of the excited and ground state, and the off-diagonal elements represent the coherence between the excited states. If a well-defined phase relationship exists between the independent two-level systems, the off-diagonal terms will be non-zero.

The four-wave mixing signal we wish to calculate results from the emission of light from a third-order nonlinear optical polarization excited on the ensemble of two level systems. We therefore need to apply the density matrix solution to the Liouville equation to calculate the polarization density P, which can be expressed as

$$P = NTr\{\mu\rho\} \tag{2.20}$$

where N is the number density of carriers in the ensemble, and Tr represents the trace of matrix $\mu\rho$. From this, a set of coupled differential equations can be derived known as the Optical Bloch Equations that describe the coherence and population dynamics of an ensemble of independent two-level systems. If we invoke the relaxation time approximation, then we have

$$\begin{aligned} [H_R, \rho]_{11} &= -i\hbar\frac{\rho_{11}}{T_1}, \\ [H_R, \rho]_{10} &= -i\hbar\frac{\rho_{10}}{T_2}. \end{aligned} \tag{2.21}$$

where $\mathbf{T}_1$ is the lifetime of the excited state, and $\mathbf{T}_2$ is the dephasing time. This leads to the optical Bloch equations, given by

$$\begin{aligned} \frac{\partial\rho_{01}}{\partial t} &= i\omega_{01}\rho_{01} - \frac{i}{\hbar}(H_{int})_{01}(2\rho_{11} - 1) - \frac{\rho_{01}}{T_2}, \\ \frac{\partial\rho_{11}}{\partial t} &= -\frac{i}{\hbar}[(H_{int})_{10}\rho_{01} - \rho_{10}(H_{int})_{01}] - \frac{\rho_{11}}{T_1}. \end{aligned} \tag{2.22}$$

This system of equations may be solved for the density matrix and used to evaluate the polarization. To isolate the component of the polarization that emits in the direction $2\mathbf{k_2} - \mathbf{k_1}$, the components of the density matrix are Fourier expanded in terms of the spatial variable in the horizontal direction defined by the intersection of the plane of incidence of the laser beams and the sample surface. The spectrally-resolved four-wave mixing signal is then obtained from this polarization solution by taking the Fourier transform with respect to time. One can carry out this solution analytically if the finite duration of the laser pulses is neglected and they are instead represented by Dirac delta functions. In this case, one obtains the spectrally-resolved FWM signal (SR-FWM) as

$$S_{SR}(\omega_t, \tau) = \Theta(\tau)e^{-\frac{2\tau}{T_2}} \frac{1}{\left(\frac{1}{T_2}\right)^2 + (\omega_0 - \omega_t)^2} \tag{2.23}$$

The SR-FWM signal for an ensemble of homogeneously broadened two-level independent systems is maximum at τ=0 and decreases exponentially with a rate of $2/T_2$. As well, the SR-FWM signal has a Lorentzian spectral profile. This type of signal is known as a free polarization decay FPD and is shown in figure 2.8.

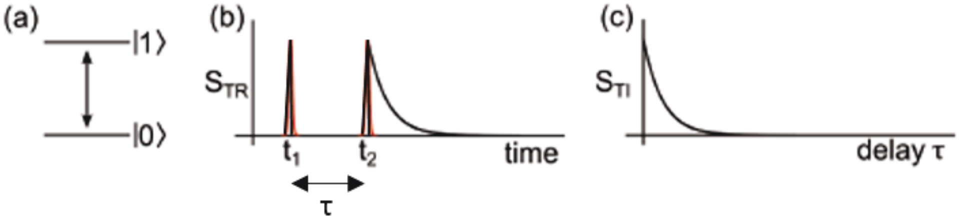

Figure 2.8: (a) Two-level homogeneously broadened system. (b) Pulse 1 arrives at time = t_1 and pulse 2 arrives some time τ later (t = t_2), and the resulting coherence decay (black) (c) TI-FWM signal (reproduced with permission [87]).

2.2.2 Inhomogeneously Broadened Transitions

To obtain the FWM signal from inhomogeneously broadened transitions that result from a continuum of closely spaced transitions (such as the inter-band electron-hole pair transitions) we solve the Optical Bloch Equation (OBE)s for a series of closely energetically spaced independent two-level transitions. In this case, the signal results from superimposing the polarization contributions for each transition:

$$S_{TR}(t) = \left| \sum_k P_k^{(3)}(t,\tau,T) \right|^2 \tag{2.24}$$

where $P_k^{(3)}$ is the macroscopic FWM polarization induced by each two-level system with wave vector k. The resulting FWM signal is given by:

$$S_{SR}(\tau) = e^{-\frac{4\tau}{T_2}} e^{-\frac{2T}{T_L}} \left(1 + erf\left(\frac{\delta\omega\tau}{\sqrt{\pi}}\right)\right) \tag{2.25}$$

where erf is an error function, and $\delta\omega$ is the inhomogeneous linewidth of the excited free carrier transitions.

The SR-FWM response from an inhomogeneously broadened transition is maximum at t=τ in contrast to the SR-FWM signal for a homogeneously broadened transition that peaks at τ=0. This response is known as a *photon echo*, and is analogous to the spin-echo in nuclear magnetic resonance. The photon echo is the result of a rephasing of the polarizations excited on each of the two level systems at different wave vectors k. The SR-FWM signal decays exponentially at twice the rate of a homogeneously broadened transitions. The signal peaks at positive delay dictated by the joint effects of T_2 and $\delta\omega$ shown in figure 2.9 and decays with a rate of 4/T_2.

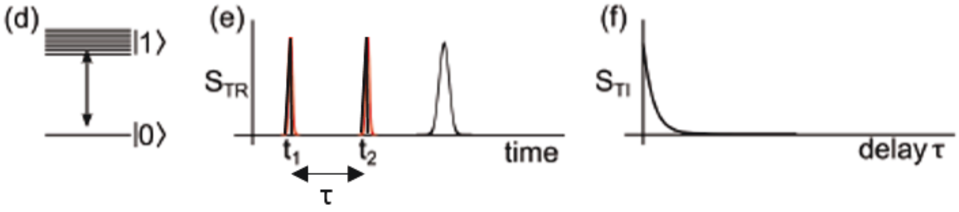

Figure 2.9: (a) homogeneously broadened transition (closely spaced continuum of transitions). (b) pulse 1 arrives at t = t_1 and pulse 2 arrives some time τ later (t = t_2), resulting in a photon echo (black line). (c) TI-FWM signal with T$_{2,inhomo}$ = 2T$_{2,homo}$ (reproduced with permission [87])

2.2.3 Many-Body Effects

The OBEs are unable to account for Coulomb mediated many-body carrier interactions but can be suitably modified to incorporate interaction induced effects by including carrier density dependent terms.

Excitation Induced Dephasing and Excitation Induced Shifts

EID results from carrier interactions leading to dephasing due to an increase in carrier density, and EIS results from a carrier density dependent modification to the transition energy due to dielectric screening [86]. These effects are included by replacing the constant dephasing rate and transition energy by

$$\begin{aligned} \frac{1}{T_2} &= \frac{1}{T_2^0} + \gamma_{EID} N, \\ \omega &= \omega_0 + \gamma_{EIS} N. \end{aligned} \tag{2.26}$$

where T_2^0 and ω_0 are the dephasing time and resonance frequency in the absence of an excited population and N is the carrier density. The coefficients γ_{EID} and γ_{EIS} reflect the strength of coupling between the charge carriers. As a result of excitation-induced dephasing, the measured T_2 time in the semiconductor depends on the excited carrier density. Measurements of T_2 versus the excitation laser power then give a means to determine the rate of carrier-carrier scattering in the sample under study.

Continuum Contributions (CC) to the Exciton Signal

When EID and EIS are propagated through the OBEs, additional sources of polarization components emitting along $2\mathbf{k_2} - \mathbf{k_1}$ emerge. Whereas the free polarization decay signal can be thought of as resulting from the diffraction of a portion of the second laser pulse from the population density grating, these additional signals are referred to as *polarization diffraction* signals because they result from the diffraction of the polarization density excited by the second pulse rather than the pulse itself. These additional signals are proportional to the coefficients γ_{EID} and γ_{EIS}. These additional many-body related signals are small for inhomogeneously broadened transitions due to destructive interference among the signals originating from different k's. For a homogeneously broadened transition, however, these many body signals do not cancel out and can be extremely large due to the strong Coulomb interaction in the semiconductor. Furthermore, these signals are strongly enhanced when broadband optical pulses are used because all of the excited carriers (both excitons and free carriers) contribute to modifying the dephasing rate and transition energy. Under these conditions, the FWM signal is known as the continuum contribution to the exciton signal (CC). The CC response has been observed in both GaAs [64, 65, 69, 70] and Ge [76, 77, 113].

Allan *et al.* developed an analytic model for the CC signal. It may be obtained by modifying the OBEs to include coupling terms between the exciton and continuum transitions for the case when the majority of carriers excited are free-carriers (N_k), and only the low-energy tail of the broadband laser pulse spectrum excites exciton polarizations N_{ex} so that $N_{ex} \ll N_k$ [71]. This leads to the result

$$p_{ex}^{(3)}(t) \propto \frac{\mu_{ex}}{\hbar} N^{(2)}(t) e^{-\left(\frac{1}{T_{2,x}^{0}} + i(\omega_0 + \gamma_{EID} N^{(0)})t\right)} \Theta(t) \tag{2.27}$$

The continuum contribution (CC) to the exciton signal has a linewidth determined by the dephasing rate of the exciton transition and only contributes for $\tau = 0$. The CC is therefore a zero-delay feature only. An example of such a CC signal from the exciton in the semiconductor Germanium is shown in figure 2.10. Notice how much larger the exciton signal is relative to the signal from the interband transitions in comparison to the linear absorption spectrum in figure 2.10.

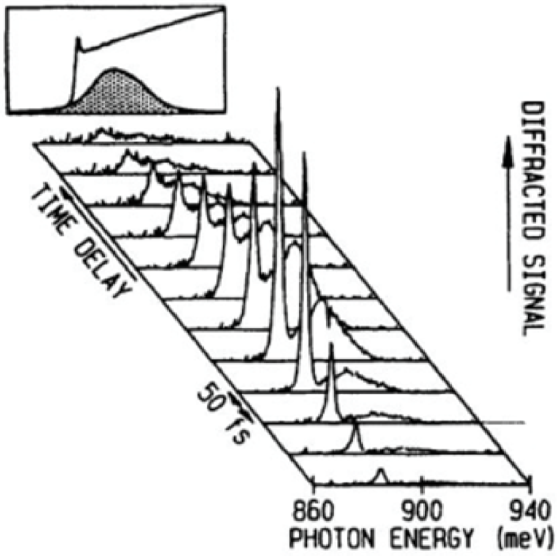

Figure 2.10: Results from SR-FWM experiments on bulk Ge and linear absorption shown in the background. (reproduced with permission [77])

Summary

In a conventional semiconductor like GaAs, the FWM signal is composed of several distinct signal contributions including 1) FPD of the homogeneously broadened exciton transition that is maximum at $\tau = 0$ and decays with a dephasing time of $\frac{2}{T_2}$. FPD has a discrete spectral profile with a linewidth inversely proportional to the dephasing time of the transition; 2) a *photon echo* from inhomogeneously broadened free-carrier excitations that reaches a maximum value at positive delay dictated by the spectral width of the laser and the linewidth of the transition, and decays with a dephasing time of $\frac{4}{T_2}$, and 3) the CC, which strongly enhances the exciton FWM signal due to simultaneous free carrier and exciton excitation resulting from many-body coupling. The CC to the exciton is apparent near $\tau = 0$ when the excitation pulses are overlapped.

Chapter 3

Experimental Methods

This chapter presents the experimental techniques used in this thesis work to study the coherent photo-physics of excitons, many-body carrier interactions, and carrier-phonon scattering in MAPI perovskite thin-films. Section 3.1 begins with a description of MAPI thin-film preparation, and GaAs film preparation, including sample characterization using x-ray diffraction (XRD), linear absorption spectroscopy, and scanning electron microscopy (SEM). Section 3.2 describes FWM coherent spectroscopy. Section 3.3 describes the techniques used to compress ultrafast optical pulses using group velocity dispersion (GVD) compensation, and ultrafast pulse characterization including the laser spot-size measurement, a description of zero-background second harmonic intensity autocorrelation that measures the temporal pulse width, and carrier density calculations. The thin-films of MAPI studied in this thesis work were prepared and characterized using XRD by Charlotte Clegg at Dalhousie under the supervision of Prof. Ian Hill. The GaAs films were grown by Dr. Xinyu Liu and Dr. Margaret Dobrowolska under the supervision of Prof. Jacek Furdyna. All of the four-wave mixing experiments, linear absorption and SEM sample characterization were carried out by myself at Dalhousie.

3.1 Sample Preparation and Characterization

3.1.1 MAPI Perovskite Thin-Film

The perovskite absorber layer can be deposited using a variety of methods, temperatures, precursor concentrations, solvents, preparation conditions (deposited in air, or inert atmosphere) and using a variety of additives, and depends on the morphology of the surface it is deposited onto (glass or compact/mesoporous TiO2 etc.). The highest efficiency perovskite solar cells have been achieved using a single step anti-solvent deposition technique, using a device architecture of glass/FTO/compact-TiO2/mesoporous-TiO2/Perovskite/Spiro-OMETAD/Au , where the first anti-solvent depositions used MAPI perovskite [114]. The open-circuit voltage was increased using mixtures of Formamadinium, Rubidium or Cesium, Methylammonium, Lead, Bromide and Iodide [115, 116]. To quantify the perovskite absorber layer quality the crystalline structure is analyzed using XRD to determine if unwanted crystal geometries are present in the film, including the presence of residual Lead Iodide [117]. High quality perovskite films for solar cells must be pinhole-free. The film homogeneity is verified using SEM. Finally, the linear absorption spectra is measured and compared to well documented, high quality perovskite films [23].

The MAPI samples were synthesized using a modified two-step procedure reported elsewhere [118]. The two steps include the deposition of a Lead Iodide film from solution, and the subsequent infiltration of a Methyl ammonium iodide solution into the existing Lead Iodide film. After annealing, the film crystallizes into perovskite. First, a solution of 1M lead iodide (PbI2) in dimethylformamide (DMF) was stirred at 70°C for 12 hours, and then filtered using a 0.45 micron polytetrafluoroethylene (PTFE) filter. Prior to depositing, the sapphire substrate (UQG Optics) was cleaned using detergent, and sonicated in deionized water, acetone, and finally ethanol. The substrate was then irradiated with ultraviolet (UV) ozone for 10 minutes. 300 μl of the PbI2 solution was cast onto the sapphire substrate and spun at 5000 RPM for 60 seconds. The film was then dried on a hotplate at 70°C for 15 minutes to remove any residual solvent. 300 μl of CH_3NH_3 (60 mg/ml) solution in DMF was then cast onto the static substrate and spun at 4000 RPM for 60 seconds. The films were then annealed at 100°C for 2 hours and subsequently stored in an inert atmosphere glove box. For optical experiments, the samples were mounted in an optical cryostat in the glove box. The cryostat was transferred to the optical setup and evacuated for low temperature measurements. The same cryostat was used for linear absorption measurements (CARY UV-VIS absorption spectrometer) and FWM experiments (described in Section 3.2). After measurements were completed the samples were again stored in the glove box to avoid sample exposure to air.

A companion sample was prepared using the same recipe and was characterized

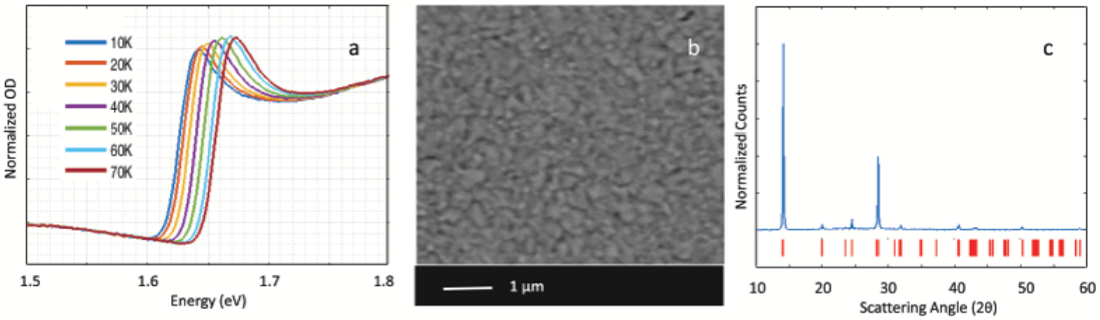

Figure 3.1: Characterization of the MAPI perovskite thin film, showing (a) temperature depedent linear absoprtion (b) scanning electron microscopy, and (c) x-ray diffraction (XRD). b and c were taken at room temperature. The red lines in c indicate the calculated peak positions for the tetragonal phase (reproduced with permission [48]).

using SEM and XRD. The SEM images indicate good sample uniformity, and crystal grains on the order of a few hundred nanometers. The XRD results indicated a full conversion to perovskite. The linear absorption as a function of temperature shows the band gap at 1.642 eV for 10 K, increasing to 1.673 eV for 70 K using the methods described in Even et. al. [22].

3.1.2 GaAs Single Crystal

The GaAs sample was prepared in Professor Jacek Furdyna's group at the University of Notre Dame. Two samples were utilized in these experiments: High temperature GaAs (Ht-GaAs) is so named due to the high temperature of the substrate during sample growth (600°C) resulting in low defect densities ($10^{13} cm^{-3}$). For Low temperature GaAs, in contrast, the substrate is held at 250°C during growth resulting in a high density of mid-gap trap states ($10^{18} cm^{-3}$). The preparation procedures for both samples is otherwise identical. 100 nm of a GaAs 'buffer layer' is deposited using MBE on a GaAs substrate. This is followed by the deposition of 175 nm of $Al_{0.27}Ga_{0.73}As$ that is used as a "stop etch" layer, and finally, 800 nm of GaAs (eventually becoming the studied film) was deposited onto the stop etch layer. The samples were then glued face down to a sapphire substrate for FWM measurements. The sample was then etched using mechanical, and chemical wet etching to expose the GaAs sample under study. The samples were characterized using linear absorption using a continuous wave white light source. The linear absorption spectra for the Ht-GaAs sample shows a sharp absorption band edge onset, with the direct band gap apparent at 1.5068 eV, and a sharp excitonic peak. The linear absorption spectra for the Lt-GaAs sample illustrates the mid-gap defect induced smearing of the band edge reported elsewhere [70] for the Lt-GaAs sample resulting from the large concentration of mid-gap defect states [119]. The absorption coefficient of both samples was extracted taking into account multiple reflections at the sample surface.

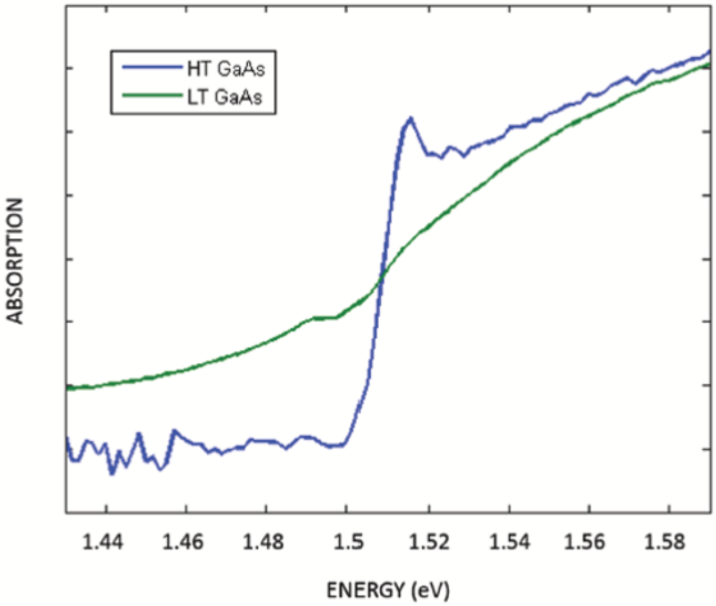

Figure 3.2: Linear absorption for Lt-GaAs, and Ht-GaAs (reproduced with permission [49])

3.2 Four-Wave Mixing Spectroscopy

The setup utilized in these measurements is spectrally resolved two-pulse degenerate four-wave mixing SR-FWM. In this setup two identical pulses with electric fields $\mathbf{E}_1$ and $\mathbf{E}_2$, and wave vectors $\mathbf{k}_1$ and $\mathbf{k}_2$ impinge onto the sample with a variable delay between the two pulses, as shown in figure 5.7. The pulses interfere at the sample, generating a position dependent density of carriers. As electron-hole pairs modify the local refractive index and absorption coefficient, a carrier density optical grating is generated. This carrier grating is only generated when the electron-hole pairs are still in phase after photoexcitation and have not scattered with each other or with the lattice. The second pulse that generated the carrier density optical grating 'self-diffracts' off of that same grating. We monitor the resultant signal at $2\mathbf{k}_2$-$\mathbf{k}_1$.

A Titanium sapphire oscillator outputs optical pulses with a duration of 60 femtoseconds. Dispersion in the optical elements in the setup GVD on the way to the sample, causes these initially transform-limited pulses to broaden. This GVD is compensated for using a prism compressor. The operation of the prism compressor which leads to a pulse duration at the sample of 50 fs, is described in Section 3.3.1. After the compressor the pulses are focused through a pinhole that acts as a spatial filter, where the aperature area of the pinhole has been chosen to select the fundamental Gaussian mode (TEM_{00}) of the laser. The pulses are then split using a beam splitter resulting in the two pulses with electric fields $\mathbf{E}_1$ and $\mathbf{E}_2$ and similar intensities. One pulse goes directly to the sample. The other is sent through a delay line, and then meets the first pulse at the sample. In this way, we can delay one pulse with respect to the other pulse. The path length of pulse $\mathbf{E}_2$ is adjusted continuously as it reflects off a retroreflector mounted to a speaker cone that oscillates with a frequency of 12 Hz. This system configuration is known as the fast scan technique, and results in the final temporal signal being averaged over many optical pulses, substantially increasing the signal-to-noise ratio. Both pulses are then focused onto the sample, and spatially overlapped using the same lens, resulting in a spot-size of 80 μm. The spot size measurement is described in Section 3.3.3. The FWM signal is monitored using a monochromator that allows us to probe the signal at different energies, and a Photomultiplier tube that amplifies the signal. The samples are mounted in an optical cryostat that enables optical throughput of the laser pulses, and temperature control in the range 10-300°K.

A Helium Neon laser (wavelength of 632.8 nm) following the same beam path as $2\mathbf{k}_2$-$\mathbf{k}_1$ illustrated in figure 5.7 is utilized to calibrate the monochromator grating angle versus wavelength.

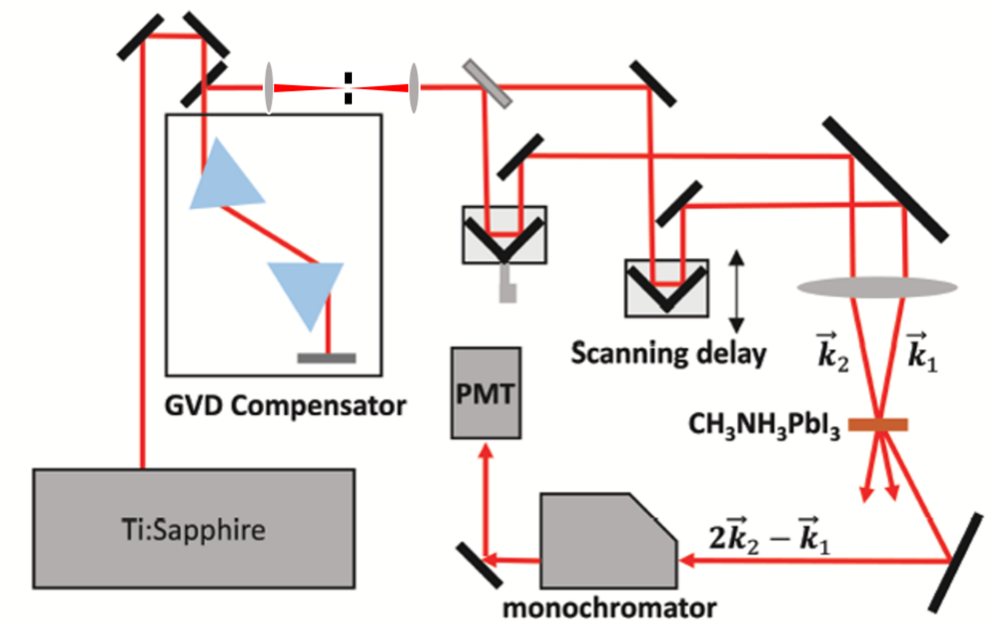

Figure 3.3: A schematic of the FWM apparatus. 40-50 fs pulses are generated in the Ti:Sapph oscillator. To compensate for positive GVD in the optical e;ements in the setup (lenses, filters) negative GVD is introduced using a pulse compressor before the setup. The pulses are then split. One is sent to the sample with wavevector $\mathbf{k}_1$, and the other through a delay line, and then to the sample with wavevector $\mathbf{k}_2$. The signal is collected in the FWM direction of $2\mathbf{k}_2$-$\mathbf{k}_1$, and sent through a monochromator to monitor the energy dependence of the signal, and then to a photomultiplier tube to amplify the signal (reproduced with permission [48]).

3.2.1 Carrier Dephasing Times

Yajima and Tiara successfully modelled the FWM response of both homogeneously, and inhomogenously broadened transitions [62]. We probed the response of electron-hole pairs above the bandgap. This continuum of transitions is intrinsically inhomogeneously broadened. The FWM signal (from Yajima and Tiara) for an inhomogeneously broadened transition is given by,

$$J = Ae^{-\frac{4}{T_2}\tau_d}\left(1 + \Phi\left(\frac{\delta\omega}{\sqrt{\pi}}\tau_d\right)\right) \tag{3.1}$$

where $\mathbf{T}_2$ is the dephasing time, τ_d is the delay between pulses 1 and 2 in the FWM experiment, δ is the degree of inhomogeneous broadening, and:

$$\Phi(x) = \frac{2}{\sqrt{\pi}} \int_0^x e^{-t^2} dt \tag{3.2}$$

This result was convoluted with the optical pulses used in the experiment, modeled as a Gaussian pulse with a pulse width that was measured using the results from section 3.3 and δ was extracted from the FWM data at zero delay, leaving $\mathbf{T}_2$ as the only fit parameter. Figure 3.4 shows an example FWM signal and excitation pulse, with the associated fit and extracted dephasing time $\mathbf{T}_2$.

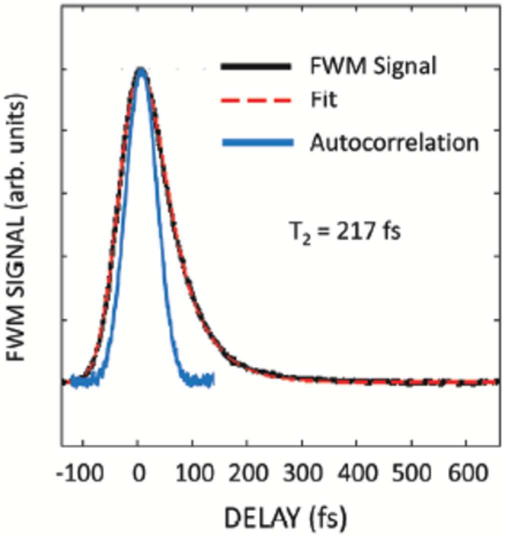

Figure 3.4: The black trace illustrates the experimental intensity versus time of the FWM signal 11 meV above gap. The dotted red line is the fit of a photon echo response [62] convolved with a Gaussian pulse with the physical parameters of the optical pulses utilized in our experiments seen in blue (reproduced with permission [49]).

3.3 Pulse Characterization

The pulse characteristics including the temporal duration and spectrum, dictate the temporal resolution of the experiment and the spectral range of transitions excited, respectively. The spot size must be determined in order to calculate the excited carrier density. The temporal intensity profile is measured using the zero-background second harmonic autocorrelation technique as described in section 3.3.1, and a spectrometer was utilized to measure the pulse intensity spectrum described in section 3.3.2. The spot size (beam waist) intensity profile, is measured using a beam profiler as described in section 3.3.3, and finally the excited carrier density calculation is described in section 3.3.4.

3.3.1 Ultrafast Pulse Width Compression and Measurement

The pulse width was compressed using a GVD prism set and measured using a zero-background autocorrelation apparatus.

GVD Compensation

The pulse temporal duration (pulse width) dictates the temporal resolution of the FWM experiment. GVD occurs when a pulse propagates through a material with dispersion, *i.e.* with a frequency-dependent index of refraction. GVD is positive in most materials (longer wavelength photons travel faster than shorter wavelength photons). Broadband pulses have a spread of wavelengths, and therefore longer wavelengths travel faster through the material compared to shorter wavelengths, resulting in a temporal spreading of the pulse. As the pulse travels through the optical setup, positive GVD is accumulated. Negative GVD is introduced to compensate for these effects by implementing a prism compressor. A prism compressor generates a negative GVD by ensuring that longer wavelength components of the pulse traverse a longer path length through the prism material, incurring a phase shift with respect to the shorter wavelength components. A schematic diagram of the pulse compressor layout is shown in figure 3.5.

Utilizing the autocorrelation technique as described below, the minimum GVD, or minimum phase difference between the spectral components in the pulse, is verified by minimizing the temporal pulse width. The autocorrelation is measured at the sample position after the pulse has propagated through the dispersive optical components. The GVD apparatus therefore compensates for all of the down-stream dispersion, resulting in a near Fourier transform limited pulse at the sample position (40 fs).

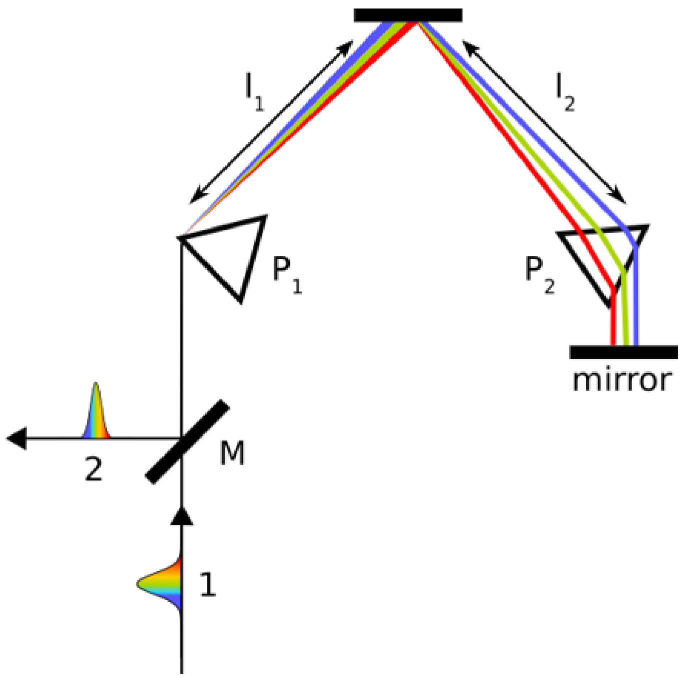

Figure 3.5: Schematic of GVD apparatus. Pulse 1 enters with positive GVD after propagating through several optical elements resulting in the longer wavelengths (red) leading the shorter wavelengths (blue). After GVD compensation, the pulse emerges with a shorter temporal pulse-width, as different wavelength components are overlapped in time.

Zero-background Autocorrelation

Zero-background autocorrelation is used to measure the temporal duration of the ultrafast optical pulses. In this method, the pulses used in the FWM experiment are split using a beam splitter, and the two resulting pulses are focused onto a β barium borate (BBO) nonlinear crystal phase-matched for optimal second harmonic generation at 800 nm. The signal measured on a silicon photodiode originates from the second harmonic generation due to contributions from pulse 1 and pulse 2. In second-harmonic generation (SHG), a photon from pulse 1 with momentum $\mathbf{k_1}$, and energy $E_1 = \hbar\omega_1$, and a photon from pulse 2 with momentum $\mathbf{k_2}$ and energy $E_2 = \hbar\omega_2$ are annihilated, and generate a third photon with momentum $\mathbf{k_1}+\mathbf{k_2}$, and energy $\hbar\omega = \hbar\omega_1 + \hbar\omega_2$. The signal is measured as a function of the delay between pulse 1 and pulse 2, resulting in a convolution of the intensity of pulse 1 and pulse

2.

$$I_{AC}(\tau) \propto \int_{-\infty}^{\infty} dt\, I(t)I(t-\tau) \tag{3.3}$$

The FWHM of the signal as a function of delay is proportional to the FWHM of the original pulse, where the constant of proportionality depends on the pulse shape. For a Gaussian pulse that factor is 0.707 [120].

3.3.2 Pulse Spectrum Measurement

In a FWM experiment the spectrum of the pulse, or the intensity as a function of wavelength, dictates the energetic transitions that are excited within the sample. The pulse spectrum was measured for each FWM signal using a spectrometer (Oceanoptics USB4000). A fibre-optic cable couples the laser beam into the spectrometer.

3.3.3 Laser Spot Size Measurement

The carrier density depends on the area or "“spot size"” of the laser beam and is defined as the 1/e distance from the Gaussian spatial beam centre [120]. The spot size was determined using a beam profiler (Coherent Lasercam HR). The laser beam is sent through a neutral density filter to control the intensity and the beam is then focused onto the active area of the beam profiler where a 2D array of photodiodes measures the beam intensity as a function of x and y. The beam waist is minimized by moving the beam profiler along the axis of beam propagation using a micrometer. The spatial full-width at half maximum (FWHM) of the laser beam is then calculated using built-in analysis software.

3.3.4 Carrier Density Calculation

The excited carrier density is determined by calculating the number of absorbed photons per pulse assuming that each absorbed photon excites an electron-hole pair. The average power of the laser beam is measured before and after the sample. The difference in the measured average power is the average power absorbed by the sample after accounting for reflection losses at all interfaces including at cryostat windows and sample interfaces. The average power per pulse is calculated by dividing the average power by the repetition rate of the laser. The number of photons per pulse is then calculated from the ratio of energy per pulse, and energy per photon. The number of photons per pulse is then averaged over the volume of the beam as it propagates through the sample (the spot size multiplied by the sample thickness). This is a good approximation because the absorption depth near the band gap where the laser is tuned is larger than the sample thickness (265 nm)

Chapter 4

Simultaneous observation of free and defect-bound excitons in $CH_3NH_3PbI_3$ using four-wave mixing spectroscopy

Authors: Samuel A. March[1], Charlotte Clegg[1], Drew B. Riley[1], Daniel Webber[1], Ian G. Hill[1], Kimberley C. Hall[1]

[1]Department of Physics and Atmospheric Science, Dalhousie University, Halifax, Nova Scotia B3H4R2, Canada

Reprinted from Scientific Reports (**6**, 39139 (2016))(open source)

Kimberley C. Hall, and Murat Yildirim developed the four-wave mixing techniques. Samuel March performed the four-wave mixing experiments, the data analysis, linear absorption and SEM sample characterization. Daniel Webber designed and built part of the apparatus. The thin-films of MAPI were prepared and characterized using XRD by Charlotte Clegg at Dalhousie under the supervision of Prof. Ian Hill. Kimberley C. Hall and Samuel March conceived and designed the experiments. Samuel March and Kimberley C. Hall wrote the manuscript with input from all authors.

The exciton binding energy dictates the operative mechanism for charge transport. If the exciton binding energy is large ($>> k_BT$), photo-currents are dictated by the drift/diffusion of excitons. If the exciton binding energy is on the order of the thermal energy at room temperature, transport is dictated by the drift/diffusion of free carriers that transport more efficiently than excitons. The exciton binding energy has been a topic of debate for several years due in part to the difficulty directly measuring this material parameter using common spectroscopic techniques, arising from the static and dynamic disorder in this 'soft' material system. In this study, we directly measure the exciton binding energy in the low temperature (orthorhombic) phase using FWM spectroscopy that is highly sensitive to exciton signals. We found two distinct exciton transitions that we attribute to free excitons, and excitons bound to shallow trap states, both of which lie within the spread of reported exciton binding energies. The presence of two exciton transitions would lead to inconsistencies in determining this value, where different spectroscopic techniques predominantly probe the free or defect-bound exciton transitions.

4.1 Abstract

Solar cells incorporating organic-inorganic perovskite, which may be fabricated using low-cost solution-based processing, have witnessed a dramatic rise in efficiencies yet their fundamental photophysical properties are not well understood. The exciton binding energy, central to the charge collection process, has been the subject of considerable controversy due to subtleties in extracting it from conventional linear spectroscopy techniques due to strong broadening tied to disorder. Here we report the simultaneous observation of free and defect-bound excitons in $CH_3NH_3PbI_3$ films using four-wave mixing (FWM) spectroscopy. Due to the high sensitivity of FWM to excitons, tied to their longer coherence decay times than unbound electron-hole pairs, we show that the exciton resonance energies can be directly observed from the nonlinear optical spectra. Our results indicate low-temperature binding energies of 13 meV (29 meV) for the free (defect-bound) exciton, with the 16 meV localization energy for excitons attributed to binding to point defects. Our findings shed light on the wide range of binding energies (2-55 meV) reported in recent years.

4.2 Introduction

The efficiency of solar cells using organometal halide perovskite semiconductor absorber layers has skyrocketed during the past few years, now reaching a level competitive with existing solar cell technologies [5] while offering a low-cost solution-processed device platform. This has stimulated intense research into the fundamental photophysical properties of these materials [12, 13, 16–27, 29, 30, 32, 33, 121–

125]. A parameter that has received considerable attention recently is the exciton binding energy (E_b), which determines the primary mechanism of carrier transport during device operation. Unlike inorganic solar cell materials such as III-V semiconductors, in which sharp exciton resonances greatly simplify extraction of E_b, the solution-processed organometal halide perovskites possess substantial broadening due to defects [88] and intrinsic dynamic disorder associated with the freedom of orientation of methylammonium ions [89, 90]. The broadening associated with these effects, which has been found to vary from 30 meV at cryogenic temperatures to 60 meV at room temperature [24], is comparable to (or larger than) the exciton binding energy. This broadening complicates the extraction of E_b from absorption or ellipsometry techniques [25]. In addition, while photoluminescence provides an effective probe of defect-induced localization and recombination processes [16,17], these techniques cannot isolate transitions relevant to absorption within an operational solar cell and can be hampered by incomplete phase transitions [17, 24]. Extraction of E_b from magneto absorption techniques is also complicated by the strong broadening in the organometal halide perovskites, resulting in the need to use large magnetic fields ($\sim$20 Tesla) [18, 19]. Due to these challenges, even for the most widely studied material $CH_3NH_3PbI_3$, the value of E_b has been quite controversial, with reports ranging from 2 meV to 55 meV [13,18–27,32,33,121–123].

Here we apply femtosecond four-wave mixing spectroscopy (FWM) to probe excitonic resonances in $CH_3NH_3PbI_3$. In this technique, two coherent ultrafast laser pulses described by electric fields $\vec{E_1}$ and $\vec{E_2}$ with wave vectors $\vec{k_1}$ and $\vec{k_2}$ excite a polarization component that emits light with wavevector $2\vec{k_2}$-$\vec{k_1}$ (see Fig.

Our experiments reveal two discrete resonances below the band gap of the $CH_3NH_3PbI_3$ thin films, which we attribute to the free exciton transition and a defect-bound exciton transition. The simultaneous observation of both free and localized excitons using this absorption-based nonlinear optical technique shows that both types of exciton can contribute to absorption during operation of a solar cell. At 10 K, the excitonic resonances we observe occur at 1.629 eV and 1.613 eV. The 16 meV energy separation is attributed to the binding energy of excitons to point defects within the perovskite film [88], and is in reasonable agreement with the recent measurement of an exciton localization energy of 17 meV in $CH_3NH_3PbI_{3-x}Cl_x$

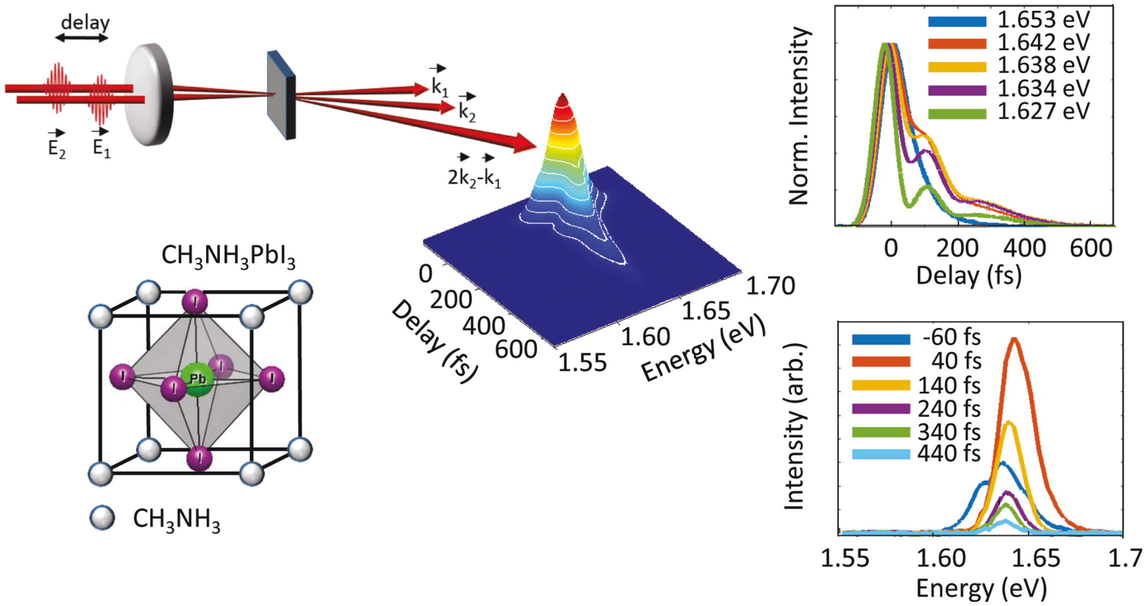

Figure 4.1: **Upper left**, schematic of four-wave mixing spectroscopy. Two 40 fs input pulses E_1 and E_2 excite a carrier density grating, and the self-diffracted signal along $2k_2 - k_1$ is measured using a monochromator and photomultiplier detector as a function of time delay. Lower left, methylammonium lead iodide perovskite ABX_3, with A = CH_3NH_3, B = Pb, X = I. **Center**, FWM response of $CH_3NH_3PbI_3$ sample at 10 K for excitation at 1.652 eV, 11 meV above the band gap. **Upper Right**, FWM signl at fixed values of detection photon energy, showing a smooth decay (oscillations) for energies above (below) band gap. **Lower Right**, FWM spectrum at fixed values of time delay, indicating multiple spectrally-distinct signal contributions

using photoluminescence and THz techniques [16]. Our measured transition energies correspond to an exciton binding energy of 13 meV (29 meV) for the free (defect-bound) exciton at 10 K, with a negligible temperature dependence up to 40 K. The low-temperature free exciton binding energy we measure is in reasonable agreement with the value of 16 meV determined at 2 K from recent magneto-optical studies at high magnetic fields [18, 19]. Together with the difficulty in fully characterizing the dielectric constant including the potential contributions of phonons [22, 26] and related dispersion [27], the close proximity of the free and bound exciton states we observe has likely contributed to the broad range of exciton binding energies reported in the literature [13, 18–27, 30, 32, 33, 121–123].

4.3 Results and Discussion

The four-wave mixing signal measured on the $CH_3NH_3PbI_3$ sample at 10 K is shown in Fig. 4.1. For these results, the center photon energy of the laser spectrum was 1.653 eV, 11 meV above the band gap determined from linear absorption measurements (Fig. 4.2). The FWM spectrum exhibits a strong dependence on the time delay between the exciting laser pulses, as shown in the lower right panel of Fig. 4.1. For time delays on the rising edge of the FWM signal, the spectrum consists of three peaks. The lowest energy peak has a maximum between 1.62 eV and 1.63 eV, with a tail on the low energy side. The other two peaks occur at approximately 1.635 eV and 1.648 eV. The FWM signal reaches its maximum intensity around zero delay, characterized by a broad response encompassing a range of energies above and below the band gap. For longer delays, the signal narrows spectrally and decays on a time scale of a few hundred femtoseconds. Cuts through the two-dimensional FWM results versus time delay are displayed in the upper right panel of Fig. 4.1. The signal exhibits a smooth temporal decay for detection energies above the band gap, while for energies below the band gap oscillations appear. These oscillations resemble beating effects observed in FWM studies in the presence of simultaneous responses due to bound and free excitons in GaAs superlattices [126] and exciton and trion resonances in doped CdTe quantum wells [127]. Together with the observation of three peaks in the four-wave mixing spectrum, this suggests that there are multiple, distinct contributions to the measured FWM response of the perovskite film.

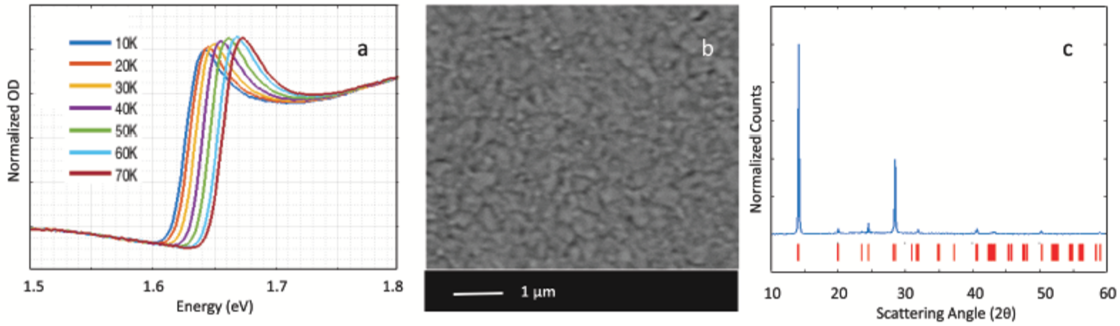

Figure 4.2: Characterization of the $CH_3NH_3PbI_3$ films, showing **a** Teperature dependent linear absorption. **b** scanning electron microscopy and **c** x-ray diffraction. **b** and **c** were taken at room tmperature. The red lines in **c** indicate the calculated peak positions for the tetragonal phase.

Further insight into the transitions contributing to the FWM response may be gained by performing measurements for which the laser pulses used to excite the sample are tuned relative to the band gap energy. The results of these experiments are shown in Fig. 4.3. In each panel, the laser spectrum is indicated by the white curve overlaid on the FWM signal, and the solid red line shows the band gap energy. For all experiments, the laser pulse fluence summed over the two excitation beams was held constant at 4 μJ/cm^2. The existence of a separate contribution to the FWM signal below the band gap is already apparent at early delays from the shape of the contours in the results for excitation at 1.653 eV in Fig. 4.3a. The broadband signal at higher energies in Fig. 4.3a is attributed to free carrier transitions [128] and transitions within the Urbach band tail [12,91,124]. As the laser is tuned below the band gap energy (Fig. 4.3b-Fig. 4.3i), the peak below the band gap grows in intensity relative to the free carrier response. When the laser is tuned to 1.580 eV, only the tail of the laser spectrum weakly excites the low-energy resonance, isolating it from other contributions, indicating a center energy of 1.613 eV and a spectral width of $\sim$18 meV (Fig. 4.3l). When the laser pulses are tuned to 1.570 eV or lower energies, the laser spectrum has negligible overlap with the 1.613 eV peak, and no FWM signal is detected. The discrete resonance we observe in the FWM signal at 1.613 eV is attributed to an excitonic transition within the $\mathrm{CH_3NH_3PbI_3}$ film.

The variation of the magnitude of the FWM signal as the laser pulses are tuned

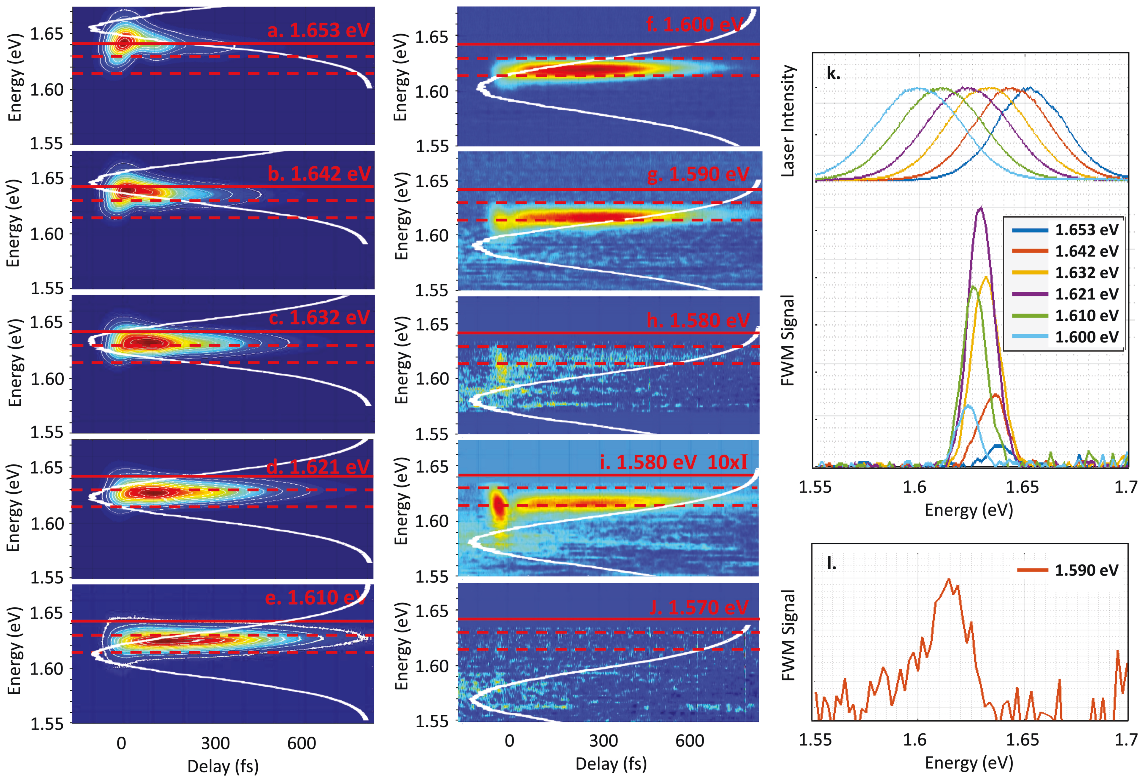

Figure 4.3: (a-j) FWM response of $CH_3NH_3PbI_3$ for varying laser tuning relative to the band gap. The FWM signal is displayed using a coloured contour scale. The white curve overlaid on the FWM results indicates the laser spectrum. The solid red line indicates the 10 K band gap determined by linear absorption. The two dashed lines indicate the resonance energies of 1.613 eV and 1.629 eV determined for the defect-bound and free exciton transition, respectively. The defect-bound exciton appears as a weak, spectrally -isolated peak when the laser is tuned well below band gap (g-i). The free exciton resonance, which produces a much stronger FWM signal than the bound exciton, is evident from the dependence of the FWM signal amplitude on laser tuning (k). In (k) the laser spectra are vertically ofset rom the FWM spectra. The free exciton dominates the FWM singal fro time delays longer than 200 fs: results for 540 fs are shown in (k). (l) FWM spectrum at zero delay fr excitation at 1.590 eV, showing the defect-bound exciton peak. The intensity of the 1.590 eV excitation laser pulses was 10 times larger for the results in i, permitting the defect-bound exciton to be observed more clearly.

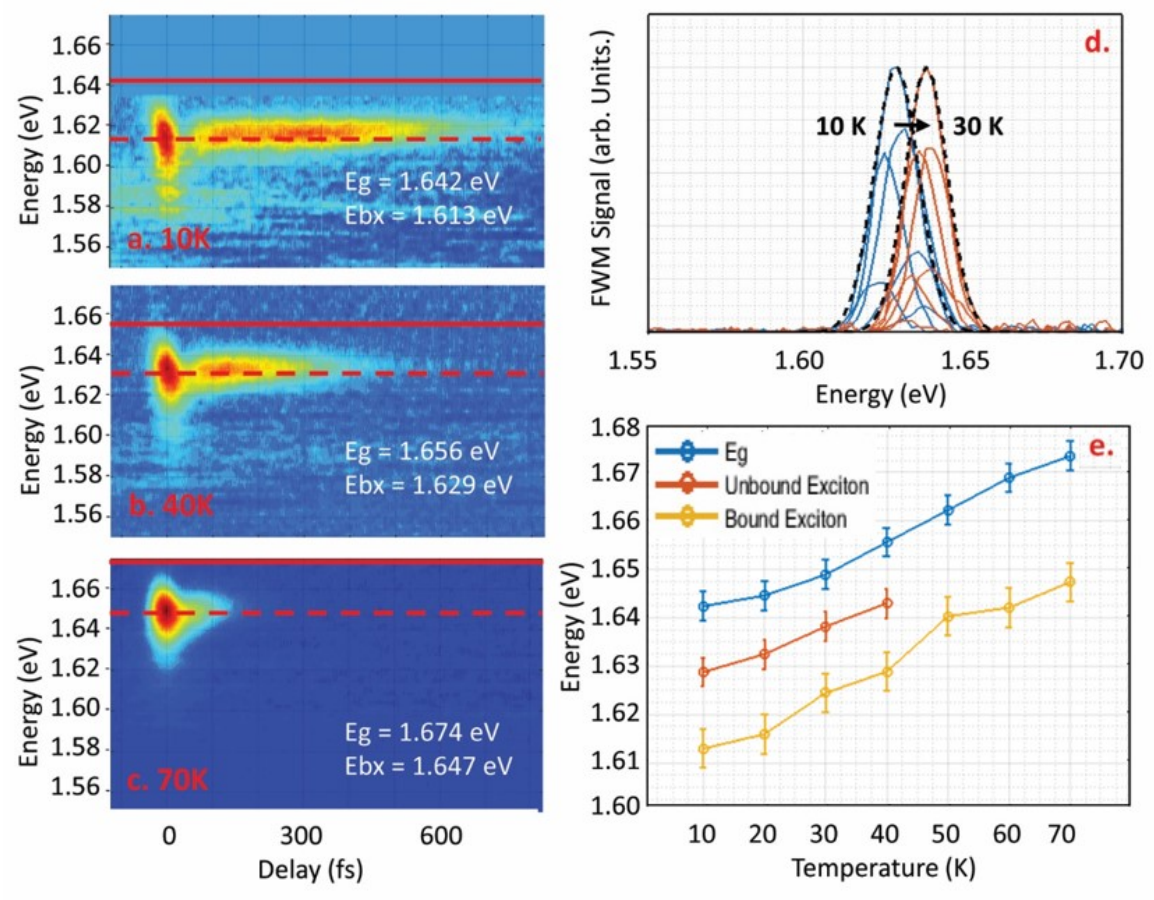

Figure 4.4: FWM response of the defect-bound exciton at (a) 10 K, (b) 40 K, and (c) 70 K with the corresponding bang gap indicated by the solid line. (d) FWM spectrum at 540 fs delay for a variety of spectral tunings, showing the variation in the resonance energy of the free exciton as the temperature is increased from 10 K (blue curves) to 30 K (red curves). The black dashed curves indicate a Gaussian fit to the resonance at each temperature. (e) The exciton transition energies deduced rom the FWM results as a function of temperature. (e) The exciton transition energies deduced from the FWM results as a function of temperature. Both exciton resonance energies follow the temperature dependence of the band gap within the experimental uncertainty, indicating no discernible temperature dependence of the exciton binding energies within the accessible range.

indicates that the resonance feature at 1.613 eV is not the only discrete resonance below the band gap. A stronger resonance occurs at higher energies, as shown in Fig. 4.3k, where the FWM spectrum at 540 fs delay is displayed color-coded with the corresponding laser spectrum in the upper panel. This second resonance has a maximum at 1.629 eV, with a width of 15 meV. The variation of the spectral content of the FWM signal as the laser is tuned indicates inhomogeneous broadening. Both of the resonances at 1.613 eV and 1.629 eV have spectral widths smaller than the laser pulse bandwidth and have transition energies that are fixed as the center photon energy of the laser spectrum is varied. These features are reflective of discrete, excitonic transitions within the semiconductor. The strong 1.629 eV resonance is attributed to the free exciton transition, while the weaker resonance at 1.613 eV is attributed to an exciton bound to defects within the perovskite film. From a comparison of the transition energy of each exciton with the band gap energy, we determine the binding energies of these excitons to be 13 meV and 29 meV, respectively. The temperature-dependence of the FWM response from the two excitons is shown in Fig. 4.4. The free exciton resonance energy could only be determined up to 40 K due to the limited tuning range of the laser relative to the band gap at higher temperatures. The spectral position of the free and defect-bound exciton resonances both track the temperature dependence of the band gap energy, indicating no discernible dependence of the binding energies of the excitons on temperature below 40 K.

The binding energy of 13 meV we measured for the free exciton is in line with the value of 16 meV found from recent magneto-optical measurements at 2 K [18, 19]. In Ref. [18] and Ref. [19], large magnetic fields ($\sim$20 Tesla) enabled the observation of the 2s exciton transition, constraining the value of the binding energy over a much narrower range than in earlier magneto-optical experiments [32, 33]. In our FWM experiments, the free exciton was found to contribute much more strongly than the bound exciton. Together with the higher sensitivity of FWM to excitonic resonances than linear absorption experiments, this accounts for the fact that the bound exciton was not observed in Refs. [18, 19]. The binding energy of the free and defect-bound exciton resonances we observe are both within the large spread of reported values of 2-55 meV for $CH_3NH_3PbI_3$, [13, 18–27, 32, 33, 121–123] shedding some light on the controversy surrounding E_b in recent years . The uncertainty in determining the dielectric constant, including both the choice of appropriate spectral range [30] and the complexity tied to the role of lattice vibrations [22, 26, 27], has also contributed substantially to the wide range of reported binding energies since this value is essential to the modeling of absorption and photoluminescence. Since the transition energies of the free and defect-bound excitons are determined directly using FWM spectroscopy, no modeling is needed and the dielectric constant is not required to determine the binding energies. We note that in a recent work by Even *et al.*, the dielectric constant was taken as a fitting variable in modeling the linear absorption spectrum, yielding a free exciton binding energy of 13 meV at 80 K, in agreement with the value reported here.

The separation between the free and defect-bound exciton resonances is 16 meV. We attribute this to the binding energy of excitons to point defects within the $CH_3NH_3PbI_3$ film. The energy levels tied to a variety of point defects were calculated using density functional theory techniques by Yin *et al.* [88]. All point defects with low formation energies were found to be shallow defects, with energies less than 50 meV away from the band extrema. The reported transition energies in Ref. [88] suggest that the dominant donor MA_i may be responsible for exciton localization at low temperatures in our sample. The small 16 meV binding energy of these defects is consistent with a similar coherence decay time observed for the free and defect-bound excitons in our experiments (Fig. 4.5), which is a signature of weak localization [129]. Our findings are also in line with an exciton localization energy of 17 meV determined from photoluminescence and THz studies on $CH_3NH_3PbI_{3-x}Cl_x$ [16]. Static disorder associated with the frozen methylammonium cations at low temperatures [22, 90] may contribute to inhomogeneous broadening of the exciton resonances, which is reflected by the measured linewidths being $\sim$5 times larger than the homogeneous width estimated from the duration of the coherent emission. As the localization energy is determined here with a precision of a few meV (limited by the level of inhomogeneous broadening), the 16 meV value we report will support theoretical models of point defects in $CH_3NH_3PbI_3$.

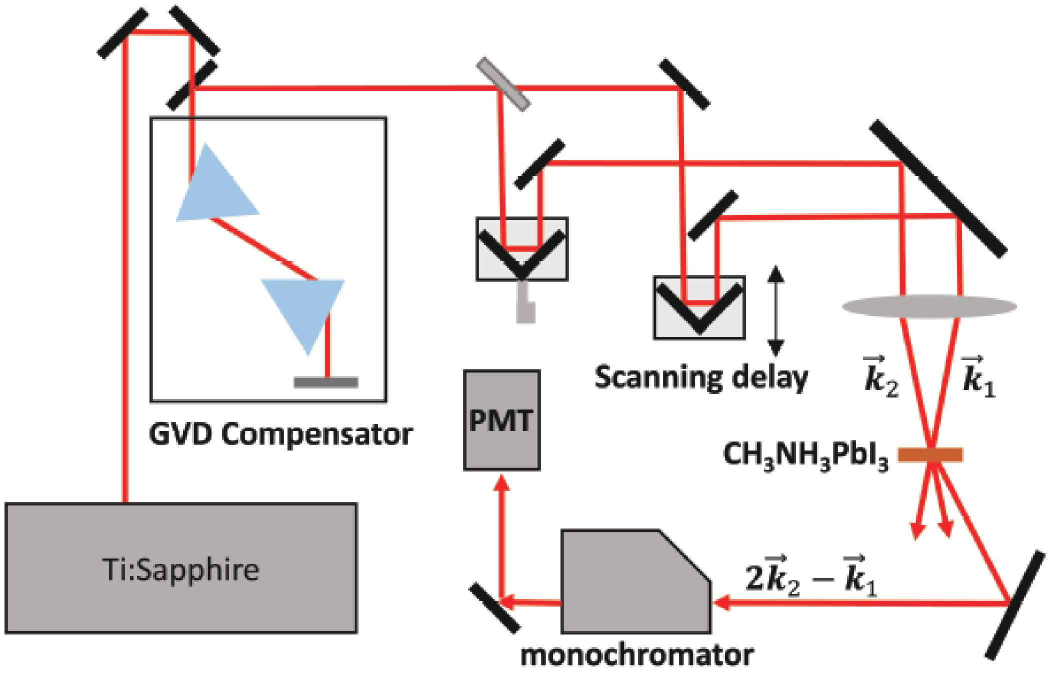

Figure 4.5: Schematic diagram of the two-pulse degenerate four-wave mixing apparatus

Multiple emission peaks have also been observed in photoluminescence experiments on single crystals of $CH_3NH_3PbI_3$ [29], however the energy separation between the emitting exciton resonances was considerably larger than that found using FWM techniques in this work. As FWM detects the states participating in absorption, this suggests that carriers relax into deeper energy levels prior to radiative recombination. Our observations, which verify the existence of weakly localized exciton states in this system, are in agreement with recent power-dependent photoluminescence studies which determined that excitons recombine radiatively from trap states [16] and transient photoconductivity experiments that indicated a resonant transition below the band gap tied to localized states [125]. Our findings are also consistent with earlier four-wave mixing experiments in disordered III-V superlattices revealing simultaneous signatures of free excitons and excitons bound to neutral Carbon acceptors [126].

4.4 Conclusions

The application of coherent nonlinear optical spectroscopy to $CH_3NH_3PbI_3$ reported here complements and extends the numerous studies of this system using linear optical techniques in recent years, for which the substantial broadening inherent to the disordered organic inorganic perovskite materials obscures fundamental photophysical properties such as excitonic effects, leading to challenges in assessing crucial parameters for solar cell design. Since FWM preferentially detects optical species possessing long coherence decay times, this technique is highly sensitive to excitonic transitions, a feature that has been exploited for studying excitons in clean and disordered III-V and II-VI semiconductors over more than two decades [47, 70, 72, 126, 127]. The direct observation of the resonance energies of both free and defect-bound excitons in $CH_3NH_3PbI_3$, eliminating the need to rely on assumed values of the dielectric constant for determination of the associated binding energies, aids in clarifying the broad range of values of the exciton binding energy reported in recent years as the relative role of free and defect-bound excitons will vary depending on whether absorption or photoluminescence based detection schemes are utilized. The observation of defect-bound excitons using a technique based on nonlinear absorption indicates that both free and localized exciton species play a role in an operational solar cell. The measured localization energy for bound excitons of 16 meV reported here provides input to theoretical models of defects in $CH_3NH_3PbI_3$. Our findings demonstrate the power of FWM spectroscopy for studying excitonic properties and the influence of disorder in $CH_3NH_3PbI_3$, laying the foundation for studies on other materials within the organometal halide perovskite class of semiconductors, and will aid in improving solar cell device performance using these materials.

4.5 Acknowledgements

This research is supported by the Natural Sciences and Engineering Research Council of Canada.

Chapter 5

Four-Wave Mixing in Perovskite Photovoltaic Materials Reveals Long Dephasing Times and Weaker Many-Body Interactions than GaAs

Authors: Samuel A. March[1], Drew B. Riley[1], Charlotte Clegg[1], Daniel Webber[1], Xinyu Liu[2], Margaret Dobrowolska[2], Jacek K. Furdyna[2], Ian G. Hill[1] and Kimberley C. Hall[1]

[1]Department of Physics and Atmospheric Science, Dalhousie University, Halifax, Nova Scotia B3H4R2, Canada

[2]Department of Physics, University of Notre Dame, Notre Dame, IN 46556

Reprinted with permission from ACS Photonics **4**, 1515-1521 (2017). Copyrighted 2017 by the American Chemical Society.

Kimberley C. Hall, and Murat Yildirim developed the four-wave mixing techniques. Samuel March performed the four-wave mixing experiments, the data analysis, linear absorption and SEM sample characterization. Daniel Webber designed and built part of the apparatus. The thin-films of MAPI were prepared and characterized using XRD by Charlotte Clegg at Dalhousie under the supervision of Prof. Ian Hill. The GaAs films were grown by Dr. Xinyu Liu and Dr. Margaret Dobrolowska under the supervision of Prof. Jacek Furdyna. Kimberley C. Hall and Samuel March conceived and designed the experiments. Samuel March and Kimberley C. Hall wrote the manuscript with input from all authors.

Strong many-body interactions are common among inorganic semiconductors used in the highest efficiency single-junction solar cells. GaAs in particular has achieved the highest single-junction solar cell efficiency on record due to the low achievable defect densities in the highly refined system. MAPI is a hybrid organic-inorganic system with high defect densities, yet MAPI solar cells have achieved higher efficiencies than some inorganic solar cells including multicrystalline silicon. In this study we used FWM spectroscopy to compare the many-body interactions in the archetypical inorganic semiconductor GaAs and the archetypical perovskite semiconductor MAPI to clarify if the high efficiencies recorded for perovskite solar cells was due to a similarity to inorganic semiconductors. We found that Many body interactions were substantially weaker in the MAPI system, revealing a stark contrast between MAPI perovskite and inorganic semiconductors. This study helps place perovskite in the context of other high performing semiconductor materials, leading the way to understanding the fundamental properties of this unique, high performing solar cell material.

5.1 Abstract

Perovksite semiconductors have shown promise for low-cost solar cells, lasers and photodetectors, yet their fundamental photophysical properties are not well understood. Recent observations of a low exciton binding energy and evidence of hot phonon effects in the room temperature phase suggest that perovskites are much closer to inorganic semiconductors than the absorber layers in traditional organic photovoltaics, signaling the need for experiments that shed light on the placement of perovskite materials within the spectrum of semiconductors used in optoelectronics and photovoltaics. Here we use four-wave mixing (FWM) to contrast the coherent optical response of $CH_3NH_3PbI_3$ thin films and crystalline GaAs. At carrier densities relevant for solar cell operation, our results show that carriers interact surprisingly weakly via the Coulomb interaction in perovskite, much weaker than in inorganic semiconductors. These weak many-body effects lead to a dephasing time in $CH_3NH_3PbI_3$ $\sim$3 times longer than in GaAs. Our results also show that the strong enhancement of the exciton FWM signal tied to excitation-induced dephasing in GaAs and other III-V semiconductors does not occur in perovskite due to weak exciton-carrier interactions.

5.2 Introduction

Since the first integration of organo-lead trihalide perovskites into photovoltaic devices, [53] the efficiencies of solar cells using this material as the primary absorber layer have increased at an unprecedented rate, having reached over 20% in just a few years. [5] Progress in understanding the fundamental physical properties of these materials has been much slower to develop as the organic-inorganic pervskites are much more complex than both the typical organic semiconductors used in solution-processed photovolatics and traditional inorganic semiconductor solar cell materials. The relative importance of excitons and free carriers to the optical response and carrier transport in perovskite systems has been the subject of considerable controversy, [14, 15, 18, 20, 22–24, 27, 30, 32, 33, 130] although a consensus is now emerging that excitonic effects are weaker than had previously been thought, [18, 22, 24, 27] with optical phonons and the rotational motion of the $CH_3NH_3^+$ cations being identified as an essential contributor to dielectric screening and an associated reduction in the exciton binding energy (E_b). [22] Together with recent experiments showing evidence of phonon bottleneck effects [96] and the successful interpretation of numerous dynamic optical experiments considering only free carriers, [11, 17, 21, 95, 96, 131–133] this suggests that the organo-lead trihalide perovskites are more similar to direct band gap III-V semiconductors like GaAs than solution-processed organics in which excitonic effects govern both optical excitation and transport. [134] Nevertheless, many open questions remain regarding the fundamental photophysical properties of these promising photovoltaic materials.

Here we contrast the *coherent* carrier dynamics in solution-processed perovskite films with the inorganic semiconductor GaAs using the powerful spectroscopic technique of femtosecond four-wave mixing, providing insight into where perovskite semiconductors fit into the broader landscape of materials used in photovoltaic technology. In a FWM experiment, two laser pulses $\vec{E}_1(t)$ and $\vec{E}_2(t-\tau_d)$ with wave vectors $\vec{k}_1$ and $\vec{k}_2$ excite a third-order polarization that emits in the direction $2\vec{k}_2 - \vec{k}_1$ (see Fig. 5.1, and Supplementary Information). The magnitude of the emitted signal, often referred to as *self diffraction*, versus the delay time τ_d probes the decay of quantum coherence within the system of electron-hole pairs excited by the laser pulse, providing a direct measurement of the time scale tied to the strongest scattering process following optical excitation. Interactions within the system of excited carriers and/or excitons lead to additional contributions to the self-diffraction signal, making this technique especially sensitive to many-body effects. [47] As a result of this high sensitivity, fundamental interactions such as electron-electron scattering or exciton-free carrier scattering, which together with electron-phonon coupling govern the relaxation, drift and diffusion of carriers following optical excitation in an operating device, may be studied at low carrier densities reflective of solar cell operating conditions.

While evidence of many-body effects such as Auger recombination and band gap renormalization have been observed in perovskites at large carrier densities $\gtrsim 1\times10^{18}$ cm^{-3}, [96, 132, 135] our experiments demonstrate that at densities relevant for solar cell device operation Coulomb-mediated scattering plays a negligible role in carrier dephasing, indicating that charge carriers in $CH_3NH_3PbI_3$ interact surprisingly weakly. This finding represents an unexpected divergence from the inorganic semiconductors such as GaAs, in which such many-body effects contribute at densities as low as 10^{13} cm^{-3}, and are stronger than all competing interactions for temperatures up to 300 K and carrier densities down to 10^{15} cm^{-3}. [63,72,77,79,84,86] In addition to causing a three-fold larger 10 K interband dephasing time relative to GaAs, our results show that the weak many body effects in perovskite have the consequence that the dramatic enhancement of the exciton FWM signal in GaAs tied to excitation-induced dephasing does not occur. These weak many-body effects highlight a fundamental difference in the nature of charge carrier scattering in perovksite relative to inorganic semiconductors, with crucial implications for both understanding charge dynamics following optical excitation and for optimizing solar cell performance.

5.3 Weak Exciton-Carrier Scattering in $CH_3NH_3PbI_3$

The four-wave mixing response of the $CH_3NH_3PbI_3$ film is shown in Fig. 5.2(a), illustrating the variation of the signal characteristics as the center photon energy of the laser pulse is tuned relative to the band gap energy. For these results, the perovskite film was held at 200 K in a liquid N_2 cryostat. The corresponding results for

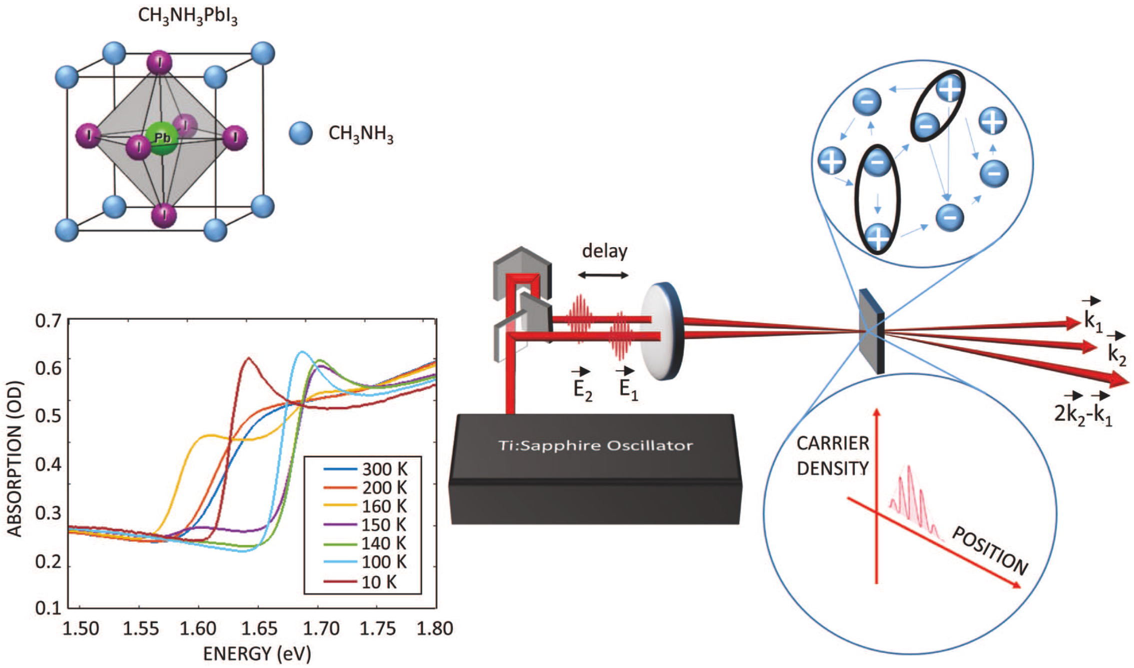

Figure 5.1: (Right) **Transient four-wave mixing spectroscopy**: Interference of $\vec{E_2}$ with the coherent polarization density excited by $\vec{E_1}$ results in a spatially-modulated carrier density in the semiconductor sample. Self-diffraction of $\vec{E_2}$ (non-interacting two-level system) or the polarization density excited by $\vec{E_2}$ (via many-body interactions within the system of electron-hole pairs) constitutes the four-wave mixing signal emitted along $2\vec{k_2}$-$\vec{k_1}$. Top left: Methyl-ammonium lead-iodide perovskite crystal structure. CH_3NH_3 (blue), Pb (green), I (purple). Bottom left: Absorption spectrum versus temperature, indicating the phase transition around 160 K. [23]

GaAs at 200 K are shown in Fig. 5.2(b). Despite a similar estimated exciton binding energy in the room temperature phase of $CH_3NH_3PbI_3$ and GaAs, [18, 22, 24] as well as a similar Urbach energy, [12] the coherent response from the two materials differs dramatically. In GaAs, the FWM signal consists of a prominent exciton peak, and a broad peak at higher energy associated with unbound electron-hole pairs excited on optical transitions above the band gap. In contrast, for the pervoskite sample the FWM signal is smooth and featureless for all laser tuning conditions: Only the overall magnitude of the response varies with laser tuning (Fig. 5.2(c)). The spectral dependence of the FWM signal from the perovskite film at 200 K is similar to the laser excitation spectrum (Supplementary Fig. 5.8), indicating only a free carrier response. The results of FWM experiments on the perovskite film at 10 K are shown in Fig. 5.3(a). In addition to the interband response above the band gap, a weak shoulder below the band gap is apparent and attributed to the FWM response of the exciton. [48] FWM results on GaAs at 10 K are shown in Fig. 5.3(c). While in perovskite the exciton and interband signals are comparable in magnitude, in GaAs a giant exciton FWM signal is detected. The large exciton signal measured in GaAs exceeds the interband response by a factor of approximately 15.

The large exciton signal observed in the FWM response of GaAs, which contrasts with the linear absorption spectrum at 200 K that shows no discernible exciton (Fig. 5.2(d)), has been studied extensively and is tied to scattering between the excitons and free carriers mediated by the Coulomb interaction (see Supplementary Information for more details). [63, 72, 77, 79, 84] This many-body interaction, typically referred to as *excitation-induced dephasing*, results in an additional FWM signal at the exciton that is proportional to the slope of the density dependent dephasing rate. This EID signal is much larger than the non-interacting exciton self-diffraction signal (*i.e.* the response expected from a simple two-level system), allowing the exciton FWM signal to persist in GaAs to temperatures beyond 250 K despite the small exciton binding energy of 4 meV. This many-body signal is easily distinguished from a non-interacting signal because the width of the exciton peak versus delay is determined by the bandwidth of free carrier transitions excited by the laser pulse rather than the intrinsic dephasing rate of the exciton, a consequence of interference between contributions to the overall exciton diffraction signal from free carriers at

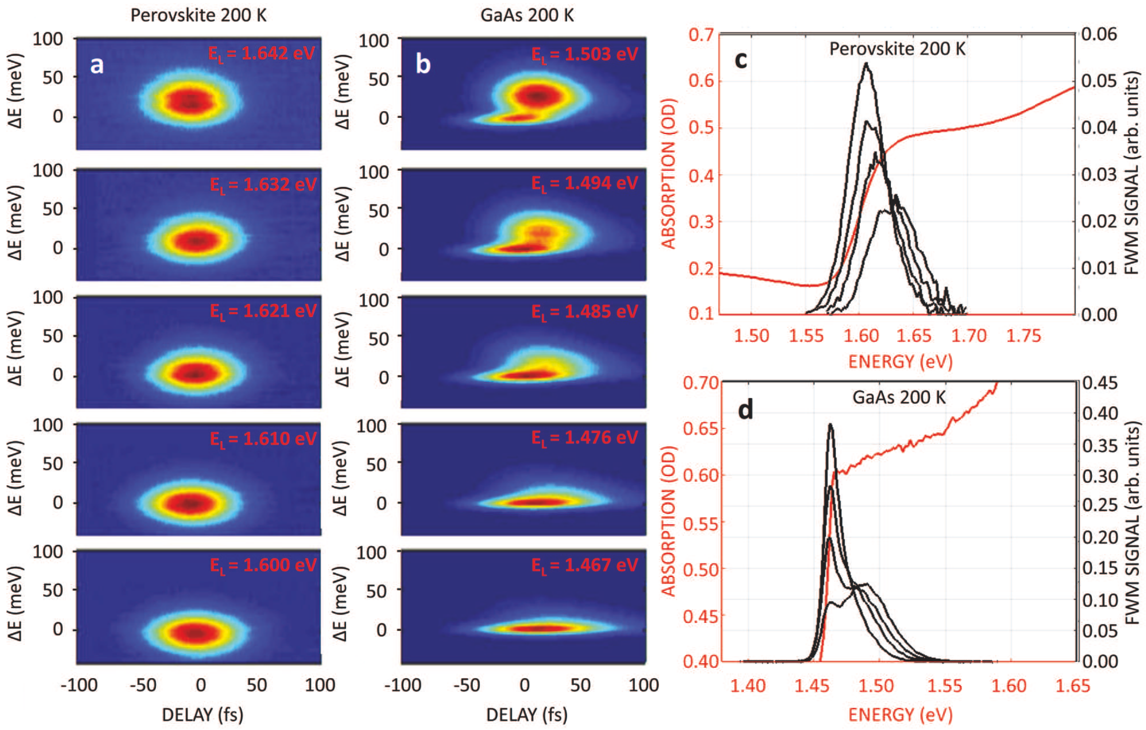

Figure 5.2: **Comparison of four-wave mixing response at 200 K from the $CH_3NH_3PbI_3$ thin film and single crystal GaAs**. The amplitude of the four-wave mixing signal normalized to the peak value (colour scale) is shown as a function of the time delay between the two excitation laser pulses and the detection energy (E_D) for different values of the detuning of the laser energy (E_L) from the band gap energy (E_g) ($\Delta E \equiv E_D - E_g$). **a** Results on $CH_3NH_3PbI_3$, with E_g = 1.606 eV, and laser tuning from 1.600 eV (bottom panel) to 1.642 eV (top panel). **b** Same results for GaAs, with E_g = 1.465 eV and laser tuning from 1.465 eV (bottom panel) to 1.503 eV (top panel). GaAs shows separate responses from the exciton and free carrier transitions, where the strong exciton peak is caused by Coulomb coupling of the exciton with the free carriers via excitation-induced dephasing. In contrast, the $CH_3NH_3PbI_3$ shows only a signal from free carrier transitions. **c** Linear absorption (red) is shown with spectral slices of the contour plots in **a** at zero delay for $CH_3NH_3PbI_3$. **d** Same data for GaAs. For GaAs, the laser tuning determines the relative size of the exciton and free carrier response, whereas in perovksite only the magnitude of the free carrier response varies with tuning.

different energies. [72, 77, 79, 84]

It is important to note that the lack of a strong FWM signal tied to excitons in $CH_3NH_3PbI_3$ does not imply that excitonic effects (including Sommerfeld enhancement in the vicinity of the band gap) are weak. Excitonic effects result from the Coulomb interaction between electrons and holes and dictate the ground state excitations of the system. In contrast, our results provide direct insight into the strength of *many-body* effects, which concern the coupling of electron-hole pairs with each other and lead to a hierarchy of interactions and associated FWM signal contributions. [136] In GaAs, the EID signal at the exciton results from four-particle correlations tied to scattering between bound and/or unbound electron-hole pairs. The lack of a strong exciton signal in the results of FWM experiments on the perovskite sample indicates that such scattering interactions are weak (or equivalently that the exciton dephasing rate is not dependent on the excited carrier density, corresponding to a negligible EID coefficient), in sharp contrast to GaAs.

A large exciton tied to the same EID many-body process has been observed in experiments on a range of inorganic semiconductors (GaAs, InGaAs, InP, Ge) and in a variety of situations in such materials (quantum well excitons, magneto-excitons, and excitons tied to the spin-orbit split-off band gap). [72, 77, 79, 84] Furthermore, strong exciton-carrier scattering has been observed in these systems at densities as low as 1×10^{13} cm^{-3}. [63] The weak exciton response in the perovskite thin film suggests that exciton-carrier scattering effects are negligible in this system, representing a fundamental departure from the inorganic semiconductors with respect to many-body interactions, and thus a fundamental difference in the physical processes governing carrier relaxation and transport in these materials.

5.4 Long Interband Dephasing Time in $CH_3NH_3PbI_3$: Weak Carrier-Carrier Scattering

The coherence decay time (τ) indicates the time scale associated with the fastest scattering events for either electrons or holes following optical excitation, including potential interactions with defects, phonons or other charge carriers. For unbound electron-hole pairs, τ may be extracted from the decay of the FWM signal above the band gap versus the interpulse delay by fitting to a standard photon echo response

[62] (see Supplementary Information for more details). While the decay of the interband response at 200 K in both GaAs and perovskite is comparable to our time resolution ($\sim$50 fs), for both samples the dephasing dynamics are resolvable at 10 K. The delay dependence of the 10 K FWM signal was analyzed at a detection energy 10 meV above the band gap, yielding the scattering time associated with low-energy unbound electron-hole pairs. The dephasing time extracted from the results on the perovskite sample in Fig. 5.3(a) is 220 fs. The results for GaAs in Fig. 5.3(c) yield a dephasing time of 60 fs. The slower coherence decay for electron-hole pairs in $CH_3NH_3PbI_3$ is surprising given the relatively high density of defects present in the solution-processed film. The density of defects in similar films has been estimated at 1×10^{16} cm^{-3} to 2×10^{17} cm^{-3}, [137, 138] much larger than in crystalline GaAs for which the defect densities are typically $\lesssim 10^{14}$ cm^{-3}.

The slower carrier dephasing in $CH_3NH_3PbI_3$ relative to GaAs is due to much weaker Coulomb scattering between free carriers in the perovskite sample, as shown in Fig. 5.4, which shows τ versus the optically-injected carrier density (n_{eh}, evaluated using the measured total absorbed power from both excitation beams, laser repetition rate, sample thickness and measured laser spot size). The rapid interband dephasing process in GaAs has been well characterized and is governed by strong carrier-carrier scattering, described by a dephasing rate $\frac{1}{\tau} = \frac{1}{\tau_0} + cn_{eh}^{\frac{1}{3}}$, where the $\frac{1}{3}$ exponent describes carrier-carrier scattering in the bulk film (*i.e.* for carriers with 3 degrees of freedom of motion), c is the EID coefficient, and the offset $\frac{1}{\tau_0}$ is due to coupling to phonons. [65, 139] Fig. 5.4 shows the measured dephasing time at 10 K from our GaAs film as a function of n_{eh}. For comparison, the results of measurements in bulk GaAs at 300 K from Ref. [[139]] are also shown in Fig. 5.4. All of the measured results for GaAs fit well to the 1/3 power law, showing dominant carrier-carrier scattering. In Ref. [[139]] the 1/3 power law was found to hold over three orders of magnitude in density, down to 2×10^{15} cm^{-3}, and a strong dependence of the dephasing rate on carrier density has been observed in earlier studies in GaAs for n_{eh} as low as 1×10^{13} cm^{-3}. [63]

The dephasing time for the $CH_3NH_3PbI_3$ sample is independent of n_{eh} over the accessible measurement range down to 4×10^{15} cm^{-3}. (The range of accessible carrier density is limited by laser power on the high side and signal to noise and

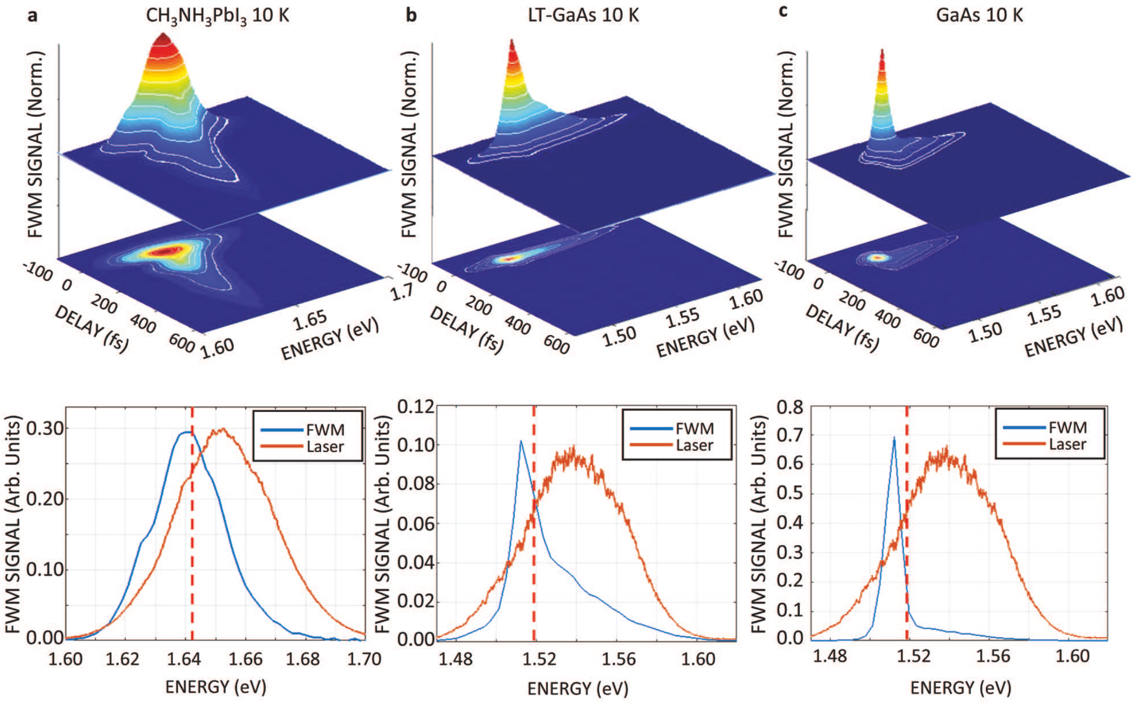

Figure 5.3: **Four-wave mixing results for $CH_3NH_3PbI_3$, low-temperature-grown GaAs, and GaAs at 10 K**. Upper panels: FWM signal (contour scale) versus pulse delay and photon energy. Lower panels: spectral cuts at zero delay together with laser spectrum. The band gap for each sample is indicated by the dashed line. LT-GaAs and GaAs both show an exciton response caused by exciton-carrier scattering, indicating that defect-induced localization associated with the high density of defects in the LT-GaAs film ($\sim 10^{19}$ cm^{-3}) does not suppress many-body effects. For the perovskite sample, only a weak exciton signal relative to the interband response is observed and the coherent emission persists to longer time scales than GaAs or LT-GaAs, indicating weak many-body interactions tied to exciton-carrier and carrier-carrier scattering.

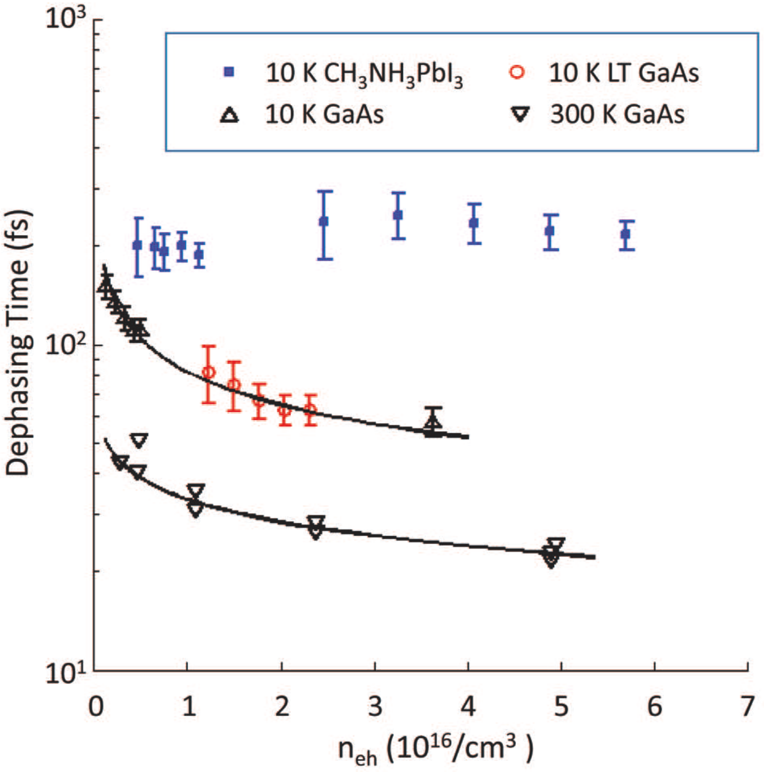

Figure 5.4: **Electron-hole pair dephasing times versus the excited carrier density for $CH_3NH_3PbI_3$, low-temperature-grown GaAs, and GaAs**. The 10 K results for GaAs and LT-GaAs from Ref. [65] were taken on the same samples as studied in this work. The 300 K GaAs experimental data and fit were extracted from Ref. [139]. The dephasing time for perovskite is >3 times larger than GaAs under the same conditions and is independent of carrier density, indicating that carrier-carrier scattering does not contribute to dephasing. This contrasts with GaAs, for which carrier-carrier scattering dominates over all other interactions at densities down to 1×10^{15} cm^{-3} and temperatures up to 300 K. [63, 139]

on the low side.) The 10 K measured value for τ in GaAs of 60 fs corresponds to a more than 3-fold shorter value in crystalline GaAs than in the solution-processed $CH_3NH_3PbI_3$ film. These results indicate that, at the densities relevant for solar cell device operation ($\lesssim 10^{16}$ cm^{-3}), Coulomb-mediated carrier carrier scattering is negligible within the perovskite system, in contrast to GaAs in which such effects strongly dominate.

5.5 Role of Defects: Comparison to Low-temperature-grown GaAs

A possible explanation for the weak many-body effects we observe in $CH_3NH_3PbI_3$ is strong carrier localization tied to the high density of defects in the solution-processed film. [135] Recent calculations using density functional theory suggest that the density of deep defects is low in this system, accounting for the long observed diffusion lengths tied to weak non-radiative recombination, [11] but that there is still a high density of shallow point defects tied to methylammonium interstitials and lead vacancies. [88] In addition to these shallow point defects, a shallow spatially-varying potential is present associated with long-range correlated orientations of methylammonium molecules, which results in static disorder at low temperatures and dynamic disorder at room temperature. [90] The shallow local potential fluctuations caused by the above defects and correlated MA orientations can lead to charge localization, which may reduce the strength of Coulomb coupling between charge carriers in $CH_3NH_3PbI_3$.

In order to gain insight into the potential role of defects in reducing many-body effects, here we contrast the FWM responses of the GaAs and perovskite samples with corresponding measurements on a companion GaAs sample grown at a lower substrate temperature (250°C), for which defects are intentionally incorporated. The resulting material is commonly referred to as low-temperature-grown GaAs (LT-GaAs), and has been studied extensively over the past two decades due to its applicability to THz sources and detectors. [140] Growth at 250°C leads to excess As, including a large density ($\sim 1\times10^{19}$ cm^{-3}) of As_{Ga} antisite defects and As clusters that cause both mid-gap trap states and local potential fluctuations. [140]

The results of FWM experiments on the LT-GaAs sample are shown in Fig. 5.3(b). The FWM spectrum consists of a distinct exciton peak and a broadband response associated with the transitions above the band gap, similar to the results in GaAs (Fig. 5.3(c)) albeit with a weaker fractional response from the exciton in comparison to the interband transitions. A shoulder is also observed for photon energies below the exciton in LT-GaAs, which has been attributed to the Urbach band tail tied to As disorder. [70] The key observation for the purposes of this work is that the exciton feature remains in the FWM response of LT-GaAs despite the large amount of disorder. Recent prepulse four-wave mixing experiments have confirmed that the observed exciton peak in LT-GaAs is caused by exciton-carrier scattering. [64] The dephasing process of free carriers is also dominated by carrier-carrier scattering in LT-GaAs, as shown in Fig. 5.4.

The dominant influence of many-body effects on the carrier kinetics in LT-GaAs mimics the situation in GaAs, suggesting that the high density of defects in the LT-GaAs film does not strongly reduce interactions between charge carriers. The origin of the weak Coulomb interactions among carriers in the $CH_3NH_3PbI_3$ system, which possesses a lower defect density than LT-GaAs by several orders of magnitude, is therefore unclear. Nevertheless, a role played by disorder cannot be ruled out as carrier localization effects will be a sensitive function of the depth and correlation length of the defect-induced local potential fluctuations. [141] Both the nature of defects and their influence on charge localization are currently under intense investigation in the methylammonium trihalide perovskite family of materials. [88, 90]

The slow spatial variation of the potential tied to the MA cation orientation in the organic-inorganic perovskite has no analog in inorganic semiconductors. The similar strength of many-body interactions within GaAs and LT-GaAs points to this slowly-varying potential, rather than point defects, as the most likely source of carrier localization and associated diminished many-body interactions in the hybrid perovskites. We note that evidence for large polaron formation and a reduction in the carrier cooling rate has been observed in single crystals of $CH_3NH_3PbBr_3$ [142] and more recently in $CH_3NH_3PbI_3$ solution processed films [143], where the orientational motion of the MA cations in the tetragonal phase screens the Coulomb interaction responsible for electron-LO phonon coupling (Fröhlich interaction). We observe evidence for weak many-body effects in both the tetragonal phase (via weak exciton-carrier scattering) and in the orthorhombic phase (via weak exciton-carrier and carrier-carrier scattering). Dynamic large polaron formation likely plays a role in our findings within the tetragonal phase, representing a dynamic self-trapping process. The localization effect we observe in the orthorhombic phase tied to the correlated (yet frozen) MA orientations is a static version of this process, resulting in a similar protective effect that reduces the rate of scattering between electron-hole pairs.

5.6 Conclusions and Outlook

The emergence of $CH_3NH_3PbI_3$ for high efficiency solar cell applications has introduced a complex yet urgent materials science challenge in the need to unravel the photophysical properties of these materials, for which the combination of both organic and inorganic constituents has led to unexpected high performance as well as subtle complexities. This fundamental understanding must be developed in the context of competing technologies based on organic and inorganic solar cell materials. The scattering processes that occur during carrier relaxation, drift and diffusion are especially crucial to device function. While incoherent techniques such as pump probe spectroscopy have provided valuable information about carrier cooling and recombination, assessing the relative strength of the operative scattering processes is essential, especially at carrier densities relevant for an operating solar cell device. Direct access to such scattering process necessitates a *coherent* optical probe that measures the time scale for decay of quantum coherence within the electron-hole pair system, reflecting the transition between the quantum kinetic and thermal regimes following optical excitation of the semiconductor.

By contrasting the coherent nonlinear optical response of a $CH_3NH_3PbI_3$ thin film with crystalline GaAs, our experiments illuminate crucial differences between perovskites and inorganic semiconductors used in solar cells and optoelectronics. At densities relevant for solar cell device operation, there is no evidence of many-body effects in perovskite, despite the fact that such effects strongly dominate the carrier kinetics in inorganic group III-V and group IV semiconductors. These weak many body effects are evidenced by a lack of many-body-related enhancement of the exciton four-wave mixing signal tied to weak exciton-carrier scattering and a dephasing time for free carriers that is independent of density. The former effect is observed in both the tetragonal and orthorhombic phases, indicating that the weak many-body effects are a universal property of the material. These findings are in stark contrast with our experimental results in GaAs and LT-GaAs, for which these many-body scattering effects strongly dominate. Our experiments highlight the need for further studies to characterize disorder and it's potential influence on carrier localization within the organic-inorganic perovskite solar cell materials, including the importance of the long-range correlated potential tied to the methylammonium cation orientations.

5.7 Acknowledgements

This research was supported by the Natural Sciences and Engineering Research Council of Canada and the Canada Research Chairs Program. The work at Notre Dame was supported by NSF Grant DMR100432.

5.8 Supporting Information

5.8.1 $CH_3NH_3PbI_3$ thin-film preparation

The $CH_3NH_3PbI_3$ samples were prepared using a modified sequential deposition procedure reported in [118]. A solution in DMF of 1M PbI_2 (mixed under argon) was stirred at 70°C for 12 hours. The solution was filtered through a 0.45 μm pore PTFE filter into a 70°C, clean glass vial prior to sample preparation. The temperature of the lead iodide solution was maintained at 70°C throughout the deposition. 300 μl of the solution was cast onto a static sapphire substrate at room temperature, and then spun at 5000 rpm for 60 seconds. The lead iodide film was transferred to a 70°C hotplate for 15 minutes to remove the residual solvent. 300 μl of methylammonium iodide solution in isopropanol was deposited onto the lead iodide film, rotating at 4000 rpm for 60 seconds. The films were then annealed in an argon atmosphere at 100°C for 2 hours. Samples were stored under argon, and subsequently transferred to the optical cryostat within the glove box prior to optical experiments to avoid exposure to air. Characterization of the $CH_3NH_3PbI_3$ thin film morphology using scanning electron microscopy indicated good uniformity Fig. 5.5. The absorption spectrum was measured using a CARY UV-VIS absorption spectrometer as a function of temperature (see Fig. 5.1), showing the Varshni blue shift with increasing temperature typical of lead composite semiconductors with positive thermal expansion coefficient of the bandgap. The phase transition around 160 K is also observed, in agreement with previous work [23]. X-ray diffraction on a companion sample grown with the same recipe indicated full conversion to perovskite with no residual lead iodide.

5.8.2 Molecular beam epitaxy growth of GaAs and LT-GaAs

The GaAs epilayers were grown using molecular beam epitaxy. A 100 nm GaAs buffer layer was deposited onto a GaAs (001) semi-insulating substrate, followed by 175 nm of $Al_{0.27}Ga_{0.73}As$, forming a stop etch layer. 800 nm of GaAs was then deposited on top of the $Al_{0.27}Ga_{0.73}As$ layer. The substrate was held at 600°C throughout the deposition of all layers for the GaAs sample, while for the LT-GaAs sample the substrate temperature was lowered to 250°C prior to deposition of the 800 nm top layer. In preparation for four-wave mixing experiments, the samples were glued face down to c-cut, 1 mm thick sapphire windows with Norland optical adhesive, and the substrate was removed using mechanical grinding followed by wet etching. Linear absorption measurements on the GaAs and LT-GaAs films were carried out using a continuous wave white light source (Ocean Optics LS-1) Fig. 5.6. The absorption coefficient was extracted from the measured transmission data using a self-consistent analysis taking into account Fabry-Perot effects. Some residual Fabry-Perot oscillations appear in the data below band gap (*e.g.* the small bump and dip around 1.49 eV in the absorption spectrum for both samples). The direct band gap occurs at 1.5068 eV. The GaAs sample grown at 600°C shows a clear excitonic peak and sharp band edge response, whereas the defect-rich LT-GaAs sample shows no excitonic peak and a smeared band-edge, consistent with previous linear optical studies on LT-GaAs [144]. The absorption tail below the band gap in LT-GaAs is tied to band tail states and absorption between the mid-gap As_{Ga} impurity band and the conduction band [69].

5.9 Optical experiments

A schematic diagram of the four-wave mixing setup is shown in Fig.5.7. The optical source is a Ti:Sapphire oscillator (Coherent Mira 900 seed). At the sample position, the laser pulse duration is approximately 50 fs after group velocity dispersion (GVD) compensation using a home-built prism pulse compressor. After the pulse compressor, the beam from the laser source is passed through a beam splitter, resulting in a power ratio of 2:1. One beam is reflected from a light-weight retroreflector mounted to the cone of a speaker, enabling approximately 1 ps of path length adjustment, and the other beam is sent along a fixed delay line controlled by a manual translation stage. The speaker is driven with an amplified sinusoidal wave form from a function generator at 12 Hz. This fast scan detection mode enables effective noise cancellation and averages over slow drifts in the laser source intensity. The four-wave mixing signal is directed through a monochromator (Oriel Cornerstone 260) and detected using a photo multiplier tube (PMT). The PMT signal is recorded versus interpulse delay using a National Instruments data acquisition card triggered by the function generator and Labview software. For selected experiments, a pulse picker was inserted prior to the optical setup, resulting in no change in the four-wave mixing signal characteristics down to a rep rate of 800 kHz aside from GVD-induced temporal broadening. For the majority of experiments, the pulse picker was removed to maximize the time resolution of the measurements. The carrier density was estimated from the sum of average powers of the two input excitation laser beams, as well as the measured reflected and transmitted average laser powers taking into account reflections at the cryostat windows surfaces, the interface between the sample and sapphire, and the back surface of the sapphire window. More details regarding the experimental techniques are found in Ref. [145].

5.10 Many-body exciton signal caused by exciton-free carrier interactions

Coulomb interactions between bound excitons and unbound electron-hole pairs may be probed to very low carrier densities in four-wave mixing experiments as these interactions produce a strong signal at the exciton when broad-bandwidth excitation pulses are used to simultaneously excite excitons and free carriers. The free carriers cause a renormalization of the exciton self-energy [146], which leads to both phase-breaking scattering interactions and a shift in the exciton transition energy. These effects, which are referred to as *excitation-induced dephasing* and *excitation-induced shift*, modify the optical parameters of the exciton by an amount that depends on the density of free-carriers. As a result, the polarization excited on the exciton transition can diffract from the population grating excited on the interband transitions, resulting in a strong many-body four-wave mixing signal at the exciton. As the interaction between the exciton and free carriers is independent of the free carrier energy [84], interference between contributions to the free carrier grating at different energies leads to an exciton response with a temporal width that depends on the total bandwidth of free carrier transitions excited. For more information on the coherent response of the semiconductor including many-body interactions, see Refs. [64, 72, 79, 84, 86, 111, 146].

5.11 Extraction of electron-hole pair dephasing times

The dephasing time for electron-hole pairs above the band gap was extracted by fitting the four-wave mixing signal versus the interpulse delay (τ_d) to a photon echo response characteristic of the inhomogeneously-broadened interband transition in the semiconductor. The associated functional dependence was taken from Ref. [62], and is given by:

$$J = Ae^{-\frac{4}{T_2}\tau_d}(1+\Phi(\frac{\delta\omega}{\sqrt{\pi}}\tau_d)) \tag{5.1}$$

where

$$\Phi(x) = \frac{2}{\sqrt{\pi}}\int_0^x e^{-t^2}\,dt \tag{5.2}$$

In Eq. 5.1, $\delta\omega$ is the degree of inhomogeneous broadening calculated from the width of the four-wave mixing spectrum at zero delay, and the dephasing time T_2 is the only fitting parameter. This function was convoluted with a Gaussian pulse with a width equal to the temporal duration of the autocorrelation of the laser pulse measured at the sample position. To reflect the fact that the four-wave mixing signal is a third order nonlinear response, the width of the Gaussian used for convolution was 15% lower than the pulse autocorrelation width. Since $\delta\omega$ and the Gaussian pulse width used for convolution are fixed by experimental measurements, the dephasing time T2 is the only fitting parameter. The error bars in Fig. 5.4 in the main text were found by repeating the fitting procedure taking into account a ±5% fluctuation in the measured width of the pulse autocorrelation and the signal to noise level.

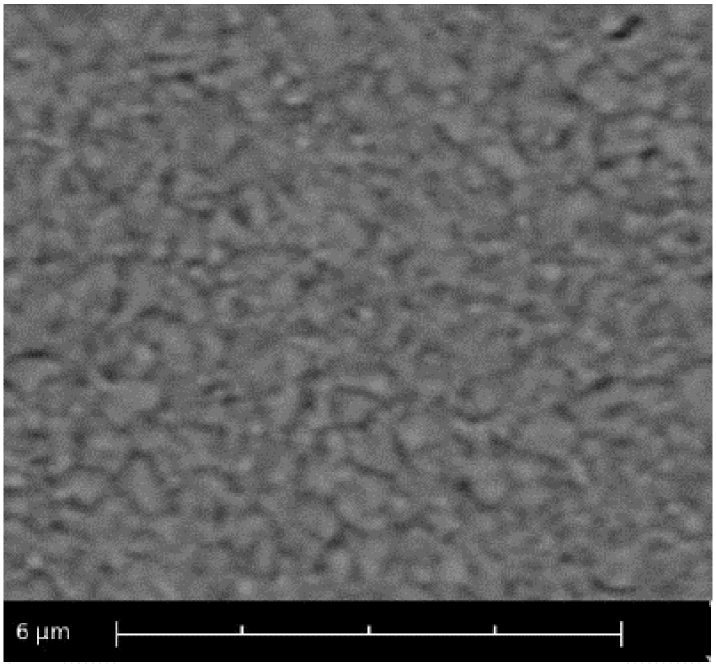

Figure 5.5: SEM image of the $CH_3NH_3PbI_3$ thin-film studied in this work.

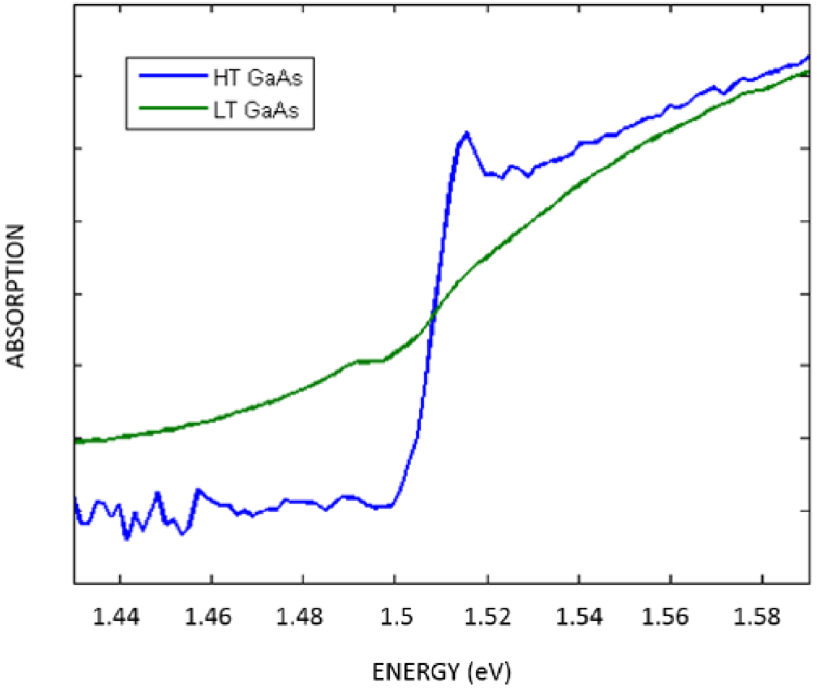

Figure 5.6: Linear absorption spectra at 10 K for high-temperature-grown GaAs (HT-GaAs) and low-temperature-grown GaAs (LT-GaAs).

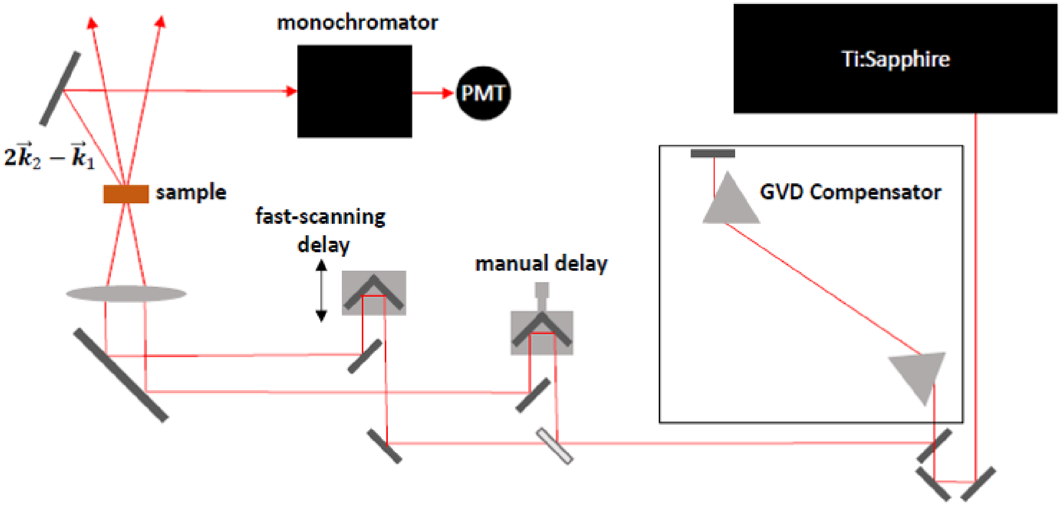

Figure 5.7: Schematic diagram of the four-wave mixing apparatus.

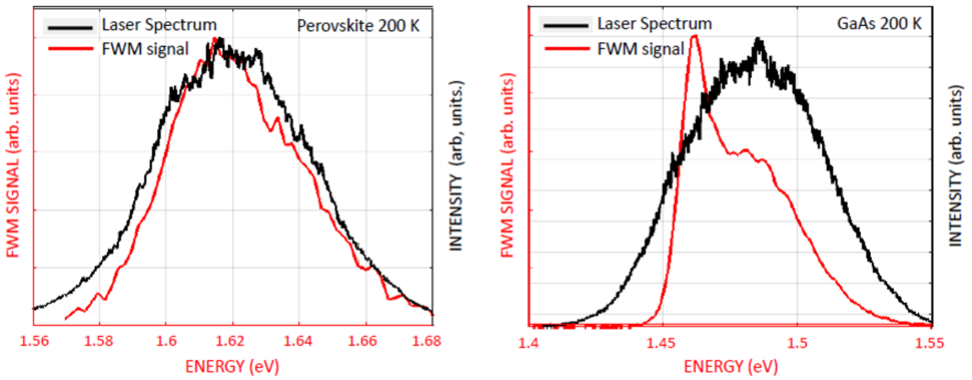

Figure 5.8: Four-wave mixing spectrum at zero delay (red curves) and excitation laser pulse spectrum (black curves) for $CH_3NH_3PbI_3$ (left) and GaAs (right), measured at a sample temperature of 200 K. The GaAs results indicate a coherent response of both exciton and free-carrier transitions, whereas the perovskite sample shows only a free-carrier response.

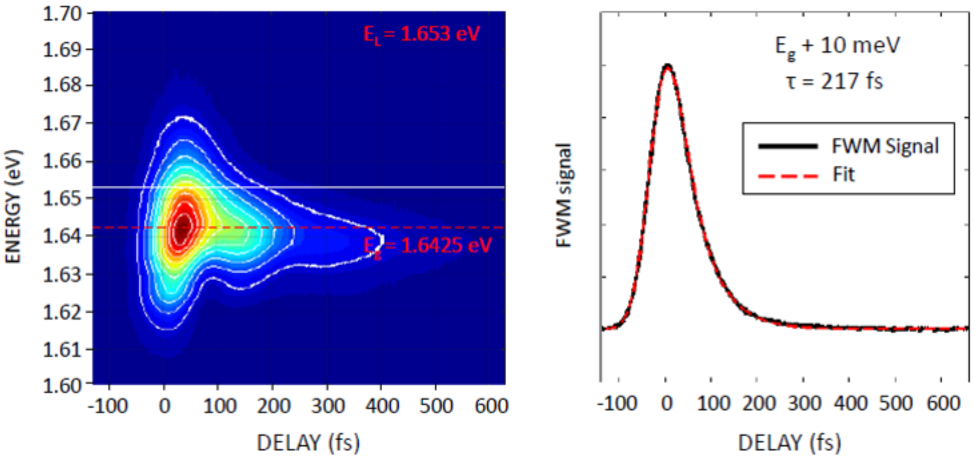

Figure 5.9: (Left) Results of four-wave mixing experiments on $CH_3NH_3PbI_3$ at 10 K, showing the amplitude of the signal (contour scale) as a function of energy and interpulse delay. The horizontal dashed red line illustrates the band gap and the white line shows the detection energy used to extract the dephasing time (10 meV above band gap). (Right) Delay dependence of FWM signal at 1.653 eV (solid black curve) with fit to Eq. 5.1 (red dashed curve).

Chapter 6

Ultrafast acoustic phonon scattering in $CH_3NH_3PbI_3$

Authors: Samuel A. March[1], Drew B. Riley[1],Charlotte Clegg[1], Daniel Webber[1], Ian G. Hill[1], Zhi-Gang Yu[2], Kimberley C. Hall[1]

[1]Department of Physics and Atmospheric Science, Dalhousie University, Halifax, Nova Scotia B3H4R2, Canada

[2]Washington State University, Spokane, Washington 99210 United States

Submitted for publication in Applied Physics Letters.

Kimberley C. Hall, and Murat Yildirim developed the four-wave mixing techniques. Samuel March performed the four-wave mixing experiments, the data analysis, linear absorption and SEM sample characterization. Daniel Webber designed and built part of the apparatus. The thin-films of MAPI were prepared and characterized using XRD by Charlotte Clegg at Dalhousie under the supervision of Prof. Ian Hill. Kimberley C. Hall and Samuel March conceived and designed the experiments. Zhi Gang Yu developed the theoretical model. Samuel March and Kimberley C. Hall wrote the manuscript with input from all authors.

Electron-phonon coupling plays a crucial role in carrier dynamics and charge transport in optoelectronic systems. The electron-phonon coupling in MAPI perovskite has been a topic of debate in recent years due in part to the complexity of fitting perovskite into standard scattering models. Here we use coherent spectroscopy to study the dominant electron-phonon scattering processes in the low temperature phase and model the dephasing signal to find clues regarding the fastest scattering processes. We find that the electron-phonon coupling is dominated by ultrafast acoustic phonon carrier scattering, and identify the Rashba effect as a potential mechanism that leads to an increase in electron-phonon interactions.

6.1 Abstract

The hybrid organic-inorganic perovskites are of great interest for applications in spintronics owing to the colossal Rashba effect in these materials. This Rashba coupling strongly modifies the dispersion relation, leading to an indirect band gap and a mixing of the spin and momentum degrees of freedom. These features of the Rashba spin-split band structure are expected to have a marked impact on carrier energy relaxation and transport in these materials. Using four-wave mixing spectroscopy, we reveal an ultrafast acoustic phonon scattering time of 110 fs. Our simulations show that the Rashba effect results in a six-fold increase in the low-temperature scattering rate over that expected from a simple parabolic band. Carrier scattering with ionized impurities dominates below 30 K, with an estimated impurity density from the measured scattering time of 1.7×10^{17} cm^{-3}. Our simulations yield a Rashba parameter of $\gamma_c = 2$ eVÅ, likely dominated by symmetry breaking at surfaces and interfaces in our solution-processed films.

6.2 Introduction

With the recent observation of a colossal Rashba Effect (RE) in $CH_3NH_3PbBr_3$ [147] with a magnitude comparable to the record set in BeTeI [148], the family of hybrid organic-inorganic perovskites have emerged as promising materials for semiconductor spintronics [97]. The RE results from the breaking of inversion symmetry in conjunction with spin-orbit coupling [103, 104], which is large in the hybrid perovskites owing to the incorporation of heavy elements (Pb, I, Br). This results in a lifting of the degeneracy of the spin states and provides a means to manipulate carrier spin without the need for external magnetic fields [149–151]. The ground-breaking observation in $CH_3NH_3PbBr_3$ using angle-resolved photoemission spectroscopy [147] has stimulated the search for experimental evidence of the RE in other hybrid perovskite materials using a variety of techniques, including photoluminescence [152, 153] electro-absorption [154], precessional spin relaxation [155], transient polarization anisotropy [156], and the circular photogalvanic effect [157]. While the origins of symmetry breaking in the various phases of the hybrid perovskites have received considerable theoretical attention in recent years [106, 110, 158–167], the observation of a large Rashba spin splitting in a range of HOIPs including thin film samples prepared under a variety of conditions is promising for the prospect of developing spintronic devices using these materials [149–151, 168–173].

For the application of HOIPs in spintronics and the optimization of other optoelectronic devices using these materials including photovoltaics [5], detectors [174], and optical sources [9, 175–177], it is essential to understand the impact of the colossal RE on carrier relaxation and transport. The splitting tied to the RE shifts the band edges away from the high symmetry point in the corresponding inversion symmetric structure. This leads to an indirect band gap separated from the direct gap by a relatively small energy (∼50 meV) [55, 153], a feature that has been invoked to explain the simultaneous presence of a large absorption coefficient and long carrier recombination time in $CH_3NH_3PbI_3$ leading to high solar cell efficiencies [110, 112, 160, 161, 164, 178, 179]. Much less is known about the effect of Rashba coupling on the dominant scattering processes in HOIPs [180], despite the crucial role played by these scattering processes in the operation of optoelectronic devices. The Rashba band edge dispersion relation and the mixing of the momentum and spin degrees of freedom are expected to strongly impact these scattering processes [99].

Here we report temperature-dependent four-wave mixing (FWM) studies on a thin film of $CH_3NH_3PbI_3$. Four-wave mixing in the self-diffraction geometry probes the time scale for the decay of quantum coherence in the electron-hole system, providing access to the dominant scattering processes for charge carriers [47–49]. Our findings reveal an ultrafast acoustic phonon scattering time of 110 fs. We show that this rapid scattering time is caused by the change of the density of states near the band edge induced by the RE [112]. Simulations of the temperature-dependent dephasing rate provide quantitative agreement with the measured four-wave mixing results. Our calculations indicate a Rashba coupling strength of $\gamma_c = 2$ eVÅ, attributed to the inversion symmetry breaking tied to the surfaces and interfaces in our solution processed film [164, 165, 181]. Our experiments also reveal an important role played by carrier scattering with ionized impurities, which dominates for temperatures below 30 K. Our experiments enable the extraction of an upper bound on the impurity density of 1.7×10^{17} cm^{-3}. Our findings provide insight into the impact of strong Rashba coupling on the fundamental carrier scattering processes in the hybrid perovskite family of materials.

The Rashba effect originates from spin-orbit coupling together with a lack of inversion symmetry. The Hamiltonian of the conduction band at a given momentum $k = (k_\perp \cos\phi, k_\perp \sin\phi, k_z)$, in the presence of the Rashba effect, reads

$$H_{\mathrm{c}} = E_{\mathrm{c}}^0 + \frac{\hbar^2}{2m_e}(k_\perp^2 + k_z^2) + \gamma_c(k_y\sigma_x - k_x\sigma_y), \tag{6.1}$$

where m_e is the effective mass, $k_\perp = \sqrt{k_x^2 + k_y^2}$, and $\sigma_{x(y)}$ are Pauli matrices. The energy-momentum dispersion of the above Hamiltonian is

$$E_k^\pm = \frac{\hbar^2}{2m_e}[(k_\perp \pm k_0)^2 + k_z^2], \tag{6.2}$$

where $k_0 = m\gamma_c/\hbar^2$ and $E_{\mathrm{c}}^0 - \frac{\hbar^2 k_0^2}{2m_e} \equiv 0$. The corresponding eigenfunctions for $E_k^\pm$ in the spin space are $|\psi_\pm(k)\rangle = \frac{1}{\sqrt{2}}(1, \pm i e^{i\phi})^T$ with the spin orientation being a function of the momentum direction. A schematic representation of the spin-split states in the conduction band is shown in Fig. 6.1**a**.

Due to the large RE in the HOIPs [147, 152–157], the form of the dispersion relation in Eq. (2) is expected to have a strong impact on carrier scattering and relaxation. For instance, the displacement of the band minimum to k_0 leads to a weakly indirect band gap, evidence for which has been observed experimentally in polycrystalline thin films of $CH_3NH_3PbI_3$ using photoluminescence techniques [55, 153]. The indirect band gap caused by the RE has been invoked to explain the unexpectedly long recombination times in the HOIPs despite their large band edge absorption [110, 112, 160, 161, 164, 178, 179]. As we show below, the modification of the density of states near the band edge tied to the RE also leads to a marked increase in the rate of acoustic phonon scattering.

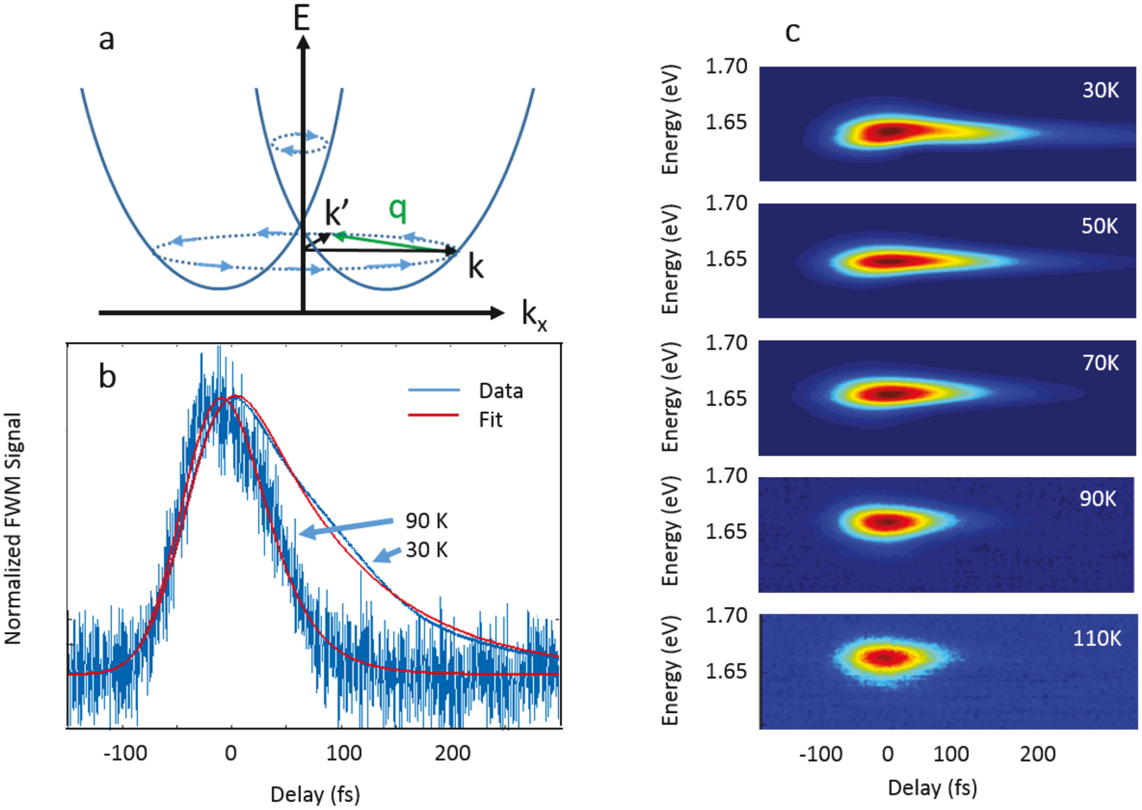

Figure 6.1: **a** Schematic electron dispersion relation in the presence of Rashba coupling. Light blue arrows indicate the direction of the Rashba effective magnetic field as a function of in-plane wavevector, representing the equilibrium spin texture for each spin band. An elastic scattering event with an acoustic phonon of wavevector $\vec{q}$ (green arrow) in the lower spin band is indicated schematically. **b** Four-wave mixing signal for two different temperatures (blue curves), together with fits to a photon echo (red curves), yielding values of $T_2 = (400 \pm 10)$ fs [(125 $\pm$ 10 fs)] for 30 K [90 K]. The laser pulse fluence was 1.3 μJ/cm^2 and the laser was tuned to 1.65 eV, exciting optical transitions near the band edge. **c** Four-wave mixing signal versus interpulse delay and detection photon energy for various temperatures. The signal decays more rapidly at higher temperature.

The carrier scattering processes were studied in a thin film of $CH_3NH_3PbI_3$ using FWM in the two pulse self-diffraction geometry. [47] The thin films were prepared using a sequential deposition procedure described previously [48, 49, 118]. In the FWM technique, two laser pulses $\vec{E_1}(t)$ and $\vec{E_2}(t-\tau)$ propagating with wave vectors $\vec{k_1}$ and $\vec{k_2}$ are used to excite the sample. The decay of the so-called "“self-diffraction”" signal along $2\vec{k_2}-\vec{k_1}$ versus interpulse delay τ indicates the time for loss of coherence on the optical transitions in the sample. Since the scattering of either carrier type (electron or hole) changes the phase of the oscillating dipole on the electron-hole pair transition, this technique provides a sensitive probe of the fastest scattering process involving charge carriers.

6.3 Results and Discussion

The results of FWM experiments are shown for two different temperatures in Fig. 6.1**b**. The FWM signal was fit to a photon echo response [62] convoluted with the laser pulse duration (55 fs) to obtain the interband dephasing time (T_2) at each temperature. The corresponding fits are indicated by the red curves in Fig. 6.1**b**. The spectrally-resolved FWM signal is shown for a range of temperatures in Fig. 6.1**c**. The weak oscillations in the results for 30 K are tied to excitonic quantum beats, as discussed previously [48]. These quantum beats disappear and the FWM signal decays more rapidly as the temperature increases, reflecting faster carrier scattering at higher temperatures. The FWM signal decay time was below the resolution of our experiments for temperatures above 110 K. The dephasing rate ($\frac{1}{T_2}$) extracted from fits to the FWM signal is shown in Fig. 6.2**a** as a function of temperature and detection photon energy. $\frac{1}{T_2}$ increases with increasing carrier energy relative to the band gap, depends weakly on temperature below 30 K and increases rapidly for higher temperatures.

The relatively constant dephasing rate below 30 K in Fig. 6.2**a** is attributed to scattering with ionized impurities. The rate of ionized impurity scattering may be obtained from the analysis of Conwell and Weisskopf [182] modified to describe interband dephasing rather than momentum relaxation. (The latter contains a directional factor $1-\cos\theta$ with θ being the scattering angle; i.e., a forward scattering

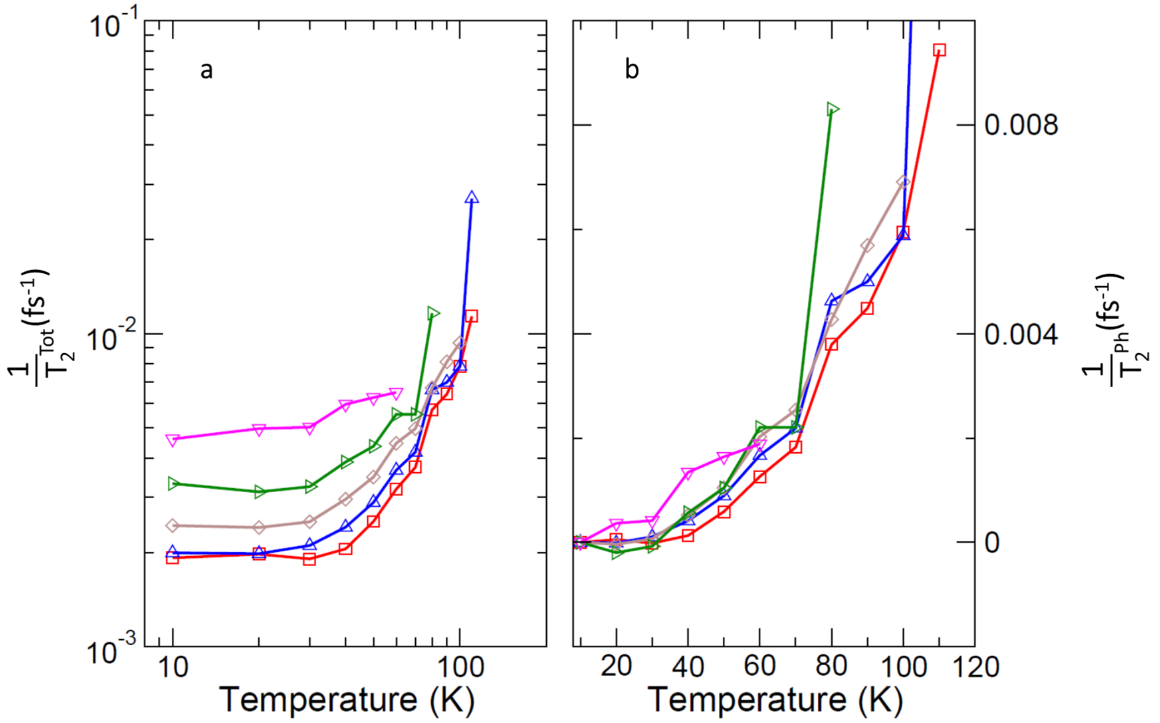

Figure 6.2: **a** The interband dephasing rate $\frac{1}{T_2}$ obtained from fits to the four-wave mixing signal (symbols). Pink, green, brown, blue and red symbols correspond to optical detection energies of -10, -5, 0, 5, and 10 meV with respect to the band gap. **b** Same data as in **a** after subtraction of the dephasing rate at 10 K, attributed to scattering with ionized impurities. The resulting data is the dephasing rate tied to scattering with phonons, which is nearly independent of carrier energy in the vicinity of the band edge.

does not impact the momentum relaxation time, but does reduce T_2.) The resulting dephasing rate may be expressed as $\tau_I^{-1} = \frac{\pi}{4} N_I^{1/3} v$, where N_I is the density of ionzied impurities and $v = \sqrt{\frac{2E_k}{m}}$ is the carrier velocity and E_k the kinetic energy. The rate of ionized impurity scattering is independent of temperature and increases with E_k. Using the measured dephasing rate at 10 K, we estimate the density of ionized impurities to be 1.7×10^{17}cm^{-3}.

If we subtract the 10 K dephasing rate from the measured results at each value of E_k, the residual dephasing rate (Fig. 6.2**b**) accounts for all other carrier scattering processes. Given the strong increase in the dephasing rate with temperature above 30 K, and the low rate of carrier-carrier scattering in $CH_3NH_3PbI_3$ at the excitation density used in these experiments (2×10^{16} cm^{-3}) [49], the residual dephasing process is attributed to carrier scattering with phonons. The overall rate of phonon scattering is faster than that expected for a simple parabolic band given known parameters for the phonon coupling strength and the value of the optical phonon energies [112, 180]. We show below that both the ultrafast scattering rate and the constant rate versus E_k are well described by acoustic phonon scattering taking into account the impact of the RE on the dispersion relation.

The interband dephasing rate due to carrier scattering with both acoustic phonons and polar optical phonons was calculated following a model developed previously [180]. The electron-phonon coupling can be expressed as

$$H_{\rm ep} = \sum_{kqs} (V_q b_q c^\dagger_{k+qs} c_{ks} + V_q^* b_q^\dagger c^\dagger_{ks} c_{k-qs}) \tag{6.3}$$

where $c^\dagger_{ks}$ creates an electron with momentum k and spin s $(=\uparrow,\downarrow)$, $b_q^\dagger$ creates a phonon with momentum q, and the two terms describe phonon absorption and emission processes, respectively. Since $H_{\rm ep}$ does not change electron spin, the matrix elements between electron eigenstates, $M_{\pm\pm}(k,k') \equiv \langle \psi_\pm(k') | H_{\rm ep} | \psi_\pm(k) \rangle$, in the presence of RE are

$$\begin{aligned} M_{++}(k,k') &= M_{--}(k,k') = V_{k'-k} \frac{1+e^{i(\phi'-\phi)}}{2}, && (6.4) \\ M_{+-}(k,k') &= M_{-+}(k,k') = V_{k'-k} \frac{1-e^{i(\phi'-\phi)}}{2}. && (6.5) \end{aligned}$$

The coupling between electrons and acoustic phonons is

$$V_q = iE_1 \left(\frac{\hbar}{2\rho\omega_q} \right)^{1/2} q \equiv iE_1 \left(\frac{\hbar v_s}{2c_L} \right)^{1/2} \sqrt{q} \tag{6.6}$$

where E_1 is the deformation potential coupling for the conduction band, ρ is the material density, $\omega_q = v_s q$ is the acoustic phonon dispersion with v_s being the velocity of sound in the material, and $c_L = \rho v_s^2$ is the longitudinal elastic constant. In HOIPs, the polar coupling for electrons can be expressed as

$$V_k = -i \sum_j \left(\frac{4\pi\alpha_{\mathrm{e}j}}{\Omega}\right)^{1/2} \frac{\hbar\omega_{l_j}}{q} \left(\frac{\hbar}{2m_{\mathrm{e}}\omega_{l_j}}\right)^{1/4} \tag{6.7}$$

where $\alpha_{\mathrm{e}j}$ is the dimensionless polar coupling strength for the jth optical phonon mode [180]. The scattering rate can be calculated from the Fermi's golden rule. In our calculations, we restrict ourselves to the scattering rate of electrons. As we show below, the RE strongly enhances the rate of acoustic phonon scattering. Since the magnitude of the RE in the valence band is expected to be weaker than in the conduction band due to the dominant contribution of the Iodide 5p orbital to the valence states [99], electron scattering is assumed to dominate the interband dephasing process. The magnitude of the Rashba coupling strength γ_c was taken as an adjustable parameter to obtain the best fit to the experimental results.

The results of theoretical simulations of the interband dephasing rate including scattering with acoustic and polar optical phonons is shown in Fig. 6.3**a**, together with the experimental data. For these simulations, only one optical phonon mode is included tied to the Pb-I stretching mode, which was shown previously to have the largest polar optical coupling ($\alpha_{\mathrm{e}} = 1.1$) with phonon energy $\hbar\omega_0 = 16.7$ meV [180], and the value of the Rashba coupling strength is $\gamma_c = 2$ eVÅ. The theoretical simulations provide good quantitative agreement with the experimental results, including both the temperature dependence and the lack of dependence of the scattering rate on carrier energy. The contribution of each phonon scattering process to the calculated dephasing rate at a temperature of 50 K is shown as a function of electron energy in Fig. 6.3**b**. The solid (dashed) curves indicate the scattering rates with (without) Rashba coupling. Acoustic phonon scattering dominates over polar optical phonon scattering for the full range of temperatures considered here ($\leq$110 K).

The rate of acoustic phonon scattering is strongly enhanced for electrons energies near the band edge with Rashba coupling included. This strong enhancement is the origin of the ultrafast interband dephasing observed in our experiments. Our

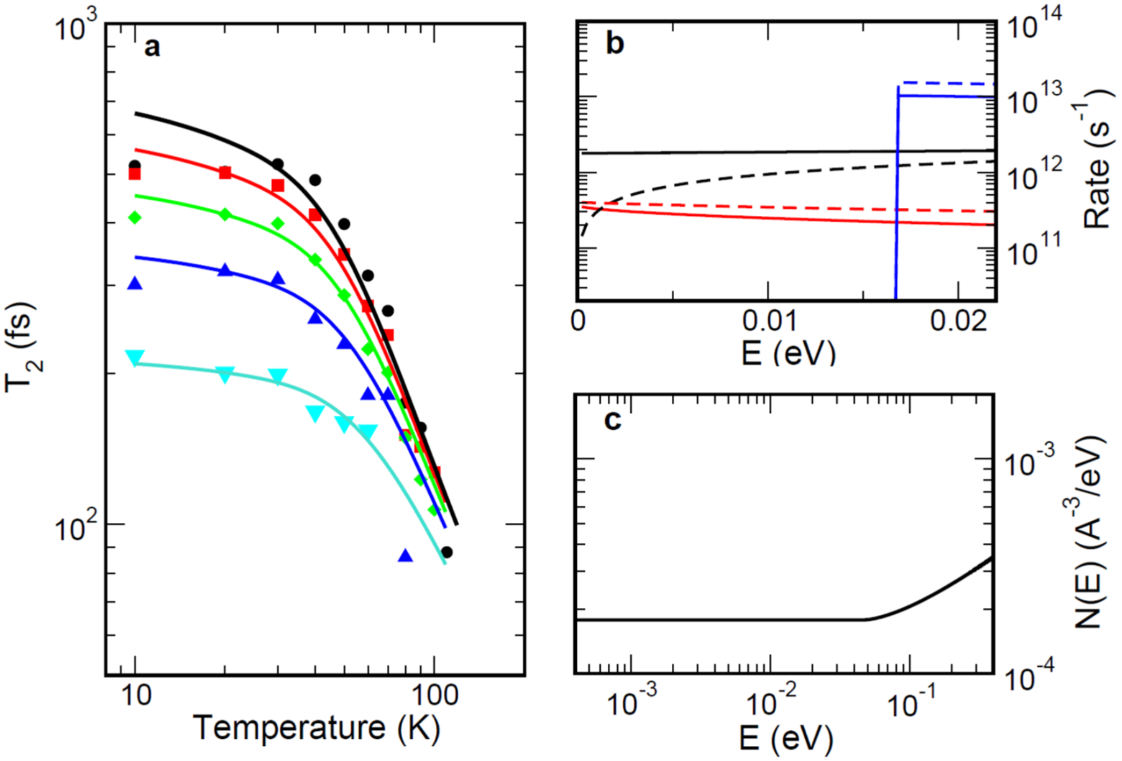

Figure 6.3: (a) Results of theoretical simulations of the interband dephasing times (solid curves). The experimental data (symbols) are the same as in Fig. 6.2a. (b) Calculated scattering rate as a function of electron energy tied to acoustic phonon scattering (black), and polar optical phonon scattering (red: phonon absorption; blue: phonon emission). Solid (dashed) curves show the results of calculations with (without) Rashba coupling, showing the strong enhancement of acoustic phonon scattering caused by the Rashba effect. (c) Calculated density of states in the conduction band including the Rashba splitting. The DOS is constant for electron energies below the onset of states involving the higher energy spin band, in contrast to the $\sqrt{E}$ dependence for a parabolic band without Rashba coupling.

calculations indicate an enhancement of the low temperature acoustic phonon scattering rate of 6× relative to the case of a simple parabolic band without Rashba coupling. The RE also modifies the energy-dependence of the scattering rate tied to acoustic phonons, which changes from an approximately square-root dependence without Rashba to constant with the RE included. This feature is tied to the constant density of states in the lower-energy spin band (Fig. 6.3**c**), and explains the lack of an observed dependence of the dephasing rate on carrier energy near the band gap. The $\sqrt{q}$ dependence of the acoustic phonon coupling strength also contributes to the enhancement of the scattering rate as the RE leads to an increase in the average $|q|$ for phonon scattering near the band minimum (Fig. 6.1**a**).

Since the $CH_3NH_3PbI_3$ sample we study here is a polycrystalline thin film, the RE we observe is likely dominated by inversion symmetry breaking at the surfaces and grain boundaries [164, 165, 181]. The surface reconstruction leads to a redistribution of the conduction and valence states, resulting in a strong surface dipole [165] that has a penetration depth comparable to the film thickness (265 nm) [181]. The value of $\gamma_c = 2$ eVÅ we extract from our simulations is in good agreement with a recent calculation of the surface RE using density functional theory [164] as well as recent observations in $CH_3NH_3PbI_3$ films in the orthorhomic phase using the circular photogalvanic effect [157].

6.4 Conclusions

In conclusion, we have applied four-wave mixing to measure electron scattering times in thin films of $CH_3NH_3PbI_3$. Our results indicate that the strong Rashba coupling in this system enhances the rate of acoustic phonon scattering for band edge carriers, by a factor of 6 at low temperature, due to the constant density of states in the lower spin subband. The resulting acoustic phonon scattering time is 110 fs at 110 K. Our simulations give quantitative agreement with the measured dependence of the interband dephasing time on temperature and carrier kinetic energy with a Rashba coupling strength of $\gamma_c = 2$ eVÅ, believed to be dominated by inversion symmetry breaking at surfaces and interfaces in the polycrystalline thin film. The large strength of the Rashba effect we observe, which is in line with other recent experiments in the HOIPs [147, 152–157], is promising for the prospect of developing spintronic devices using these materials. Our experiments also indicate that scattering with ionized impurities dominates for temperatures below 30 K, with an estimated density of 1.7×10^{17} cm^{-3}. Our findings provide insight into the influence of the strong Rashba effect in the HOIPs on carrier relaxation and transport, with implications for a wide range of device applications.

6.5 Acknowledgements

This research is supported by the Natural Sciences and Engineering Research Council of Canada. Work at Washington State University was supported by grant W911NF-17-1-0511 from the US Army Research Office.

Chapter 7

Conclusion

Perovskite photovoltaic materials have gained critical acclaim worldwide as a potential solution to our growing demand for clean and renewable energy. As an alternative to fossil-fuel based energy production technologies, the advantages of perovskite photovoltaics are obvious. Compared to existing PV technologies, perovskite has the advantage that it can achieve high efficiencies from low temperature, low-cost manufacturing techniques. Existing photovoltaics technologies including crystalline and thin-film technologies require high temperature, high cost manufacturing processes to achieve high crystal purity, and high efficiencies. Another advantage is that perovskite is deposited from solution, meaning it can be deposited on a variety of different substrates and can be building integrated as a thin-film on facades or as a coating on windows. The high efficiency resulting from an ideal combination of a large absorption coefficient and long carrier lifetimes is surprising as perovskite is manufactured using low-temperature manufacturing processes resulting in a highly defected crystal structure. The fundamental material properties that lead to these ideal device properties has remained a mystery. This thesis has advanced the fundamental understanding of the material properties of MAPI by utilizing coherent spectroscopy techniques that study the fastest scattering processes in semiconductor systems. This thesis work encompasses the direct measurement of the exciton binding energy, showed that many-body interactions are weaker in perovskite than GaAs, and illuminates the effect of the Rashba spin splitting on carrier-phonon scattering in MAPI perovskite thin-films.

The exciton binding energy is a crucial material parameter that dictates the mode of transport in the PV device. If the exciton binding energy is significantly larger than the thermal energy at device operating temperature ($k_B T$), transport is dictated by the conduction of Coulombically bound electron-hole pairs. If the exciton binding energy is on the order of $k_B T$, transport is dictated by the conduction of free electrons and holes. We used FWM coherent spectroscopy that is sensitive to exciton resonances to directly, and simultaneously measure the binding energy of free excitons, and excitons localized by shallow defect states in the low temperature orthorhombic phase of MAPI. We found that the exciton binding energy for free (defect-bound) excitons was 13 meV (29 meV). Our measurements clarified an ongoing debate regarding the binding energy with reported values that ranged from 2-50 meV and were attained using incoherent optical techniques.

This thesis also reported a study that provided valuable context as to whether the fundamental material properties of perovskite resemble those of inorganic semiconductors. We measured the carrier density dependent scattering of free-carriers at carrier densities on the order of those typical in operating photovoltaic devices using FWM coherent spectroscopy. Our results indicate that scattering resulting from many-body interactions are weak in the MAPI perovskite system compared to the well known inorganic semiconductor GaAs, revealing a stark contrast between perovskite and inorganic semiconductors irrespective of the GaAs defect density. We proposed that dynamic disorder inherent to the MAPI system due to the organic constituents could lead to carrier localization and weak many-body interactions. This effect would have no corollary in inorganic systems.

This thesis work also encompassed the measurement of carrier-phonon scattering times by analyzing the temperature, and energy dependent dephasing time in the MAPI system using FWM coherent spectroscopy at low temperatures (10-100 K). These experiments showed that the phonon scattering time is extremely rapid. In collaboration with Zhi Gang Yu at Washington State University, a model was developed that indicates that acoustic phonon scattering dominates dephasing, with a scattering time of 110 fs at 110 K. The comparison between the experimental results and the theoretical simulations also revealed the important role that Rashba band-splitting plays in enhancing acoustic phonon scattering.

FWM offers the ability to probe carrier scattering at low carrier densities ($< 10^{16} cm^{-3}$). In probing this low carrier density regime, our studies strongly contrast with ultrafast experiments by other research groups [50,133,183]. For example Deschler et al. reported the measurement of T_2 times in perovskite at densities greater than $10^{19} cm^{-3}$ [50]. Their experiments revealed a carrier density dependent T_2

time. In this much higher carrier density regime, a nonzero density dependence is expected because of the influence of screening of the charge carriers. In the room temperature experiments of Deschler et al, the high carrier density would screen put the coupling responsible for polaron formation. Such screening effects would also be apparent in pump probe experiments at densities of greater than $10^{19} cm^{-3}$, explaining the band gap renormalization that has been observed in the past at these densities [133]. By probing carrier scattering at densitites comparable to the operating conditions of solar cells, our experiments provide an important contribution to unraveling the fundamental properties relevant for solar cell operation.

A valuable extension of the present thesis work would be to apply FWM to other perovskite systems including single-crystal and two-dimensional perovskite. Two-dimensional perovskites offer enhanced tunability by controlling the thickness of the octahedral layers which controls the degree of quantum confinement. In addition, these materials offer flexibility in the choice of organic spacer molecules that play the role of insulating barriers between the lead-iodide octahedral sheets in which the charge carriers are confined. Recent experiments suggest that the coupling between the charge carriers and the phonon modes tied to the organic constituents is very strong [51]. It would therefore be of value to see if polaronic effects play a similar role in reducing coupling between charge carriers in these 2D perovskites. Measuring the dephasing time in these novel systems at low carrier densities will clarify the fundamental optoelectronic properties in these systems, as these measurements do not exist in the literature to date.

Furthermore, the experiments utilized in these studies were limited by the finite tuning range and pulse duration of the laser system (50 fs, 750 nm - 850 nm). In order to study the full range of carrier dephasing dynamics above and below the optical bandgap (as a function of temperature) shorter wavelength, and shorter temporal duration pulses can be utilized. As well, bi-exciton resonances can be probed using a variety of coherent spectroscopy techniques including 2DFTS (2D-perovskite), and FWM (3D-perovskite). Such studies would provide further insight into the role of Coulomb coupling in perovskite systems.

The work presented in this thesis builds upon the onslaught of experimental work reported in the literature over the past 5 years of intense research, and advances the current understanding of the fundamental properties of perovskite. This work should promote further development of perovskite based photovoltaic technology, resulting from a clarified understanding of the role of Coulomb coupling between carriers, and the material environment that they interact in.

Bibliography

[1] “Renewables 2017,” tech. rep., International Energy Agency, 2018.

[2] “2018 Snapshot of Global Photovoltaic Markets,” tech. rep., International Energy Agency, 2018.

[3] “Photovoltaics Report,” tech. rep., Fraunhofer ISE, 2018.

[4] J. Gong, S. B. Darling, and F. You, “Perovskite photovoltaics: Life-cycle assessment of energy and environmental impacts,” *Energy and Environmental Science*, vol. 8, no. 7, pp. 1953–1968, 2015.

[5] NREL, “Best Research-Cell Efficiencies,” 2017.

[6] P. Gao, M. Gratzel, and M. K. Nazeeruddin, “Organohalide Lead Perovskites for Photovoltaic Applications,” *Energy & Environmental Science*, vol. 7, no. c, pp. 2448–2463, 2014.

[7] W. Zhang, G. E. Eperon, and H. J. Snaith, “Metal halide perovskites for energy applications,” *Nature Energy*, vol. 1, no. 6, 2016.

[8] R. Dong, Y. Fang, J. Chae, J. Dai, Z. Xiao, Q. Dong, Y. Yuan, A. Centrone, X. C. Zeng, and J. Huang, “High-Gain and Low-Driving-Voltage Photodetectors Based on Organolead Triiodide Perovskites,” *Advanced Materials*, vol. 27, no. 11, pp. 1912–1918, 2015.

[9] H. Zhu, Y. Fu, F. Meng, X. Wu, Z. Gong, Q. Ding, M. V. Gustafsson, M. T. Trinh, S. Jin, and X. Y. Zhu, “Lead halide perovskite nanowire lasers with low lasing thresholds and high quality factors,” *Nature Materials*, vol. 14, no. 6, pp. 636–642, 2015.

[10] N. G. Park, “Organometal Perovskite Light Absorbers Toward a 20% Efficiency Low-Cost Solid-State Mesoscopic Solar Cell,” *Journal of Physical Chemistry Letters*, vol. 4, no. 15, pp. 2423–2429, 2013.

[11] S. D. Stranks, G. E. Eperon, G. Grancini, C. Menelaou, M. J. P. Alcocer, T. Leijtens, L. M. Herz, A. Petrozza, and H. J. Snaith, “Electron-Hole Diffusion Lengths Exceeding 1 Micrometer in an Organometal Trihalide Perovskite Absorber,” *Science*, vol. 342, pp. 341–345, 2013.

[12] S. De Wolf, J. Holovsky, S.-J. Moon, P. Löper, B. Niesen, M. Ledinsky, F.-J. Haug, J.-H. Yum, and C. Ballif, “Organometallic halide perovskites: Sharp optical absorption edge and its relation to photovoltaic performance,” *Journal of Physical Chemistry Letters*, vol. 5, pp. 1035–1039, 2014.

[13] K. Wu, A. Bera, C. Ma, Y. Du, Y. Yang, L. Li, and T. Wu, "Temperature-dependent excitonic photoluminescence of hybrid organometal halide perovskite films," *Phys. Chem. Chem. Phys.*, vol. 16, no. 41, pp. 22476–22481, 2014.

[14] T. J. Savenije, C. S. Ponseca, L. Kunneman, M. Abdellah, K. Zheng, Y. Tian, Q. Zhu, S. E. Canton, I. G. Scheblykin, T. Pullerits, A. Yartsev, and V. Sundström, "Thermally activated exciton dissociation and recombination control the carrier dynamics in organometal halide perovskite," *Journal of Physical Chemistry Letters*, vol. 5, pp. 2189–2194, 2014.

[15] S. Sun, T. Salim, N. Mathews, M. Duchamp, C. Boothroyd, G. Xing, C. Sum, Tze, and Y. M. Lam, "The origin of high efficiency in low-temperature solution-processable bilayer organometal halide hybrid solar cells," *Energy and Environmental Science*, vol. 7, pp. 399–407, 2014.

[16] H. He, Q. Yu, H. Li, J. Li, J. Si, Y. Jin, N. Wang, J. Wang, J. He, X. Wang, Y. Zhang, and Z. Ye, "Exciton localization in solution-processed organolead trihalide perovskites," *Nature Communications*, vol. 7, p. 10896, 2016.

[17] C. Wehrenfennig, M. Liu, H. J. Snaith, M. B. Johnston, and L. M. Herz, "Charge carrier recombination channels in the low-temperature phase of organic-inorganic lead halide perovskite thin films," *APL Materials*, vol. 2, p. 081513, 2014.

[18] A. Miyata, A. Mitioglu, P. Plochocka, O. Portugall, J. T.-W. Wang, S. D. Stranks, H. J. Snaith, and R. J. Nicholas, "Direct measurement of the exciton binding energy and effective masses for charge carriers in organic–inorganic tri-halide perovskites," *Nature Physics*, vol. 11, pp. 582–588, 2015.

[19] K. Galkowski, A. Mitioglu, A. Miyata, P. Plochocka, O. Portugall, G. E. Eperon, J. T.-W. Wang, T. Stergiopoulos, S. D. Stranks, H. Snaith, and R. J. Nicholas, "Determination of the exciton binding energy and effective masses for methylammonium and formamidinium lead tri-halide perovskite semiconductors," *Energy Environ. Sci.*, vol. 9, pp. 962–970, 2016.

[20] Q. Lin, A. Armin, R. Nagiri, Ravi, Chandra, P. L. Burn, and P. Meredith, "Electro-optics of perovskite solar cells," *Nature Photonics*, vol. 9, no. 2, pp. 106–112, 2014.

[21] M. Saba, M. Cadelano, D. Marongiu, F. Chen, V. Sarritzu, N. Sestu, C. Figus, M. Aresti, R. Piras, A. Geddo Lehmann, C. Cannas, A. Musinu, F. Quochi, A. Mura, and G. Bongiovanni, "Correlated electron-hole plasma in organometal perovskites.," *Nature communications*, vol. 5, no. May, p. 5049, 2014.

[22] J. Even, L. Pedesseau, and C. Katan, "Analysis of multivalley and multibandgap absorption and enhancement of free carriers related to exciton screening in hybrid perovskites," *Journal of Physical Chemistry C*, vol. 118, no. 22, pp. 11566–11572, 2014.

[23] V. D'Innocenzo, G. Grancini, M. J. P. Alcocer, A. R. S. Kandada, S. D. Stranks, M. M. Lee, G. Lanzani, H. J. Snaith, and A. Petrozza, "Excitons versus free charges in organo-lead tri-halide perovskites.," *Nature communications*, vol. 5, p. 3586, 2014.

[24] Y. Yamada, T. Nakamura, M. Endo, A. Wakamiya, and Y. Kanemitsu, "Photoelectronic Responses in Solution-Processed Perovskite CH3NH3PbI3 Solar Cells Studied by Photoluminescence and Photoabsorption Spectroscopy," *IEEE Journal of Photovoltaics*, vol. 5, no. 1, pp. 401–405, 2015.

[25] N. Sestu, M. Cadelano, V. Sarritzu, F. Chen, D. Marongiu, R. Piras, M. Mainas, F. Quochi, M. Saba, A. Mura, and G. Bongiovanni, "Absorption F-Sum Rule for the Exciton Binding Energy in Methylammonium Lead Halide Perovskites," *Journal of Physical Chemistry Letters*, vol. 6, no. 22, pp. 4566–4572, 2015.

[26] A. M. Soufiani, F. Huang, P. Reece, R. Sheng, A. Ho-Baillie, and M. A. Green, "Polaronic exciton binding energy in iodide and bromide organic-inorganic lead halide perovskites," *Applied Physics Letters*, vol. 107, no. 23, 2015.

[27] D. A. Valverde-Chávez, C. S. Ponseca, C. C. Stoumpos, A. Yartsev, M. G. Kanatzidis, V. Sundström, and D. G. Cooke, "Intrinsic femtosecond charge generation dynamics in single crystal CH 3 NH 3 PbI 3," *Energy Environ. Sci.*, vol. 8, no. 12, pp. 3700–3707, 2015.

[28] Y. Yamada, T. Nakamura, M. Endo, A. Wakamiya, and Y. Kanemitsu, "Near-band-edge optical responses of solution-processed organic–inorganic hybrid perovskite CH3NH3PbI3 on mesoporous TiO2 electrodes," *Applied Physics Express*, vol. 7, no. 3, p. 032302, 2014.

[29] H. H. Fang, R. Raissa, M. Abdu-Aguye, S. Adjokatse, G. R. Blake, J. Even, and M. A. Loi, "Photophysics of organic-inorganic hybrid lead iodide perovskite single crystals," *Advanced Functional Materials*, vol. 25, no. 16, pp. 2378–2385, 2015.

[30] L. Y. Huang and W. R. L. Lambrecht, "Electronic band structure, phonons, and exciton binding energies of halide perovskites CsSnCl3, CsSnBr3, and CsSnI3," *Physical Review B - Condensed Matter and Materials Physics*, vol. 88, p. 165203, 2013.

[31] H. Tahara, M. Endo, A. Wakamiya, and Y. Kanemitsu, "Experimental Evidence of Localized Shallow States in Orthorhombic Phase of

CH3NH3PbI3Perovskite Thin Films Revealed by Photocurrent Beat Spectroscopy," *Journal of Physical Chemistry C*, vol. 120, no. 10, pp. 5347–5352, 2016.

[32] K. Tanaka, T. Takahashi, T. Ban, T. Kondo, K. Uchida, and N. Miura, "Comparative study on the excitons in lead-halide-based perovskite-type crystals CH3NH3PbBr3 CH3NH3PbI3," *Solid State Communications*, vol. 127, pp. 619–623, 2003.

[33] M. Hirasawa, T. Ishihara, T. Goto, K. Uchida, and N. Miura, "Magnetoabsorption of the lowest exciton in perovskite-type compound (CH3NH3)PbI3," *Physica B: Physics of Condensed Matter*, vol. 201, no. C, pp. 427–430, 1994.

[34] D. P. McMeekin, G. Sadoughi, W. Rehman, G. E. Eperon, M. Saliba, M. T. Horantner, A. Haghighirad, N. Sakai, L. Korte, B. Rech, M. B. Johnston, L. M. Herz, and H. J. Snaith, "A mixed-cation lead mixed-halide perovskite absorber for tandem solar cells," *Science*, vol. 351, no. 6269, pp. 151–155, 2016.

[35] R. E. Beal, D. J. Slotcavage, T. Leijtens, A. R. Bowring, R. A. Belisle, W. H. Nguyen, G. F. Burkhard, E. T. Hoke, and M. D. McGehee, "Cesium Lead Halide Perovskites with Improved Stability for Tandem Solar Cells," *Journal of Physical Chemistry Letters*, vol. 7, no. 5, pp. 746–751, 2016.

[36] F. Hao, C. C. Stoumpos, D. H. Cao, R. P. H. Chang, and M. G. Kanatzidis, "Lead-free solid-state organic–inorganic halide perovskite solar cells," *Nature Photonics*, vol. 8, no. 6, pp. 489–494, 2014.

[37] B. Saparov, F. Hong, J. P. Sun, H. S. Duan, W. Meng, S. Cameron, I. G. Hill, Y. Yan, and D. B. Mitzi, "Thin-Film Preparation and Characterization of Cs3Sb2I9: A Lead-Free Layered Perovskite Semiconductor," *Chemistry of Materials*, vol. 27, no. 16, pp. 5622–5632, 2015.

[38] F. Hong, B. Saparov, W. Meng, Z. Xiao, D. B. Mitzi, and Y. Yan, "Viability of Lead-Free Perovskites with Mixed Chalcogen and Halogen Anions for Photovoltaic Applications," *Journal of Physical Chemistry C*, vol. 120, no. 12, pp. 6435–6441, 2016.

[39] D. H. Cao, C. C. Stoumpos, O. K. Farha, J. T. Hupp, and M. G. Kanatzidis, "2D Homologous Perovskites as Light-Absorbing Materials for Solar Cell Applications," *Journal of the American Chemical Society*, vol. 137, no. 24, pp. 7843–7850, 2015.

[40] Y. Kim, E. Yassitepe, O. Voznyy, R. Comin, G. Walters, X. Gong, P. Kanjanaboos, A. F. Nogueira, and E. H. Sargent, "Efficient Luminescence from Perovskite Quantum Dot Solids," *ACS Applied Materials and Interfaces*, vol. 7, no. 45, pp. 25007–25013, 2015.

[41] D. Zhang, S. W. Eaton, Y. Yu, L. Dou, and P. Yang, “Solution-Phase Synthesis of Cesium Lead Halide Perovskite Nanowires,” *Journal of the American Chemical Society*, vol. 137, no. 29, pp. 9230–9233, 2015.

[42] Y. Bekenstein, B. A. Koscher, S. W. Eaton, P. Yang, and A. P. Alivisatos, “Highly Luminescent Colloidal Nanoplates of Perovskite Cesium Lead Halide and Their Oriented Assemblies,” *Journal of the American Chemical Society*, vol. 137, no. 51, pp. 16008–16011, 2015.

[43] Y. Fu, F. Meng, M. B. Rowley, B. J. Thompson, M. J. Shearer, D. Ma, R. J. Hamers, J. C. Wright, and S. Jin, “Solution growth of single crystal methylammonium lead halide perovskite nanostructures for optoelectronic and photovoltaic applications,” *Journal of the American Chemical Society*, vol. 137, no. 17, pp. 5810–5818, 2015.

[44] Y. Zhang, J. Liu, Z. Wang, Y. Xue, Q. Ou, L. Polavarapu, J. Zheng, X. Qi, and Q. Bao, “Synthesis, properties, and optical applications of low-dimensional perovskites,” *Chem. Commun.*, vol. 52, no. 94, pp. 13637–13655, 2016.

[45] L. M. Herz, “Charge-Carrier Dynamics in Organic-Inorganic Metal Halide Perovskites,” *Annual Review of Physical Chemistry*, vol. 67, no. 1, pp. 65–89, 2016.

[46] T. C. Sum and N. Mathews, “Advancements in perovskite solar cells: photophysics behind the photovoltaics,” *Energy Environ. Sci.*, vol. 7, no. 8, pp. 2518–2534, 2014.

[47] J. Shah, *Ultrafast Spectroscopy of Semiconductors and Semiconductor Nanostructures*. Springer-Verlag, 1996.

[48] S. A. March, C. Clegg, D. B. Riley, D. Webber, I. G. Hill, and K. C. Hall, “Simultaneous observation of free and defect-bound excitons in CH3NH3PbI3 using four-wave mixing spectroscopy,” *Scientific Reports*, vol. 6, p. 39139, 2016.

[49] S. A. March, D. B. Riley, C. Clegg, D. Webber, X. Liu, M. Dobrowolska, J. K. Furdyna, I. G. Hill, and K. C. Hall, “Four-Wave Mixing in Perovskite Photovoltaic Materials Reveals Long Dephasing Times and Weaker Many-Body Interactions than GaAs,” *ACS Photonics*, vol. 4, no. 6, pp. 1515–1521, 2017.

[50] J. M. Richter, F. Branchi, F. Valduga De Almeida Camargo, B. Zhao, R. H. Friend, G. Cerullo, and F. Deschler, “Ultrafast carrier thermalization in lead iodide perovskite probed with two-dimensional electronic spectroscopy,” *Nature Communications*, vol. 8, no. 1, pp. 1–7, 2017.

[51] F. Thouin, S. Neutzner, D. Cortecchia, V. A. Dragomir, C. Soci, T. Salim, Y. M. Lam, R. Leonelli, A. Petrozza, A. R. S. Kandada, and C. Silva, “Stable

biexcitons in two-dimensional metal-halide perovskites with strong dynamic lattice disorder," vol. 034001, pp. 1–10, 2017.

[52] J. Shi, Y. Li, Y. Li, D. Li, Y. Luo, H. Wu, and Q. Meng, "From Ultrafast to Ultraslow: Charge-Carrier Dynamics of Perovskite Solar Cells," *Joule*, vol. 2, no. 5, pp. 879–901, 2018.

[53] A. Kojima, K. Teshima, Y. Shirai, and T. Miyasaka, "Organometal halide perovskites as visible-light sensitizers for photovoltaic cells," *Journal of the American Chemical Society*, vol. 131, no. 17, pp. 6050–6051, 2009.

[54] M. Saliba, T. Matsui, K. Domanski, J. Seo, A. Ummadisingu, S. Zakeeruddin, J. Correa-Baena, W. Tress, A. Abate, A. Hagfeld, and M. Gratzel, "Incorporation of rubidium cations into perovskite solar cells improves photovoltaic performance," vol. 354, no. 6309, 2016.

[55] E. M. Hutter, M. C. Gélvez-Rueda, A. Osherov, V. Bulović, F. C. Grozema, S. D. Stranks, and T. J. Savenije, "Direct–indirect character of the bandgap in methylammonium lead iodide perovskite," *Nature Materials*, vol. 1, no. October, 2016.

[56] J. Even, "Pedestrian Guide to Symmetry Properties of the Reference Cubic Structure of 3D All-Inorganic and Hybrid Perovskites," *The Journal of Physical Chemistry Letters*, vol. 6, no. 12, pp. 2238–2242, 2015.

[57] J. C. Hwang, H. Temkin, T. M. Brennan, and R. E. Frahm, "Growth of high-purity GaAs layers by molecular beam epitaxy," *Applied Physics Letters*, vol. 42, no. 1, pp. 66–68, 1983.

[58] W. I. Wang, R. F. Marks, and L. Vina, "High-purity GaAs grown by molecular-beam epitaxy," *Journal of Applied Physics*, vol. 59, no. 3, pp. 937–939, 1986.

[59] M. Kaminska and E. R. Weber, "Low Temperature GaAs: Electrical and Optical Properties," in *Defects in Semiconductors 16*, vol. 83 of *Materials Science Forum*, pp. 1033–1044, Trans Tech Publications, 1992.

[60] M. Luysberg, H. Sohn, A. Prasad, P. Specht, Z. Liliental-Weber, E. R. Weber, J. Gebauer, and R. Krause-Rehberg, "Effects of the growth temperature and As/Ga flux ratio on the incorporation of excess As into low temperature grown GaAs," *Journal of Applied Physics*, vol. 83, no. 1, pp. 561–566, 1998.

[61] B. J. Bohn, T. Simon, M. Gramlich, A. F. Richter, L. Polavarapu, A. S. Urban, and J. Feldmann, "Dephasing and Quantum Beating of Excitons in Methylammonium Lead Iodide Perovskite Nanoplatelets," *ACS Photonics*, vol. 5, no. 2, pp. 648–654, 2018.

[62] T. Yajima and Y. Taira, “Spatial Optical Parametric Coupling of Picosecond Light Pulses and Transverse Relaxation Effect in Resonant Media,” *Journal of the Physical Society of Japan*, vol. 47, no. 5, pp. 1620–1626, 1979.

[63] C. W. Schultheis, L., Kuhl, J., Honold, A., Tu, “Ultrafast Phase Relaxation of Excitons via Exciton-Exciton and Exciton-Electron Collisions,” *Physical Review Letters*, vol. 57, no. 13, pp. 1635–1638, 1986.

[64] D. Webber, L. Hacquebard, X. Liu, M. Dobrowolska, J. K. Furdyna, and K. C. Hall, “Role of many-body effects in the coherent dynamics of excitons in low-temperature-grown GaAs,” *Applied Physics Letters*, vol. 107, no. 14, p. 142108, 2015.

[65] M. Yildirim, S. March, R. Mathew, A. Gamouras, X. Liu, M. Dobrowolska, J. K. Furdyna, and K. C. Hall, “Interband dephasing and photon echo response in GaMnAs,” *Applied Physics Letters*, vol. 101, no. 6, p. 062403, 2012.

[66] W. S. A. Lohner, K. Rick, P. Leisching, A. Leitenstorfer, T. Elsaeser, T. Kuhn, F. Rossi, “Coherent Optical Polarization of Bulk GaAs Studied by Femtosecond Photon-Echo Spectroscopy,” *Physical Review Letter*, vol. 71, no. 1, pp. 1–4, 1993.

[67] H. Wang, K. Ferrio, D. G. Steel, Y. Z. Hu, R. Binder, and S. W. Koch, “Transient nonlinear optical response from excitation induced dephasing in GaAs,” *Phys. Rev. Lett.*, vol. 71, pp. 1261–1264, aug 1993.

[68] M. Wehner, D. Steinbach, and M. Wegener, “Ultrafast coherent transients due to exciton-continuum scattering in bulk GaAs,” *Physical Review B - Condensed Matter and Materials Physics*, vol. 54, no. 8, pp. R5211–R5214, 1996.

[69] M. Yildirim, S. March, R. Mathew, a. Gamouras, X. Liu, M. Dobrowolska, J. K. Furdyna, and K. C. Hall, “Electronic structure of Ga1-xMnxAs probed by four-wave mixing spectroscopy,” *Physical Review B - Condensed Matter and Materials Physics*, vol. 84, no. 12, pp. 1–5, 2011.

[70] D. Webber, M. Yildirim, L. Hacquebard, S. March, R. Mathew, a. Gamouras, X. Liu, M. Dobrowolska, J. K. Furdyna, and K. C. Hall, “Observation of the exciton and Urbach band tail in low-temperature-grown GaAs using four-wave mixing spectroscopy,” *Applied Physics Letters*, vol. 105, no. 18, p. 182109, 2014.

[71] G. R. Allan and H. M. van Driel, “Coherence dynamics of excitons and continuum excitations in inp,” *Physical Review B - Condensed Matter and Materials Physics*, vol. 59, no. 24, pp. 15740–15747, 1999.

[72] K. Hall, G. R. Allan, H. M. van Driel, T. Krivosheeva, and W. Pötz, “Coherent response of spin-orbit split-off excitons in InP: Isolation of many-body effects through interference,” *Physical Review B*, vol. 65, no. 20, p. 201201, 2002.

[73] J. M. Hvam, “Optical Nonlinearities and Phase Coherence in CdSe Studied by Transient Four-Wave Mixing,” *IEEE Journal of Quantum Electronics*, vol. 25, no. 5, pp. 904–912, 1989.

[74] V. G. Lyssenko, J. Erland, I. Balslev, K. H. Pantke, B. S. Razbirin, and J. M. Hvam, “Nature of nonlinear four-wave-mixing beats in semiconductors,” *Physical Review B*, vol. 48, no. 8, pp. 5720–5723, 1993.

[75] J. M. H. J. Erland, K.-H. Pantke, V. Mizeikis, V. G. Lyssenko, “Spectrally resolved four-wave mixing in semiconductors: Influence of inhomogeneous broadening,” *Physical Review B*, vol. 50, no. 20, pp. 47–55, 1994.

[76] T. Rappen, U. Peter, G. Mohs, W. Schafer, and M. Wegener, “Coherent dynamics of continuum and bound states in germanium,” *Semiconductor Science and Technology*, vol. 9, no. 5 S, pp. 422–424, 1994.

[77] T. Rappen, U.-G. Peter, M. Wegener, and W. Schäfer, “Polarization dependence of dephasing processes: A probe for many-body effects,” *Physical Review B*, vol. 49, no. 15, pp. 10774–10777, 1994.

[78] A. Honold, L. Schultheis, J. Kuhl, and C. W. Tu, “Collision broadening of two-dimensional excitons in a GaAs single quantum well,” *Physical Review B*, vol. 40, no. 9, pp. 6442–6445, 1989.

[79] K. El Sayed, D. Birkedal, V. G. Lyssenko, and J. M. Hvam, “Continuum contribution to excitonic four-wave mixing due to interaction-induced nonlinearities: A numerical study,” *Physical Review B*, vol. 55, no. 4, pp. 2456–2465, 1997.

[80] K. Leo, M. Wegener, J. Shah, D. S. Chemla, E. O. Göbel, T. C. Damen, S. Schmitt-Rink, and W. Schäfer, “Effects of coherent polarization interactions on time-resolved degenerate four-wave mixing,” *Physical Review Letters*, vol. 65, no. 11, pp. 1340–1343, 1990.

[81] D.-S. Kim, J. Shah, J. E. Cunningham, T. C. Damen, W. Schäfer, M. Hartmann, and S. Schmitt-Rink, “Giant excitonic resonance in time-resolved four-wave mixing in quantum wells,” *Phys. Rev. Lett.*, vol. 68, pp. 1006–1009, feb 1992.

[82] D.-S. Kim, J. Shah, T. C. Damen, W. Schäfer, F. Jahnke, S. Schmitt-Rink, and K. Köhler, “Unusually slow temporal evolution of femtosecond four-wave-mixing signals in intrinsic GaAs quantum wells: Direct evidence for the dominance of interaction effects,” *Phys. Rev. Lett.*, vol. 69, pp. 2725–2728, nov 1992.

[83] S. T. Cundiff, H. Wang, and D. G. Steel, “Polarization-dependent picosecond excitonic nonlinearities and the complexities of disorder,” *Physical Review B*, vol. 46, no. 11, pp. 7248–7251, 1992.

[84] S. T. Cundiff, M. Koch, W. H. Knox, J. Shah, and W. Stolz, "Optical Coherence in Semiconductors: Strong Emission Mediated by Nondegenerate Interactions.," *Physical Review Letters*, vol. 77, no. 6, pp. 1107–1110, 1996.

[85] T. Rappen, G. Mohs, and M. Wegener, "Polariton dynamics in quantum wells studied by femtosecond four-wave mixing," *Phys. Rev. B*, vol. 47, pp. 9658–9662, apr 1993.

[86] J. M. Shacklette and S. T. Cundiff, "Role of excitation-induced shift in the coherent optical response of semiconductors," *Physical Review B*, vol. 66, no. 4, p. 045309, 2002.

[87] D. Webber, "TRANSIENT FOUR-WAVE MIXING STUDIES OF GaAs , AND CH3NH3PbI3," *PhD Thesis*, no. December, 2017.

[88] W.-J. Yin, T. Shi, and Y. Yan, "Unusual defect physics in CH3NH3PbI3 perovskite solar cell absorber.," *Applied Physics Letters*, vol. 104, no. 6, p. 063903, 2014.

[89] A. a. Bakulin, O. Selig, H. J. Bakker, Y. L. a. Rezus, C. Muller, T. Glaser, R. Lovrincic, Z. Sun, Z. Chen, A. Walsh, J. M. Frost, and T. L. C. Jansen, "Real-Time Observation of Organic Cation Reorientation in Methylammonium Lead Iodide Perovskites," *Journal of Physical Chemistry Letters*, vol. 6, no. 18, pp. 3663–3669, 2015.

[90] J. Ma and L.-w. Wang, "Nanoscale Charge Localization Induced by Random Orientations of Organic Molecules in Hybrid Perovskite CH 3 NH 3 PbI 3," *Nano Letters*, no. 15, pp. 248–253, 2015.

[91] G. Segschneider, T. Dekorsy, H. Kurz, R. Hey, and K. Ploog, "Energy resolved ultrafast relaxation dynamics close to the band edge of low-temperature grown GaAs," *Applied Physics Letters*, vol. 71, p. 2779, 1997.

[92] C. Quarti, G. Grancini, E. Mosconi, P. Bruno, J. M. Ball, M. M. Lee, H. J. Snaith, A. Petrozza, and F. D. Angelis, "The raman spectrum of the CH3NH3PbI3 hybrid perovskite: Interplay of theory and experiment," *Journal of Physical Chemistry Letters*, vol. 5, no. 2, pp. 279–284, 2014.

[93] F. Brivio, J. M. Frost, J. M. Skelton, A. J. Jackson, O. J. Weber, M. T. Weller, A. R. Go??i, A. M. a. Leguy, P. R. F. Barnes, and A. Walsh, "Lattice dynamics and vibrational spectra of the orthorhombic, tetragonal, and cubic phases of methylammonium lead iodide," *Physical Review B - Condensed Matter and Materials Physics*, vol. 92, no. 14, pp. 1–8, 2015.

[94] J. Even, L. Pedesseau, and C. Katan, "Analysis of multivalley and multibandgap absorption and enhancement of free carriers related to exciton screening in hybrid perovskites," *Journal of Physical Chemistry C*, vol. 118, no. 22, pp. 11566–11572, 2014.

[95] O. Flender, J. R. Klein, T. Lenzer, and K. Oum, “Ultrafast photoinduced dynamics of the organolead trihalide perovskite CH3NH3PbI3 on mesoporous TiO 2 scaffolds in the 320–920 nm range,” *Phys. Chem. Chem. Phys.*, vol. 17, pp. 19238–19246, 2015.

[96] M. B. Price, J. Butkus, T. C. Jellicoe, A. Sadhanala, A. Briane, J. E. Halpert, K. Broch, J. M. Hodgkiss, R. H. Friend, and F. Deschler, “Hot-carrier cooling and photoinduced refractive index changes in organic–inorganic lead halide perovskites,” *Nature Communications*, vol. 6, no. May, p. 8420, 2015.

[97] D. D. Awschalom, D. Loss, and N. Samarth, “Semiconductor Spintronics and Quantum Computation,” 2002.

[98] J. Even, L. Pedesseau, M. a. Dupertuis, J. M. Jancu, and C. Katan, “Electronic model for self-assembled hybrid organic/perovskite semiconductors: Reverse band edge electronic states ordering and spin-orbit coupling,” *Physical Review B - Condensed Matter and Materials Physics*, vol. 86, no. 20, pp. 3–6, 2012.

[99] M. Kepenekian and J. Even, “Rashba and Dresselhaus Couplings in Halide Perovskites: Accomplishments and Opportunities for Spintronics and Spin-Orbitronics,” *Journal of Physical Chemistry Letters*, vol. 8, no. 14, pp. 3362–3370, 2017.

[100] O. Madelung, *Semiconductors — Basic Data*. Springer Berlin Heidelberg, 2012.

[101] P. YU and M. Cardona, *Fundamentals of Semiconductors: Physics and Materials Properties*. Graduate Texts in Physics, Springer Berlin Heidelberg, 2010.

[102] J. Even, L. Pedesseau, J. M. Jancu, and C. Katan, “Importance of spin-orbit coupling in hybrid organic/inorganic perovskites for photovoltaic applications,” *Journal of Physical Chemistry Letters*, vol. 4, no. 17, pp. 2999–3005, 2013.

[103] G. Dresselhaus, “Spin-Orbit Coupling Effects in Zinc Blende Structures,” *Phys.Rev.*, vol. 100, no. 2, pp. 580–586, 1955.

[104] Y. A. Bychkov and E. I. Rashba, “Properties of a 2D electron gas with lifted spectral degeneracy,” 1984.

[105] M. Kim, J. Im, a. J. Freeman, J. Ihm, and H. Jin, “Switchable S = 1/2 and J = 1/2 Rashba bands in ferroelectric halide perovskites,” *Proceedings of the National Academy of Sciences*, vol. 111, no. 19, pp. 6900–6904, 2014.

[106] M. Kepenekian, R. Robles, C. Katan, D. Sapori, L. Pedesseau, and J. Even, “Rashba and Dresselhaus Effects in Hybrid Organic-Inorganic Perovskites: From Basics to Devices,” *ACS Nano*, vol. 9, no. 12, pp. 11557–11567, 2015.

[107] J. Even, L. Pedesseau, M.-a. Dupertuis, J.-m. Jancu, J. Even, L. Pedesseau, M.-a. Dupertuis, J.-m. Jancu, and C. K. An, “An electronic model for self-assembled hybrid organic / perovskite semiconductors : reverse band edge electronic states ordering and spin-orbit coupling To cite this version : HAL Id : hal-00753888 An electronic model for self-assembled hybrid organic / p,” 2012.

[108] J. Even, L. Pedesseau, J.-M. Jancu, and C. Katan, “DFT and kp modelling of the phase transitions of lead and tin halide perovskites for photovoltaic cells,” *physica status solidi (RRL) - Rapid Research Letters*, vol. 8, no. 1, pp. 31–35, 2014.

[109] F. Brivio, K. T. Butler, A. Walsh, and M. Van Schilfgaarde, “Relativistic quasiparticle self-consistent electronic structure of hybrid halide perovskite photovoltaic absorbers,” *Physical Review B - Condensed Matter and Materials Physics*, vol. 89, no. 15, pp. 1–6, 2014.

[110] A. Amat, E. Mosconi, E. Ronca, C. Quarti, P. Umari, M. K. Nazeeruddin, M. Grätzel, and F. De Angelis, “Cation-induced band-gap tuning in organohalide perovskites: Interplay of spin-orbit coupling and octahedra tilting,” *Nano Letters*, vol. 14, no. 6, pp. 3608–3616, 2014.

[111] H. Haug and S. W. Koch, *Quantum Theory of the Optical and Electronic Properties of Semiconductors*. WORLD SCIENTIFIC, 1990.

[112] Z. G. Yu, “The Rashba effect and indirect electron-hole recombination in hybrid organic-inorganic perovskites,” *Physical Chemistry Chemical Physics*, vol. 19, no. 23, pp. 14907–14912, 2017.

[113] T. Rappen, U. Peter, M. Wegener, and W. Schafer, “Coherent dynamics of continuum and exciton states studied by spectrally resolved fs four-wave mixing,” *Physical Review B*, vol. 48, no. 7, pp. 4879–4882, 1993.

[114] N. Ahn, D. Y. Son, I. H. Jang, S. M. Kang, M. Choi, and N. G. Park, “Highly Reproducible Perovskite Solar Cells with Average Efficiency of 18.3% and Best Efficiency of 19.7% Fabricated via Lewis Base Adduct of Lead(II) Iodide,” *Journal of the American Chemical Society*, vol. 137, no. 27, pp. 8696–8699, 2015.

[115] M. Saliba, T. Matsui, K. Domanski, J.-y. Seo, A. Ummadisingu, M. Zakeeruddin, W. R. Tress, A. Abate, A. Hagfeldt, and M. Grätzel, “<Incorporation of rubidium cations into perovskite solar cells improves photovoltaic performance.pdf>,” vol. 5557, no. September, pp. 1–9, 2016.

[116] M. Saliba, T. Matsui, J. Y. Seo, K. Domanski, J. P. Correa-Baena, M. K. Nazeeruddin, S. M. Zakeeruddin, W. Tress, A. Abate, A. Hagfeldt, and M. Grätzel, “Cesium-containing triple cation perovskite solar cells: Improved

stability, reproducibility and high efficiency," *Energy and Environmental Science*, vol. 9, no. 6, pp. 1989–1997, 2016.

[117] F. Liu, Q. Dong, M. K. Wong, A. B. Djurišić, A. Ng, Z. Ren, Q. Shen, C. Surya, W. K. Chan, J. Wang, A. M. C. Ng, C. Liao, H. Li, K. Shih, C. Wei, H. Su, and J. Dai, "Is Excess PbI2Beneficial for Perovskite Solar Cell Performance?," *Advanced Energy Materials*, vol. 6, no. 7, pp. 1–9, 2016.

[118] Z. Xiao, C. Bi, Y. Shao, Q. Dong, Q. Wang, Y. Yuan, C. Wang, Y. Gao, and J. Huang, "Efficient, high yield perovskite photovoltaic devices grown by interdiffusion of solution-processed precursor stacking layers," *Energy Environ. Sci.*, vol. 7, no. 8, pp. 2619–2623, 2014.

[119] J. Landman, C. Morgan, and J. Schick, "Arsenic interstitials and interstitial complexes in low-temperature grown GaAs," *Physical Review B - Condensed Matter and Materials Physics*, vol. 55, no. 23, pp. 15581–15586, 1997.

[120] A. E. Siegman, *Lasers*. University Science Books, 1986.

[121] T. J. Savenije, C. S. Ponseca, L. Kunneman, M. Abdellah, K. Zheng, Y. Tian, Q. Zhu, S. E. Canton, I. G. Scheblykin, T. Pullerits, A. Yartsev, and V. Sundström, "Thermally activated exciton dissociation and recombination control the carrier dynamics in organometal halide perovskite," *Journal of Physical Chemistry Letters*, vol. 5, no. 13, pp. 2189–2194, 2014.

[122] S. Sun, T. Salim, N. Mathews, M. Duchamp, C. Boothroyd, G. Xing, T. C. Sum, and Y. M. Lam, "The origin of high efficiency in low-temperature solution-processable bilayer organometal halide hybrid solar cells," *Energy & Environmental Science*, vol. 7, no. 1, p. 399, 2014.

[123] T. Ishihara, "Optical properties of PbI-based perovskite structures," *Journal of Luminescence*, vol. 60, pp. 269–274, 1994.

[124] Y. Yamada, T. Nakamura, M. Endo, A. Wakamiya, and Y. Kanemitsu, "Near-band-edge optical responses of solution-processed organic–inorganic hybrid perovskite CH3NH3PbI3 on mesoporous TiO2 electrodes," *Applied Physics Express*, vol. 7, no. 3, p. 032302, 2014.

[125] H. Tahara, M. Endo, A. Wakamiya, and Y. Kanemitsu, "Experimental Evidence of Localized Shallow States in Orthorhombic Phase of CH3NH3PbI3 Perovskite Thin Films Revealed by Photocurrent Beat Spectroscopy," *The Journal of Physical Chemistry C*, p. acs.jpcc.6b01283, 2016.

[126] M. Koch, D. Weber, J. Feldmann, E. O. Göbel, T. Meier, A. Schulze, P. Thomas, S. Schmitt-Rink, and K. Ploog, "Subpicosecond photon-echo spectroscopy on GaAs/AlAs short-period superlattices," *Physical Review B*, vol. 47, no. 3, pp. 1532–1539, 1993.

[127] P. Gilliot, D. Brinkmann, J. Kudrna, O. Cregut, R. Levy, A. Arnoult, J. Cibert, and S. Tatarenko, “Quantum beats between trion and exciton transitions in modulation-doped CdTe quantum wells,” *Physical Review B - Condensed Matter and Materials Physics*, vol. 60, no. 8, pp. 5797–5801, 1999.

[128] P. C. Becker, H. L. Fragnito, C. H. Cruz, R. L. Fork, J. E. Cunningham, J. E. Henry, and C. V. Shank, “Femtosecond photon echoes from band-to-band transitions in GaAs,” *Physical Review Letters*, vol. 61, no. 14, pp. 1647–1649, 1988.

[129] U. Siegner, D. Weber, E. O. Göbel, D. Bennhardt, V. Heuckeroth, R. Saleh, S. D. Baranovskii, P. Thomas, H. Schwab, C. Klingshirn, J. M. Hvam, and V. G. Lyssenko, “Optical dephasing in semiconductor mixed crystals,” *Physical Review B*, vol. 46, no. 8, pp. 4564–4581, 1992.

[130] E. Menéndez-Proupin, P. Palacios, P. Wahnón, and J. C. Conesa, “Self-consistent relativistic band structure of the CH3NH3PbI3 perovskite,” *Physical Review B*, vol. 90, no. 4, p. 045207, 2014.

[131] F. Deschler, M. Price, S. Pathak, L. E. Klintberg, D.-d. Jarausch, R. Higler, S. H¨ttner, T. Leijtens, S. D. Stranks, H. J. Snaith, M. Atat¨re, R. T. Phillips, and R. H. Friend, “High Photoluminescence Efficiency and Optically Pumped Lasing in Solution-Processed Mixed Halide Perovskite Semiconductors,” vol. 5, pp. 1421–1426, 2014.

[132] M. T. Trinh, X. Wu, D. Niesner, and X. Zhu, “Many-Body Interactions in Photo-Excited Lead Iodide Perovskite,” *J. Mater. Chem. A*, vol. 3, pp. 9285–9290, 2015.

[133] J. S. Manser and P. V. Kamat, “Band filling with free charge carriers in organometal halide perovskites,” *Nat. Photonics*, vol. 8, no. 9, pp. 737–743, 2014.

[134] H. Hoppe and N. S. Sariciftci, “Organic solar cells: An overview,” *Journal of Materials Research*, vol. 19, no. 07, pp. 1924–1945, 2004.

[135] X. Wu, M. T. Trinh, and X.-y. Zhu, “Excitonic Many-Body Interactions in Two-Dimensional Lead Iodide Perovskite Quantum Wells,” *The Journal of Physical Chemistry C*, 2015.

[136] K. W. Stone, D. B. Turner, K. Gundogdu, S. T. Cundiff, and K. A. Nelson, “Exciton-exciton correlations revealed by twoquantum, two-dimensional fourier transform optical spectroscopy,” *Accounts of Chemical Research*, vol. 42, no. 9, pp. 1452–1461, 2009.

[137] S. D. Stranks, V. M. Burlakov, T. Leijtens, J. M. Ball, A. Goriely, and H. J. Snaith, “Recombination Kinetics in Organic-Inorganic Perovskites : Excitons ,

Free Charge , and Subgap States," *Physical Review Applied*, vol. 2, p. 034007, 2014.

[138] G. Xing, N. Mathews, S. S. Lim, N. Yantara, X. Liu, D. Sabba, M. Grätzel, S. Mhaisalkar, and T. C. Sum, "Low-temperature solution-processed wavelength-tunable perovskites for lasing.," *Nat. Mater.*, vol. 13, no. 5, pp. 476–80, 2014.

[139] W. A. Hügel, M. F. Heinrich, M. Wegener, Q. T. Vu, L. Bányai, and H. Haug, "Photon Echoes from Semiconductor Band-to-Band Continuum Transitions in the Regime of Coulomb Quantum Kinetics," *Phys. Rev. Lett.*, vol. 83, no. 16, pp. 3313–3316, 1999.

[140] A. Krotkus, "Semiconductors for terahertz photonics applications," *Journal of Physics D: Applied Physics*, vol. 43, p. 273001, 2010.

[141] S. John, C. Soukoulis, M. H. Cohen, and E. N. Economou, "Theory of electron band tails and the urbach optical-absorption edge," *Physical Review Letters*, vol. 57, no. 14, pp. 1777–1780, 1986.

[142] H. Zhu, K. Miyata, Y. Fu, J. Wang, P. Joshi, D. Niesner, K. W. Williams, S. Jin, and X.-Y. Zhu, "Screening in Crystalline Liquids Protects Energetic Carriers in Hybrid Perovskites," *Science (New York, N.Y.)*, vol. 353, no. 6306, pp. 1409–1413, 2016.

[143] D. Niesner, H. Zhu, K. Miyata, P. P. Joshi, T. J. S. Evans, B. J. Kudisch, M. T. Trinh, M. Marks, and X.-Y. Zhu, "Persistent Energetic Electrons in Methylammonium Lead Iodide Perovskite Thin Films," *Journal of the American Chemical Society*, pp. 15717–15726, 2016.

[144] S. U. Dankowski, D. Streb, M. Ruff, P. Kiesel, M. Kneissl, B. Knüpfer, G. H. Döhler, U. D. Keil, C. B. Sørenson, and A. K. Verma, "Above band gap absorption spectra of the arsenic antisite defect in low temperature grown GaAs and AlGaAs," *Applied Physics Letters*, vol. 68, no. 1, pp. 37–39, 1996.

[145] D. Webber, T. de Boer, M. Yildirim, S. March, R. Mathew, A. Gamouras, X. Liu, M. Dobrowolska, J. Furdyna, and K. Hall, "Measurement of Coherence Decay in GaMnAs Using Femtosecond Four-wave Mixing," no. 82, p. e51094, 2013.

[146] Y. Z. Hu, R. Binder, S. W. Koch, S. T. Cundiff, H. Wang, and D. G. Steel, "Excitation and polarization effects in semiconductor four-wave-mixing spectroscopy," *Physical Review B*, vol. 49, no. 20, pp. 14382–14386, 1994.

[147] D. Niesner, M. Wilhelm, I. Levchuk, A. Osvet, S. Shrestha, M. Batentschuk, C. Brabec, and T. Fauster, "Giant Rashba Splitting in CH3NH3PbBr3 Organic-Inorganic Perovskite," *Physical Review Letters*, vol. 117, no. 12, p. 126401, 2016.

[148] K. Ishizaka, M. S. Bahramy, H. Murakawa, M. Sakano, T. Shimojima, T. Sonobe, K. Koizumi, S. Shin, H. Miyahara, A. Kimura, K. Miyamoto, T. Okuda, H. Namatame, M. Taniguchi, R. Arita, N. Nagaosa, K. Kobayashi, Y. Murakami, R. Kumai, Y. Kaneko, Y. Onose, and Y. Tokura, "Giant Rashba-type spin splitting in bulk BiTeI," *Nature Materials*, vol. 10, no. 7, pp. 521–526, 2011.

[149] S. Datta and B. Das, "Electronic analog of the electro-optic modulator," *Applied Physics Letters*, vol. 56, no. 7, pp. 665–667, 1990.

[150] K. C. Hall, W. H. Lau, K. Gündoğdu, M. E. Flatté, and T. F. Boggess, "Nonmagnetic semiconductor spin transistor," *Applied Physics Letters*, vol. 83, no. 14, pp. 2937–2939, 2003.

[151] K. C. Hall and M. E. Flatt ́, "Performance of a spin-based insulated gate field effect transistor," *Applied Physics Letters*, vol. 88, no. 16, pp. 2016–2019, 2006.

[152] M. Isarov, L. Z. Tan, M. I. Bodnarchuk, M. V. Kovalenko, A. M. Rappe, and E. Lifshitz, "Rashba effect in a single colloidal CsPbBr3perovskite nanocrystal detected by magneto-optical measurements," *Nano Letters*, vol. 17, no. 8, pp. 5020–5026, 2017.

[153] T. Wang, B. Daiber, J. M. Frost, S. A. Mann, E. C. Garnett, A. Walsh, and B. Ehrler, "Indirect to direct bandgap transition in methylammonium lead halide perovskite," *Energy Environ. Sci.*, vol. 10, no. 2, pp. 509–515, 2017.

[154] Y. Zhai, S. Baniya, C. Zhang, J. Li, P. Haney, C. X. Sheng, E. Ehrenfreund, and Z. V. Vardeny, "Giant Rashba splitting in 2D organic-inorganic halide perovskites measured by transient spectroscopies," *Science Advances*, vol. 3, no. 7, pp. 1–7, 2017.

[155] S. B. Todd, D. B. Riley, A. Ramachandran, C. Clegg, A. Binai-motlagh, S. A. March, I. G. Hill, C. C. Stoumpos, M. G. Kanatzidis, and K. C. Hall, "Detection of Rashba spin splitting in 2D organic-inorganic perovskite via precessional carrier spin relaxation," pp. 1–10.

[156] J. P. H. Rivett, L. Z. Tan, M. B. Price, S. A. Bourelle, N. J. L. K. Davis, J. Xiao, Y. Zou, R. Middleton, B. Sun, A. M. Rappe, D. Credgington, and F. Deschler, "Long-lived polarization memory in the electronic states of lead-halide perovskites from local structural dynamics," *Nature Communications*, vol. 9, no. 1, p. 3531, 2018.

[157] D. Niesner, M. Hauck, S. Shrestha, I. Levchuk, G. J. Matt, A. Osvet, M. Batentschuk, C. Brabec, H. B. Weber, and T. Fauster, "Structural fluctuations cause spin-split states in tetragonal (CH3NH3)PbI3 as evidenced by the circular photogalvanic effect," *Proceedings of the National Academy of Sciences*, p. 201805422, 2018.

[158] M. Kim, J. Im, A. J. Freeman, J. Ihm, and H. Jin, "Switchable S = 1/2 and J = 1/2 Rashba bands in ferroelectric halide perovskites," *Proceedings of the National Academy of Sciences*, vol. 111, no. 19, pp. 6900–6904, 2014.

[159] A. Stroppa, D. Di Sante, P. Barone, M. Bokdam, G. Kresse, C. Franchini, M.-H. Whangbo, and S. Picozzi, "Tunable ferroelectric polarization and its interplay with spin–orbit coupling in tin iodide perovskites," *Nature Communications*, vol. 5, p. 5900, 2014.

[160] C. Motta, F. E. Mellouhi, S. Kais, N. Tabet, F. Alharbi, and S. Sanvito, "Revealing the role of organic cations in hybrid halide perovskites CH3NH3PbI3," *Nature Communications*, vol. 6, no. May 2014, pp. 1–7, 2014.

[161] T. Etienne, E. Mosconi, and F. De Angelis, "Dynamical Origin of the Rashba Effect in Organohalide Lead Perovskites: A Key to Suppressed Carrier Recombination in Perovskite Solar Cells?," *Journal of Physical Chemistry Letters*, vol. 7, no. 9, pp. 1638–1645, 2016.

[162] L. Leppert, S. E. Reyes-Lillo, and J. B. Neaton, "Electric Field- and Strain-Induced Rashba Effect in Hybrid Halide Perovskites," *Journal of Physical Chemistry Letters*, vol. 7, no. 18, pp. 3683–3689, 2016.

[163] P. Azarhoosh, S. McKechnie, J. M. Frost, A. Walsh, and M. Van Schilfgaarde, "Research Update: Relativistic origin of slow electron-hole recombination in hybrid halide perovskite solar cells," *APL Materials*, vol. 4, no. 9, 2016.

[164] E. Mosconi, T. Etienne, and F. De Angelis, "Rashba Band Splitting in Organohalide Lead Perovskites: Bulk and Surface Effects," *The Journal of Physical Chemistry Letters*, p. acs.jpclett.7b00328, 2017.

[165] X. Che, B. Traore, C. Katan, M. Kepenekian, and J. Even, "Does Rashba splitting in CH3NH3PbBr3 arise from 2 × 2 surface reconstruction?," *Physical Chemistry Chemical Physics*, no. 001, pp. 9638–9643, 2018.

[166] X. Zhang, J. X. Shen, and C. G. Van De Walle, "Three-Dimensional Spin Texture in Hybrid Perovskites and Its Impact on Optical Transitions," *Journal of Physical Chemistry Letters*, vol. 9, no. 11, pp. 2903–2908, 2018.

[167] S. McKechnie, J. M. Frost, D. Pashov, P. Azarhoosh, A. Walsh, and M. Van Schilfgaarde, "Dynamic symmetry breaking and spin splitting in metal halide perovskites," *Physical Review B*, vol. 98, no. 8, pp. 1–7, 2018.

[168] K. Onodera, T. Masumoto, and M. Kimura, "980nm compact optical isolators using Cdl,Mn,Hg2Te single crystals for high power pumping laser diodes," *Electronics Letters*, vol. 30, no. 23, pp. 1954–1955, 1994.

[169] J. Rudolph, D. Hägele, H. M. Gibbs, G. Khitrova, and M. Oestreich, "Laser threshold reduction in a spintronic device," *Applied Physics Letters*, vol. 82, no. 25, pp. 4516–4518, 2003.

[170] K. C. Hall, J. P. Zahn, A. Gamouras, S. March, J. L. Robb, X. Liu, and J. K. Furdyna, "Ultrafast optical control of coercivity in GaMnAs," *Applied Physics Letters*, vol. 93, no. 3, 2008.

[171] Y. Nishikawa, A. Tackeuchi, S. Nakamura, S. Muto, and N. Yokoyama, "All-optical picosecond switching of a quantum well etalon using spin-polarization relaxation," *Applied Physics Letters*, vol. 839, no. 1995, p. 839, 1995.

[172] K. C. Hall, S. W. Leonard, H. M. Van Driel, A. R. Kost, E. Selvig, and D. H. Chow, "Subpicosecond spin relaxation in GaAsSb multiple quantum wells," *Applied Physics Letters*, vol. 75, no. 23, pp. 3665–3667, 1999.

[173] C. Zhang, D. Sun, and Z. V. Vardeny, "Multifunctional Optoelectronic–Spintronic Device Based on Hybrid Organometal Trihalide Perovskites," *Advanced Electronic Materials*, vol. 3, no. 2, 2017.

[174] L. Dou, Y. M. Yang, J. You, Z. Hong, W. H. Chang, G. Li, and Y. Yang, "Solution-processed hybrid perovskite photodetectors with high detectivity," *Nature Communications*, vol. 5, pp. 1–6, 2014.

[175] T. Ishihara, J. Takahashi, and T. Goto, "Exciton state in two-dimensional perovskite semiconductor (C10H21NH3)2PbI4," *Solid State Communications*, vol. 69, no. 9, pp. 933–936, 1989.

[176] Z.-K. Tan, R. S. Moghaddam, M. L. Lai, P. Docampo, R. Higler, F. Deschler, M. Price, A. Sadhanala, L. M. Pazos, D. Credgington, F. Hanusch, T. Bein, H. J. Snaith, and R. H. Friend, "Bright light-emitting diodes based on organometal halide perovskite," *Nature Nanotechnology*, vol. 9, no. 9, pp. 687–692, 2014.

[177] F. Yan, J. Xing, G. Xing, L. Quan, S. T. Tan, J. Zhao, R. Su, L. Zhang, S. Chen, Y. Zhao, A. Huan, E. H. Sargent, Q. Xiong, and H. V. Demir, "Highly Efficient Visible Colloidal Lead-Halide Perovskite Nanocrystal Light-Emitting Diodes," *Nano Letters*, vol. 18, no. 5, pp. 3157–3164, 2018.

[178] F. Zheng, L. Z. Tan, S. Liu, and A. M. Rappe, "Rashba spin-orbit coupling enhanced carrier lifetime in CH3NH3PbI3," *Nano Letters*, vol. 15, no. 12, pp. 7794–7800, 2015.

[179] T. Kirchartz and U. Rau, "Decreasing Radiative Recombination Coefficients via an Indirect Band Gap in Lead Halide Perovskites," *Journal of Physical Chemistry Letters*, vol. 8, no. 6, pp. 1265–1271, 2017.

[180] Z. G. Yu, “Rashba Effect and Carrier Mobility in Hybrid Organic-Inorganic Perovskites,” *Journal of Physical Chemistry Letters*, vol. 7, no. 16, pp. 3078–3083, 2016.

[181] K. Frohna, T. Deshpande, J. Harter, W. Peng, B. A. Barker, J. B. Neaton, S. G. Louie, O. M. Bakr, D. Hsieh, and M. Bernardi, “Inversion symmetry and bulk Rashba effect in methylammonium lead iodide perovskite single crystals,” *Nature Communications*, vol. 9, no. 1, 2018.

[182] E. Conwell and V. F. Weisskopf, “Theory of impurity scattering in semiconductors,” *Physical Review*, vol. 77, no. 3, pp. 388–390, 1950.

[183] M. H. Elkins, R. Pensack, A. H. Proppe, O. Voznyy, L. N. Quan, S. O. Kelley, E. H. Sargent, and G. D. Scholes, “Biexciton Resonances Reveal Exciton Localization in Stacked Perovskite Quantum Wells,” *Journal of Physical Chemistry Letters*, vol. 8, no. 16, pp. 3895–3901, 2017.

Appendix A

Copyright Permission

Title: Four-Wave Mixing in Perovskite Photovoltaic Materials Reveals Long Dephasing Times and Weaker Many-Body Interactions than GaAs

Author: Samuel A. March, Drew B. Riley, Charlotte Clegg, et al

Publication: ACS Photonics

Publisher: American Chemical Society

Date: Jun 1, 2017

Copyright © 2017, American Chemical Society

If you're a copyright.com user, you can login to RightsLink using your copyright.com credentials. Already **a RightsLink user** or want to learn more?

PERMISSION/LICENSE IS GRANTED FOR YOUR ORDER AT NO CHARGE

This type of permission/license, instead of the standard Terms & Conditions, is sent to you because no fee is being charged for your order. Please note the following:

- Permission is granted for your request in both print and electronic formats, and translations.
- If figures and/or tables were requested, they may be adapted or used in part.
- Please print this page for your records and send a copy of it to your publisher/graduate school.
- Appropriate credit for the requested material should be given as follows: "Reprinted (adapted) with permission from (COMPLETE REFERENCE CITATION). Copyright (YEAR) American Chemical Society." Insert appropriate information in place of the capitalized words.
- One-time permission is granted only for the use specified in your request. No additional uses are granted (such as derivative works or other editions). For any other uses, please submit a new request.

Copyright © 2018 Copyright Clearance Center, Inc. All Rights Reserved. Privacy statement. Terms and Conditions.
Comments? We would like to hear from you. E-mail us at customercare@copyright.com

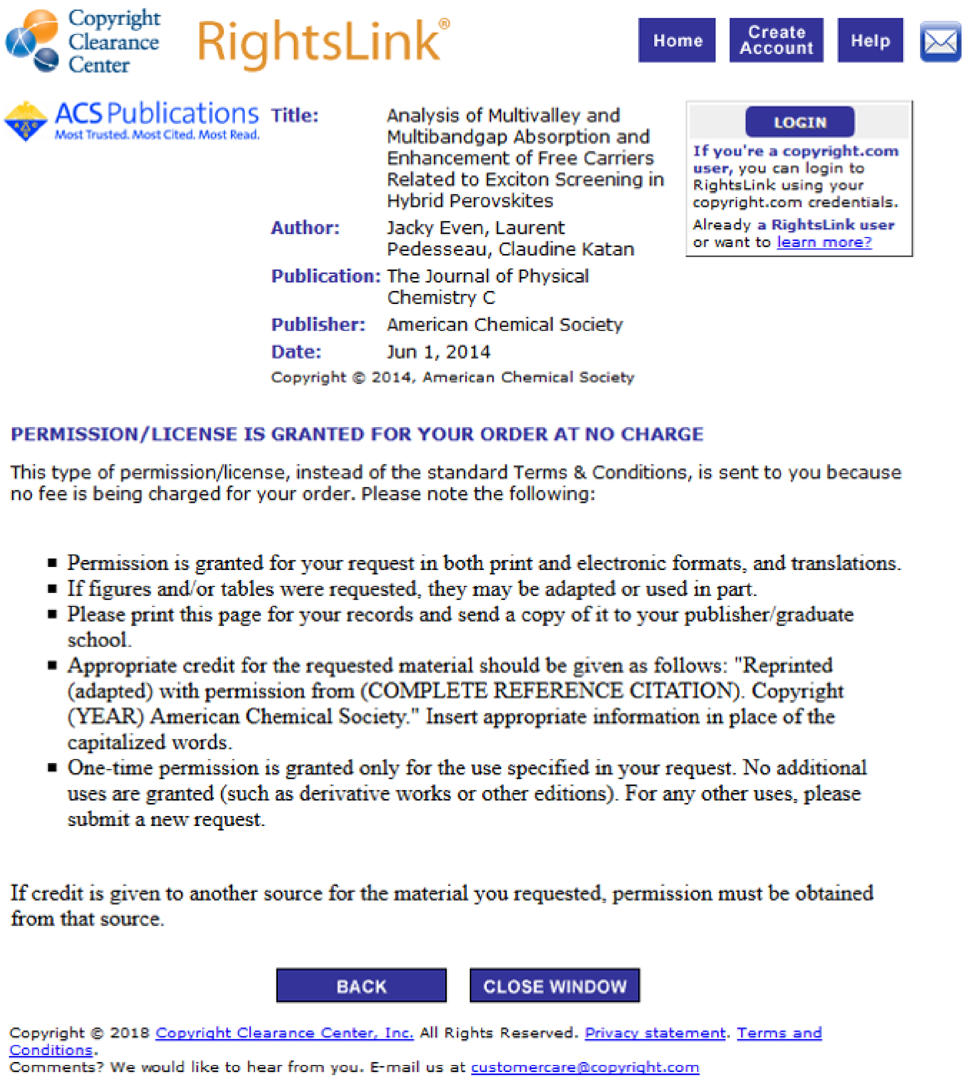

Title: Analysis of Multivalley and Multibandgap Absorption and Enhancement of Free Carriers Related to Exciton Screening in Hybrid Perovskites

Author: Jacky Even, Laurent Pedesseau, Claudine Katan

Publication: The Journal of Physical Chemistry C

Publisher: American Chemical Society

Date: Jun 1, 2014

Copyright © 2014, American Chemical Society

If you're a copyright.com user, you can login to RightsLink using your copyright.com credentials.

Already **a RightsLink user** or want to learn more?

PERMISSION/LICENSE IS GRANTED FOR YOUR ORDER AT NO CHARGE

This type of permission/license, instead of the standard Terms & Conditions, is sent to you because no fee is being charged for your order. Please note the following:

- Permission is granted for your request in both print and electronic formats, and translations.
- If figures and/or tables were requested, they may be adapted or used in part.
- Please print this page for your records and send a copy of it to your publisher/graduate school.
- Appropriate credit for the requested material should be given as follows: "Reprinted (adapted) with permission from (COMPLETE REFERENCE CITATION). Copyright (YEAR) American Chemical Society." Insert appropriate information in place of the capitalized words.
- One-time permission is granted only for the use specified in your request. No additional uses are granted (such as derivative works or other editions). For any other uses, please submit a new request.

If credit is given to another source for the material you requested, permission must be obtained from that source.

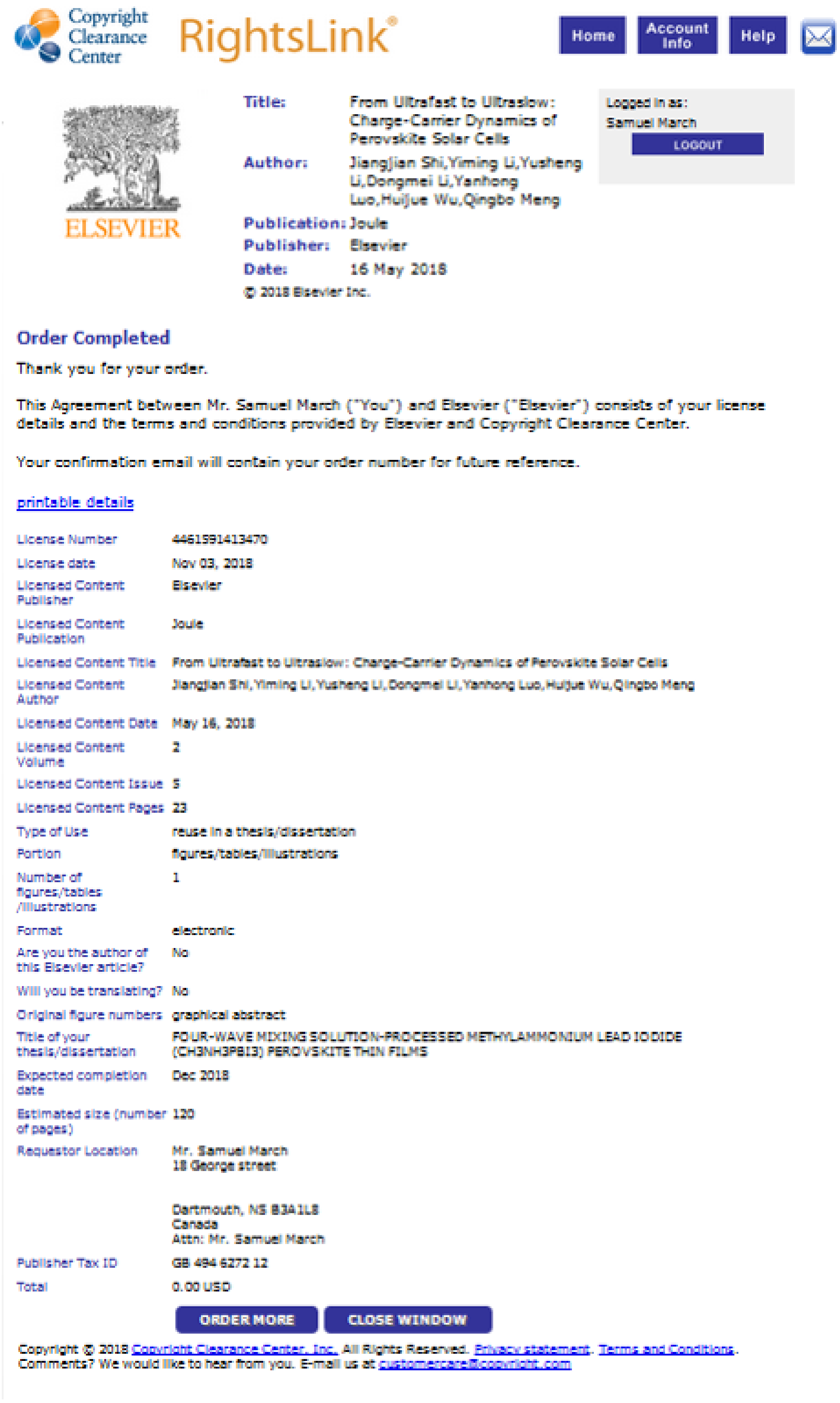

Title: From Ultrafast to Ultraslow: Charge-Carrier Dynamics of Perovskite Solar Cells
Author: Jiangjian Shi,Yiming Li,Yusheng Li,Dongmei Li,Yanhong Luo,Huijue Wu,Qingbo Meng
Publication: Joule
Publisher: Elsevier
Date: 16 May 2018
© 2018 Elsevier Inc.

Logged in as:
Samuel March

Order Completed

Thank you for your order.

This Agreement between Mr. Samuel March ("You") and Elsevier ("Elsevier") consists of your license details and the terms and conditions provided by Elsevier and Copyright Clearance Center.

Your confirmation email will contain your order number for future reference.

printable details

License Number	4461591413470
License date	Nov 03, 2018
Licensed Content Publisher	Elsevier
Licensed Content Publication	Joule
Licensed Content Title	From Ultrafast to Ultraslow: Charge-Carrier Dynamics of Perovskite Solar Cells
Licensed Content Author	Jiangjian Shi,Yiming Li,Yusheng Li,Dongmei Li,Yanhong Luo,Huijue Wu,Qingbo Meng
Licensed Content Date	May 16, 2018
Licensed Content Volume	2
Licensed Content Issue	5
Licensed Content Pages	23
Type of Use	reuse in a thesis/dissertation
Portion	figures/tables/illustrations
Number of figures/tables /illustrations	1
Format	electronic
Are you the author of this Elsevier article?	No
Will you be translating?	No
Original figure numbers	graphical abstract
Title of your thesis/dissertation	FOUR-WAVE MIXING SOLUTION-PROCESSED METHYLAMMONIUM LEAD IODIDE (CH3NH3PBI3) PEROVSKITE THIN FILMS
Expected completion date	Dec 2018
Estimated size (number of pages)	120
Requestor Location	Mr. Samuel March 18 George street Dartmouth, NS B3A1L8 Canada Attn: Mr. Samuel March
Publisher Tax ID	GB 494 6272 12
Total	0.00 USD

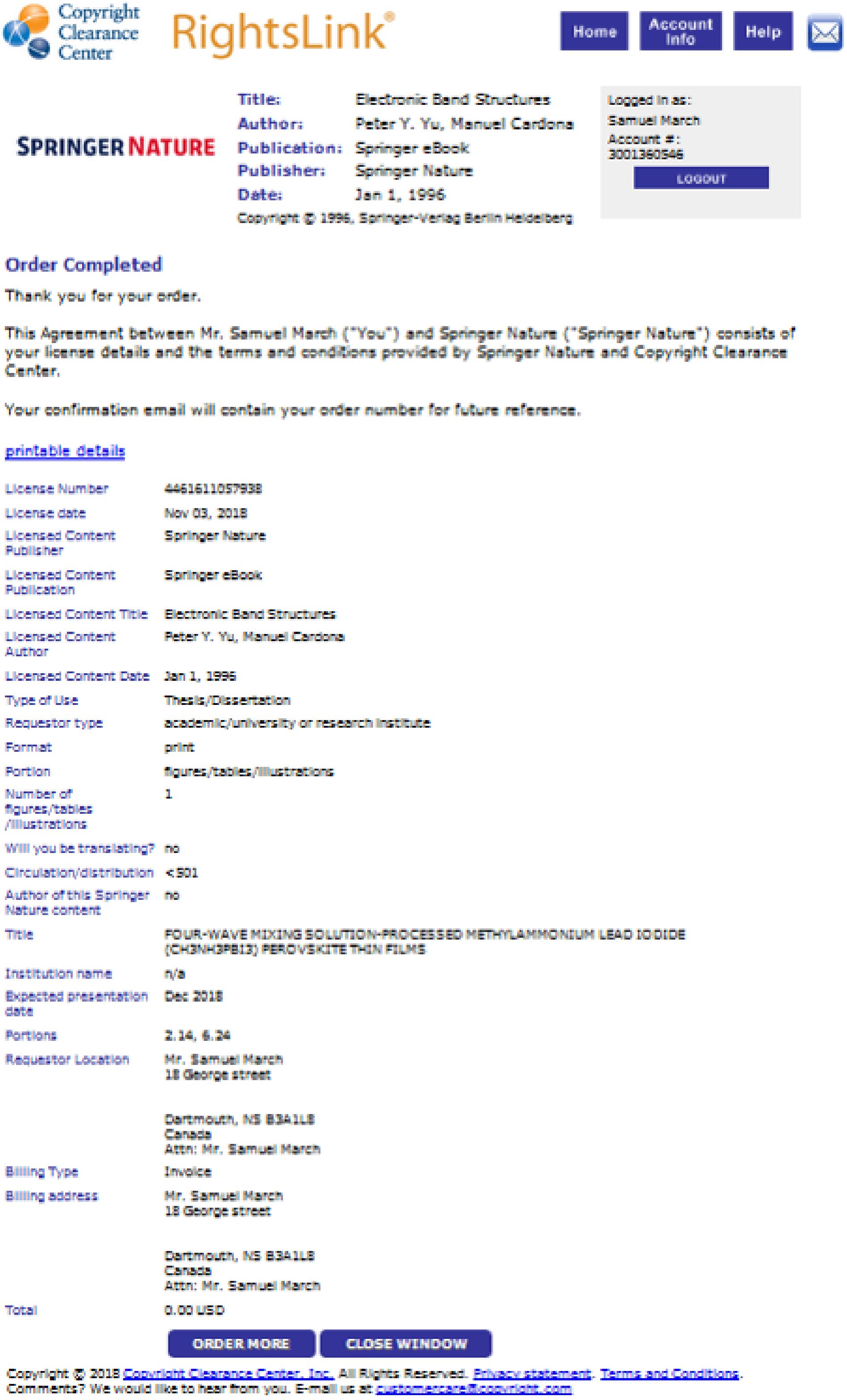

Title:	Electronic Band Structures
Author:	Peter Y. Yu, Manuel Cardona
Publication:	Springer eBook
Publisher:	Springer Nature
Date:	Jan 1, 1996

Copyright © 1996, Springer-Verlag Berlin Heidelberg

Logged in as:
Samuel March
Account #:
3001360546

Order Completed

Thank you for your order.

This Agreement between Mr. Samuel March ("You") and Springer Nature ("Springer Nature") consists of your license details and the terms and conditions provided by Springer Nature and Copyright Clearance Center.

Your confirmation email will contain your order number for future reference.

printable details

License Number	4461611057938
License date	Nov 03, 2018
Licensed Content Publisher	Springer Nature
Licensed Content Publication	Springer eBook
Licensed Content Title	Electronic Band Structures
Licensed Content Author	Peter Y. Yu, Manuel Cardona
Licensed Content Date	Jan 1, 1996
Type of Use	Thesis/Dissertation
Requestor type	academic/university or research institute
Format	print
Portion	figures/tables/illustrations
Number of figures/tables /illustrations	1
Will you be translating?	no
Circulation/distribution	<501
Author of this Springer Nature content	no
Title	FOUR-WAVE MIXING SOLUTION-PROCESSED METHYLAMMONIUM LEAD IODIDE (CH3NH3PBI3) PEROVSKITE THIN FILMS
Institution name	n/a
Expected presentation date	Dec 2018
Portions	2.14, 6.24
Requestor Location	Mr. Samuel March 18 George street Dartmouth, NS B3A1L8 Canada Attn: Mr. Samuel March
Billing Type	Invoice
Billing address	Mr. Samuel March 18 George street Dartmouth, NS B3A1L8 Canada Attn: Mr. Samuel March
Total	0.00 USD

Title: Rashba and Dresselhaus Effects in Hybrid Organic–Inorganic Perovskites: From Basics to Devices

Author: Mikaël Kepenekian, Roberto Robles, Claudine Katan, et al

Publication: ACS Nano

Publisher: American Chemical Society

Date: Dec 1, 2015

Copyright © 2015, American Chemical Society

Logged in as:
Samuel March
Account #:
3001360546

PERMISSION/LICENSE IS GRANTED FOR YOUR ORDER AT NO CHARGE

This type of permission/license, instead of the standard Terms & Conditions, is sent to you because no fee is being charged for your order. Please note the following:

- Permission is granted for your request in both print and electronic formats, and translations.
- If figures and/or tables were requested, they may be adapted or used in part.
- Please print this page for your records and send a copy of it to your publisher/graduate school.
- Appropriate credit for the requested material should be given as follows: "Reprinted (adapted) with permission from (COMPLETE REFERENCE CITATION). Copyright (YEAR) American Chemical Society." Insert appropriate information in place of the capitalized words.
- One-time permission is granted only for the use specified in your request. No additional uses are granted (such as derivative works or other editions). For any other uses, please submit a new request.

If credit is given to another source for the material you requested, permission must be obtained from that source.

Copyright © 2018 Copyright Clearance Center, Inc. All Rights Reserved. Privacy statement. Terms and Conditions.
Comments? We would like to hear from you. E-mail us at customercare@copyright.com

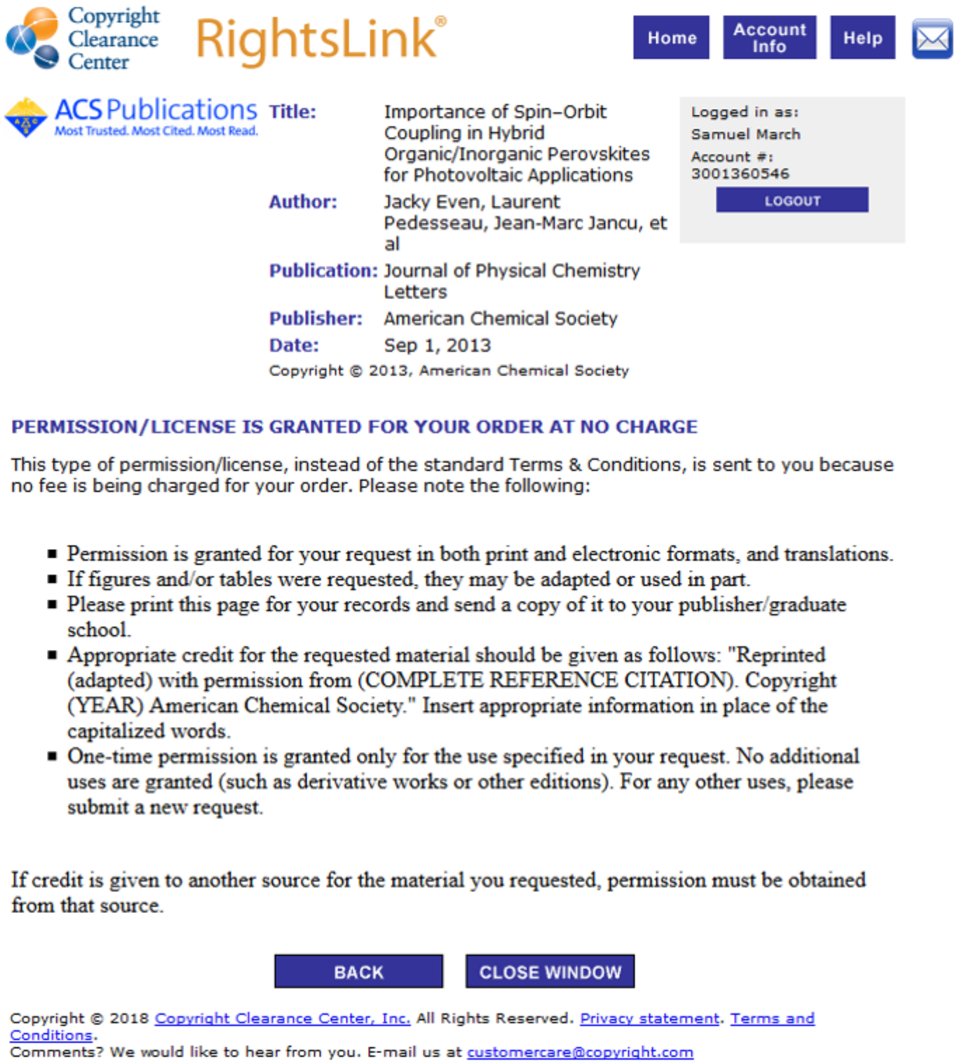

Title: Importance of Spin–Orbit Coupling in Hybrid Organic/Inorganic Perovskites for Photovoltaic Applications

Author: Jacky Even, Laurent Pedesseau, Jean-Marc Jancu, et al

Publication: Journal of Physical Chemistry Letters

Publisher: American Chemical Society

Date: Sep 1, 2013

Copyright © 2013, American Chemical Society

Logged in as:
Samuel March
Account #:
3001360546

PERMISSION/LICENSE IS GRANTED FOR YOUR ORDER AT NO CHARGE

This type of permission/license, instead of the standard Terms & Conditions, is sent to you because no fee is being charged for your order. Please note the following:

- Permission is granted for your request in both print and electronic formats, and translations.
- If figures and/or tables were requested, they may be adapted or used in part.
- Please print this page for your records and send a copy of it to your publisher/graduate school.
- Appropriate credit for the requested material should be given as follows: "Reprinted (adapted) with permission from (COMPLETE REFERENCE CITATION). Copyright (YEAR) American Chemical Society." Insert appropriate information in place of the capitalized words.
- One-time permission is granted only for the use specified in your request. No additional uses are granted (such as derivative works or other editions). For any other uses, please submit a new request.

If credit is given to another source for the material you requested, permission must be obtained from that source.

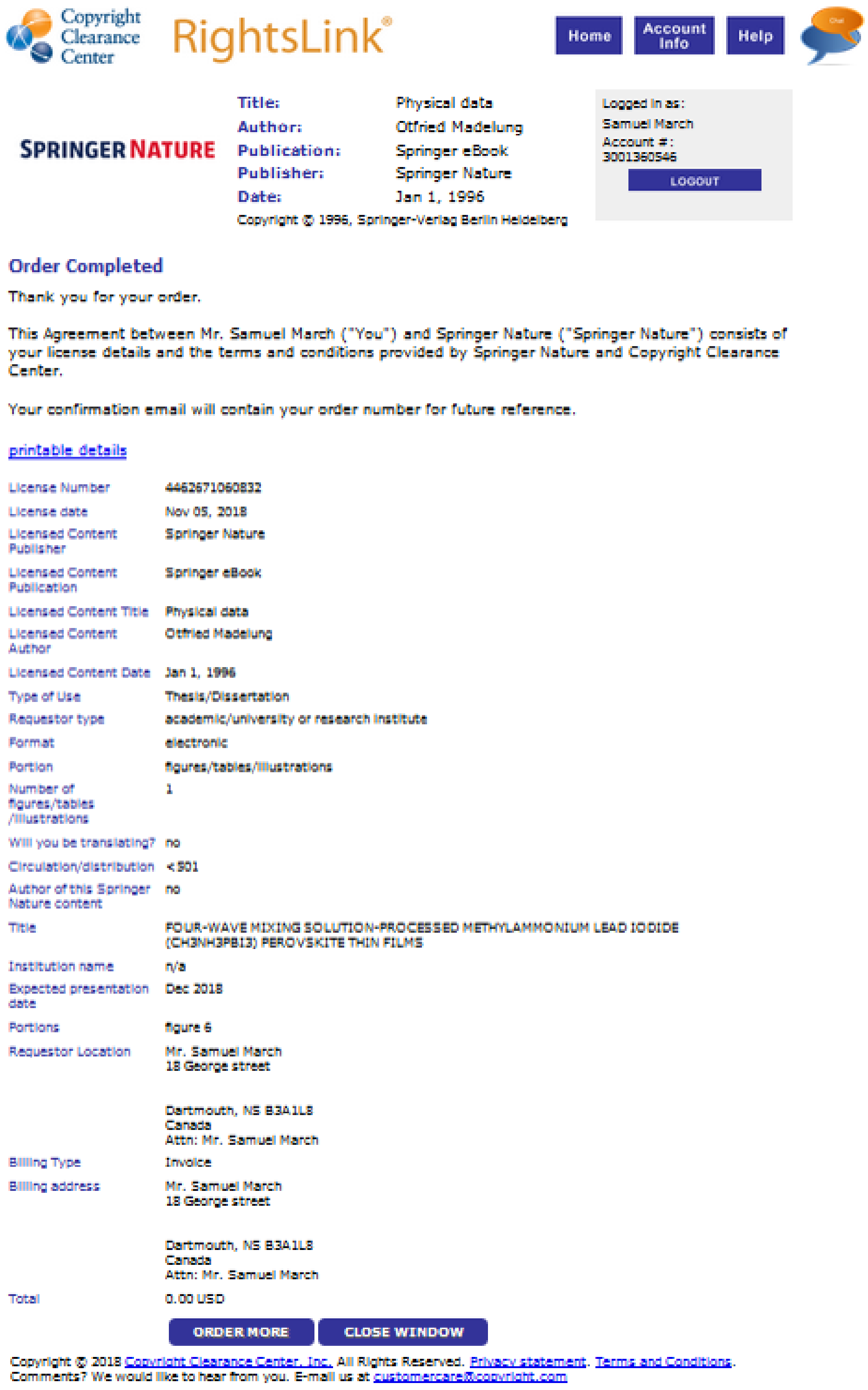

Title: Physical data
Author: Otfried Madelung
Publication: Springer eBook
Publisher: Springer Nature
Date: Jan 1, 1996
Copyright © 1996, Springer-Verlag Berlin Heidelberg

Logged in as:
Samuel March
Account #:
3001360546

Order Completed

Thank you for your order.

This Agreement between Mr. Samuel March ("You") and Springer Nature ("Springer Nature") consists of your license details and the terms and conditions provided by Springer Nature and Copyright Clearance Center.

Your confirmation email will contain your order number for future reference.

License Number	4462671060832
License date	Nov 05, 2018
Licensed Content Publisher	Springer Nature
Licensed Content Publication	Springer eBook
Licensed Content Title	Physical data
Licensed Content Author	Otfried Madelung
Licensed Content Date	Jan 1, 1996
Type of Use	Thesis/Dissertation
Requestor type	academic/university or research institute
Format	electronic
Portion	figures/tables/illustrations
Number of figures/tables /illustrations	1
Will you be translating?	no
Circulation/distribution	< 501
Author of this Springer Nature content	no
Title	FOUR-WAVE MIXING SOLUTION-PROCESSED METHYLAMMONIUM LEAD IODIDE (CH3NH3PBI3) PEROVSKITE THIN FILMS
Institution name	n/a
Expected presentation date	Dec 2018
Portions	figure 6
Requestor Location	Mr. Samuel March 18 George street Dartmouth, NS B3A1L8 Canada Attn: Mr. Samuel March
Billing Type	Invoice
Billing address	Mr. Samuel March 18 George street Dartmouth, NS B3A1L8 Canada Attn: Mr. Samuel March
Total	0.00 USD

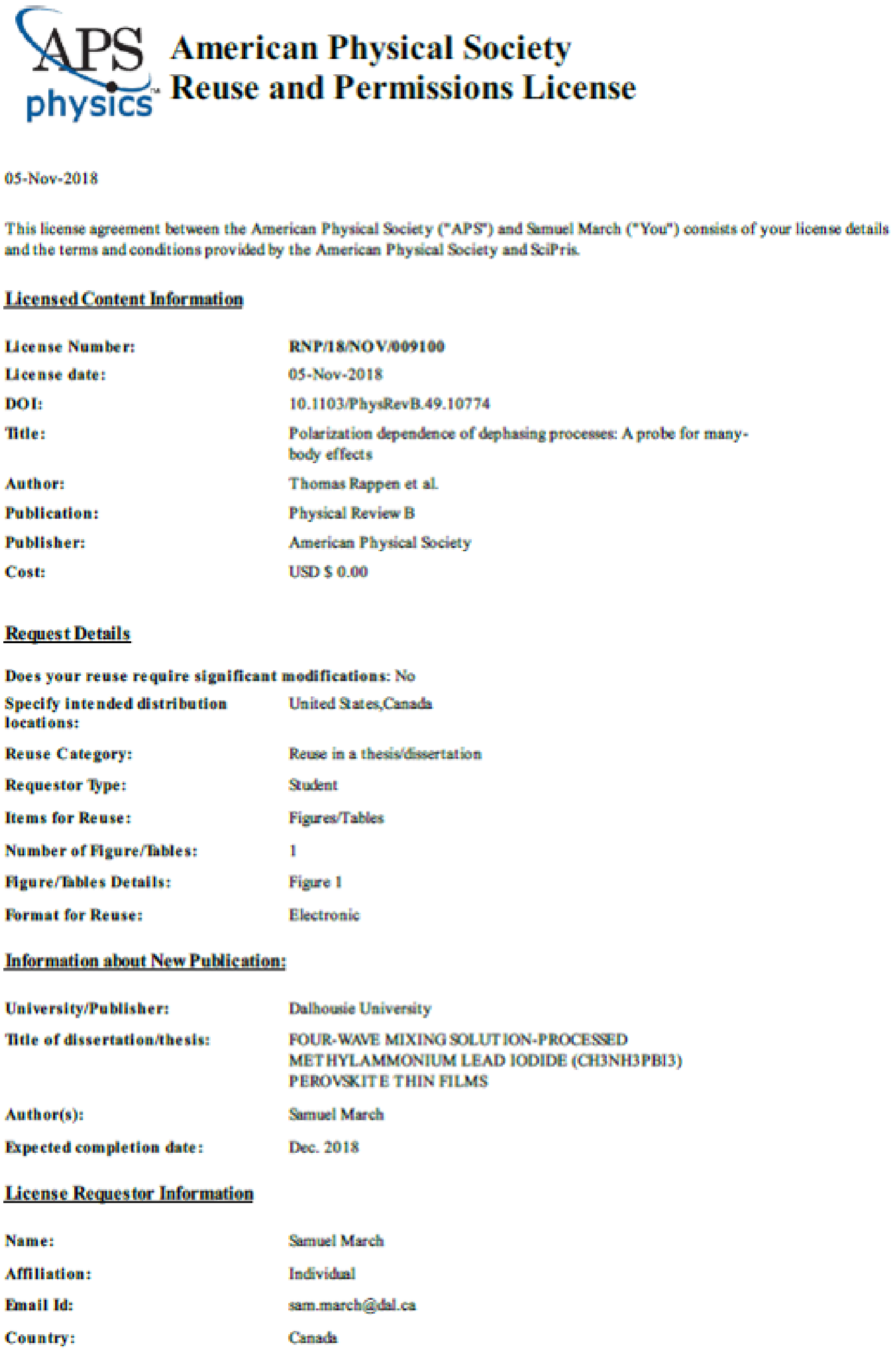

American Physical Society Reuse and Permissions License

05-Nov-2018

This license agreement between the American Physical Society ("APS") and Samuel March ("You") consists of your license details and the terms and conditions provided by the American Physical Society and SciPris.

Licensed Content Information

License Number:	RNP/18/NOV/009100
License date:	05-Nov-2018
DOI:	10.1103/PhysRevB.49.10774
Title:	Polarization dependence of dephasing processes: A probe for many-body effects
Author:	Thomas Rappen et al.
Publication:	Physical Review B
Publisher:	American Physical Society
Cost:	USD $ 0.00

Request Details

Does your reuse require significant modifications: No

Specify intended distribution locations:	United States,Canada
Reuse Category:	Reuse in a thesis/dissertation
Requestor Type:	Student
Items for Reuse:	Figures/Tables
Number of Figure/Tables:	1
Figure/Tables Details:	Figure 1
Format for Reuse:	Electronic

Information about New Publication:

University/Publisher:	Dalhousie University
Title of dissertation/thesis:	FOUR-WAVE MIXING SOLUTION-PROCESSED METHYLAMMONIUM LEAD IODIDE (CH3NH3PBI3) PEROVSKITE THIN FILMS
Author(s):	Samuel March
Expected completion date:	Dec. 2018

License Requestor Information

Name:	Samuel March
Affiliation:	Individual
Email Id:	sam.march@dal.ca
Country:	Canada